Modeling, Dynamic Analysis, and Stabilization of Converter-Based Distributed Generation Systems Considering Low-Voltage Ride-Through Requirements, Unbalanced and Weak Grid Conditions, and Load Dynamics

by

Shahed Mortazavian

A thesis submitted in partial fulfillment of the requirements for the degree of

Doctor of Philosophy

in

Energy Systems

Department of Electrical and Computer Engineering
University of Alberta

Abstract

The distributed generation (DG) is an alternative and efficient method to supply electric power to customers in the modern electricity market. Nowadays, there is a growing interest in connecting more DG units to utility distribution networks to satisfy the increasing demand, provide simplified and effective connections, and avoid the high investment costs for system upgrades. For an effective integration of DG units into the power networks, the low-voltage ride-through (LVRT) requirements have been recently recommended for large DG installations. The capability of the LVRT is an important mandate for the converter-interfaced DG units. The system operators impose new grid codes requiring large DG units to remain connected and improve the voltage profile during short-term grid faults. To maintain the stability of the power system, DG units are also expected to inject reactive current proportional to the voltage drop, with a dead-band applied to the voltage deviation.

This thesis provides a detailed modeling, dynamic analysis, and systematic control design procedure to stabilize the performance of grid-connected voltage-source converters considering LVRT requirements, unbalanced and weak grid conditions, and load dynamics. In this regard, the state-space model of a grid-connected converter (GCC) in dispatchable DG applications and for the power system configuration with single- and multiple-DG units are considered for small-signal stability analysis under unbalanced and low-voltage conditions. Because

power distribution systems are naturally unbalanced (due to their lines and loads characteristics, and increasing penetration of DG), such a tool is necessary to realize reliable and secure operation. The state-space model is then used to develop a model-based compensation method that stabilizes the performance of the overall system, especially under a weak grid condition.

Furthermore, the new LVRT standards require the DG units to not only stay connected to the grid but also inject both positive and negative sequence reactive currents proportional to the unbalanced voltage sag characteristics under severe short-term unbalanced grid faults. In addition to the nonlinear dynamics of a GCC, this requirement adds more coupling and complexity to the system in dynamic, transient and stability studies. Therefore, a multi-stage linearized state-space model, with the consideration of the positive and negative sequence reactive current injection, is developed to analyze the dynamic performance and stability of the GCC-based DG unit under fault conditions. A control design method based on the integrated converter dynamics is also presented to stabilize the converter performance.

With the expected high penetration level of DG units in modern power distribution systems and recent progress in power converter topologies and ratings, medium voltage DG units will be subjected to a wide range of both static and dynamic loads. Therefore, integrated modeling, analysis, and stabilization approach of a GCC-based DG unit with an induction machine load are studied. A comprehensive multi-stage small-signal model is obtained to provide the possibility

of the grid fault studies for different operating states of the system. This model is then used to assess the impact of the induction machine dynamics on the overall system stability as compared with the static load model and under different grid strength conditions. Control design methods to facilitate stable operation and successful LVRT performance are presented and evaluated.

In all stages of the study, comparative simulation and laboratory-scale experimental results are used to validate the theoretical analysis and the effectiveness of the proposed models and compensation methods.

Preface

This thesis is an original work by Shahed Mortazavian. As detailed in the following, some chapters of this thesis have been published or submitted for publication as scholarly articles in which Professor Yasser Abdel-Rady I. Mohamed was the supervisory author and has contributed to concepts formation and the manuscript composition. Mr. Masoud M. Shabestary assisted with method implementation and manuscript composition of the first article.

A version of Chapter 2 has been published as

- S. Mortazavian, M. M. Shabestary and Y. A. R. I. Mohamed, "Analysis and Dynamic Performance Improvement of Grid-Connected Voltage–Source Converters Under Unbalanced Network Conditions," *IEEE Transactions on Power Electronics*, vol. 32, no. 10, pp. 8134-8149, Oct. 2017.

A version of Chapter 3 has been published as

- S. Mortazavian, Y. A. I. Mohamed, "Dynamic Analysis and Improved LVRT Performance of Multiple DG Units Equipped With Grid-Support Functions Under Unbalanced Faults and Weak Grid Conditions," *IEEE Transactions on Power Electronics*, vol. 33, no. 10, pp. 9017-9032, Oct. 2018.

A version of Chapter 4 has been submitted as

- S. Mortazavian, and Y. A. R. I. Mohamed, “Analysis and Enhanced Model-Based Control Design of Distributed Generation Converters with Flexible Grid-Support Controller,” Conditionally accepted with major mandatory changes in *IEEE Transactions on Power Electronics*, revised and resubmitted in June 2018.

A version of Chapter 5 is submitted as

- S. Mortazavian, and Y. A. R. I. Mohamed, “LVRT Performance Improvement in Grid-Connected Converter Based DG Units with Dynamic Loads,” Submitted to *IEEE Transactions on Power Electronics*, July 2018.

This thesis work is dedicated to my husband, who has been a constant source of support and encouragement during the challenges of my graduate studies and life. I am truly thankful for having you in my life.

This work is also dedicated to my parents, who have always loved me unconditionally and whose good examples have taught me to work hard for the things I aspire to achieve.

Acknowledgment

I would like to express my sincere appreciation to Prof. Yasser Abdel-Rady I. Mohamed for his great support and supervision during this research project. This research and dissertation would not have been possible without his continuous guidance.

Also, I would like to extend a special thanks to Prof. Walid Morsi and other examining committee members including Prof. Yasser Mohamed, Prof. Venkata Dinavahi, Prof. Ali Khajehoddin and Prof. Yunwei (Ryan) Li for taking the time to review this thesis. I am also thankful to all the faculty and staff members in the Department of Electrical and Computer Engineering at the University of Alberta who provided a pleasant working atmosphere for me during the past five years.

Table of Contents

List of Tables

List of Figures

List of Acronyms

BPSC	Balanced Positive-Sequence Control
DDSRF	Decoupled Double Synchronous Reference Frame
DG	Distributed Generation
FMS-RCI	Flexible Multi-Sequence Reactive Current Injection
GCC	Grid-Connected Converter
IM	Induction Machine
LVRT	Low-Voltage Ride Through
PCC	Point of Common Coupling
PFA	Participation Factor Analysis
PI	Proportional-Integral
PLL	Phase-Locked Loop
PNSC	Positive–Negative-Sequence Compensation
PWM	Pulse-Width Modulation
RCG	Reference Current Generation
RMS	Root Mean Square
SCR	Short-Circuit Ratio
SSSA	Small Signal Stability Analysis
VSC	Voltage Source Converter

List of Symbols

A. *Superscripts*

+	Positive sequence components
-	Negative sequence components
*	Variable reference value
ss	Steady-state value

B. *Subscripts*

d	Variable component in *d*-axis
q	Variable component in *q*-axis.

C. *Variables and parameters*

i_g	Grid currents.
i_l	DG currents.
i_c	Capacitor current
V_p	voltage at the PCC.
P^*	Reference active power of DG.
Q^*	Reference reactive power of DG.
V_f	filtered feed-forwarded value of the PCC voltage.
V_g	Grid voltage (at bus1).
C_f	Capacitance of the ac filter.
R_f	Equivalent resistance of the ac filter, coupling transformer, and connection cables of DG up to PCC
L_f	Equivalent inductance of the ac filter, coupling transformer, and connection cables of DG up to PCC
R_l	Equivalent resistance of the connection cables between PCC and bus2.
L_l	Equivalent inductance of the connection cables between PCC and bus2.
R_0	Equivalent resistance of the connection cables between bus2 and bus1.
L_0	Equivalent inductance of the connection cables between bus2 and bus1.
R_g	Equivalent grid resistance up to bus1.
L_g	Equivalent grid inductance up to bus1.
ω_0	Grid angular frequency.
K^+	Positive sequence coefficient of the FMS-RCI method.
K^-	Negative sequence coefficient of the FMS-RCI method.

K_i	Integrator gain of the current controller compensator of DG.
K_p	Proportional gain of the current controller compensator of DG.
$K_{i,PLL}$	Integrator gain of the PLL.
$K_{p,PLL}$	Proportional gain of the PLL.
τ_{ff}	Time constant of the feed-forwarded LPF of the PCC voltage.
τ_1	Time constant of the LPF on V_{pd}^{+} sampling before the RCG.
τ_2	Time constant of the LPF on V_{pq}^{+} sampling before the PLL.

Chapter 1

Introduction

The increasing concerns about climate change, rising fossil fuel prices, and energy security caused a growing global interest in renewable energy resources. It is a great challenge to integrate a significant portion of renewable energy resources into the existing power grid. In contrast to the traditional large power plants, renewable energy plants are installed in a more distributed manner with less capacity and at different locations. The integration of distributed generation (DG) units has thus great impacts on the operation of the grid and necessitates new grid infrastructures. Although there are numerous advantages associated with the significant development of the renewable energies and DG units, their increasingly high penetration level will bring inherent negative effects on the dynamic performance of the power system. To maintain the stability of the system, grid operators have specified a set of requirements for the integration of DGs. New grid codes strictly demand low-voltage ride through (LVRT) capability, which mandates DG units to remain connected during a fault and even, in some cases, inject the reactive current to support the system.

To this day, the existing literature suffers from the lack of detailed dynamic analysis and systematic design procedure to enhance the dynamic performance of grid-connected voltage-source converters equipped with grid-support controllers under unbalanced grid conditions. The unbalanced conditions bring the negative voltage and current components to the problem, causing considerable effects on the accuracy of the existing simplified linear models of the DGs integration in balanced conditions. Therefore, a full characterization of the whole DG-integrated system, under unbalanced conditions, is needed to obtain an accurate and reliable

assessment of the dynamic behavior of such systems. In addition, by expanding the system to a multi-DG case, some other constraints appear such as considering different DG control modes (e.g., PQ and PV modes), the effect of the location of the unbalanced fault and, the effects of variations in the distribution system line parameters and their influence on the whole system characteristic.

To increase the penetration level of renewable energy resources in modern power grids, new challenges, as well as new approaches to operate power grids, are necessary. For example, some countries have issued dedicated grid codes for connecting wind turbines/farms to the electrical network at the transmission and distribution systems. In most of the cases, e.g., in Denmark, Germany, and Ireland, these requirements focus on power controllability, power quality and, fault ride-through (FRT) capability [18]. Moreover, some grid codes require grid support during network disturbances; e.g., Germany and Spain [18]-[20]. Denmark has the most demanding requirements regarding the controllability of the generated power. The power quality requirements are very demanding in respect to flicker emission as well as the harmonic compatibility levels for voltages, particularly at the distribution level. All existing grid codes require FRT capabilities for wind turbines. Voltage profiles specify the depth of the voltage dip and the clearance time as well. This trend calls for advanced control, analysis and performance improvement of distributed generation systems under different types of network disturbances.

1.1 Events in Electrical Network

Various events can occur in electrical networks, and most of them are related to the network voltage. These voltage events are usually characterized by a change in the magnitude of the voltage, and they can have different time durations from milliseconds up to hours [1]-[3]. Based on these two main characteristics, namely magnitude and duration, the voltage events are classified by standards in different ways. The standard EN 50160 [2] is focused on the characterization of voltages in low- and medium-voltage networks. The momentary voltage disturbances are classified in IEEE Std. 1250 [4] for a duration up to a few seconds. Based on [1],

two types of events are characterized by this magnitude and duration: short interruptions and voltage sags. These events are mainly related to the short-circuits in the electrical networks.

1.1.1 Short Interruptions

The origins of the voltage interruptions, in general, are faults which subsequently trigger the protection measure [1]. Other primary causes can be classified as 1) protection operation when there is no fault; 2) broken conductors without triggering the protective measure; and, 3) operator intervention.

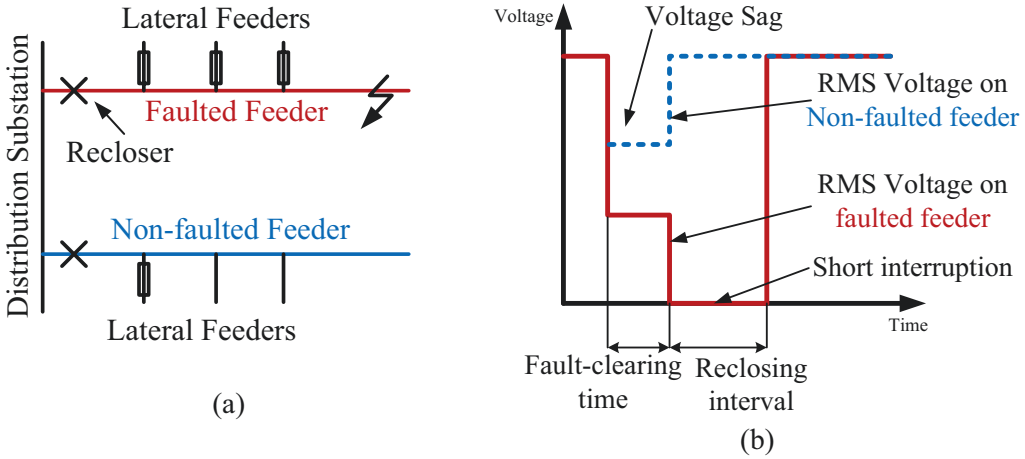

Figure 1.1 Fault in a distribution network: a) Network layout and b) RMS voltages on feeders.

When the supply is restored automatically, the resultant event is called a short interruption. Based on the network layout between the location of the fault and the point where the voltage is measured and the protection schemes used, the event can be seen in a different way (Figure 1.1). The voltage on the faulted feeder will drop to zero while the non-faulted feeder will see a voltage sag.

1.1.2 Voltage Sags

According to [1], the voltage sags are short duration reductions in RMS voltage, caused by short circuits, overloads, and starting of large motors. Because voltage sags are caused by short-circuit faults located at hundreds of kilometers away in the transmission system, these events are more global problems than an interruption. The magnitude of the voltage sags are determined by the following factors: 1) distance to fault; 2) cross-section of the lines and cables; 3) connection type of

transformers between the location of fault and the recording point; 4) type of the network (radial or loops); 5) short-circuit impedance of the network, etc.

An overview regarding the influence of transformer winding connections on the propagation of voltage sags is given in [5]. When several cascaded transformers are present between the fault location and the point of voltage measurement, the voltage sag will be determined by the connection types of all these transformers.

In the 1980s, the cage induction generators were utilized in the first generation of fixed-speed grid-connected wind turbines to maintain a high power factor [6]. The doubly fed induction generator (DFIG) was then presented during the 1990s in which typically a 0.3 per-unit (p.u.) converter is used to control the rotor voltage. By controlling the reactive power within some boundaries and by adding a chopper in the dc-link, FRT or LVRT requirements can be achieved in this technology. Today, both the DFIG and full-scale converter technologies can comply with the most demanding grid codes [7]-[12]. However, because the DFIG compliance is becoming more challenging based on the new grid codes, especially in the case of asymmetrical grid faults, there is a strong trend toward the full-scale converter topology [11]-[14].

As the power level of modern wind turbines is continuously increasing, even up to 7 MW, the wind power generation systems are required to withstand extreme grid disturbances and be more reliable. In [15], three promising grid-side multilevel converter topologies for the next-generation wind turbines with 10 MW capacity were proposed. Some heavily loaded power devices, especially the diodes, experienced difficulties in higher junction temperature, under LVRT operation. Besides, the three-level and five-level H-bridge topologies presented more potential to reduce the inequality of device stress than the well-known three-level neutral point clamped (NPC) topology. The predictive current control was applied to the grid-side NPC converter in [16], to provide the LVRT requirements. Considering the redundant switching states of the NPC converter, the dc-link neutral-point balance is also attained employing the predictive control algorithm. This method showed a fast and accurate current reference tracking performance. Another control

scheme for the back-to-back NPC converter was presented in [17]. By storing the active power surplus in the turbine-generator mechanical system inertia during grid voltage dip, the controllers of the generator-side and grid-side converters work simultaneously to meet the LVRT requirements and keep the dc-link voltage constant [17].

1.2 Literature Review

1.2.1 LVRT Requirements under Unbalanced Grid Conditions

The LVRT requirements necessitate the wind-power plants to remain connected to the network in the presence of grid voltage dips [18]-[20]. Most grid faults cause positive, negative, and zero sequence components in the voltage of the point of common coupling (PCC). Hence, regulators based on symmetrical components are well suited to control grid-connected converters (GCCs). In this thesis, the system under study is designed based on a typical Northern Ontario, Canada rural distribution system. It comprises a radial distribution system with dispatchable three-wire DG units. The dc-side of each VSC is equipped with a combination of the main energy resource (e.g., a fuel cell) and a fast dynamic response energy storage system (e.g., a supercapacitor) so that the hybrid source provides an almost constant dc-bus voltage for the inverter [36], [59], [61], [75]. Three different current controllers based on symmetrical components and linear quadratic regulator were considered in [21]. Results show that all three controllers can meet the LVRT requirements, but all the control objectives cannot be achieved simultaneously. Each control scheme gives different comparative advantages in terms of system performance. One control scheme was designed to deliver balanced grid currents, whereas the other one was designed to nullify the oscillating active power flow. Therefore, the controller selection depends on the system constraints and the performance features. A control method based on the injection of reactive current with a variable ratio between positive and negative sequences was presented in [22]. It sets two control parameters online: the reactive power reference value and a parameter that balances the positive and negative sequences of the reactive current.

In this way, the inverter helps to restore the dropped voltages within the continuous operation limits determined by the grid codes.

The analytical evaluations and mathematical assessments of three reference current generation strategies in GCCs were studied in [23]. In [23], the authors obtained the analytical expressions of the instantaneous active/reactive powers oscillation and the maximum phase currents in different strategies to conduct several comparisons among them. Also, based on the obtained formulas for the maximum phase currents, the maximum allowable support control strategies are presented under unbalanced voltage conditions. The proposed methods help all studied techniques to provide their maximum voltage or frequency support under the pre-set maximum phase current limitations. In [1], different reference current generation (RCG) methods for the GCCs were presented using a generic vector approach. Using this analysis, the following generalized RCG methods which are valid in either stationary or synchronous reference frames are carried out in this thesis.

1.2.1.1 Traditional RCG techniques

In this current control technique, the reference current is generated using the following instantaneous power equations in *dq* frame when the phase-locked loop (PLL) system is in the steady state and is synchronized [24]:

$$P_s(t)=\frac{3}{2}V_{pd}i_d,\quad Q_s(t)=\frac{-3}{2}V_{pd}i_q \tag{1.1}$$

Using the feedback from PCC voltage measurement (V_{pd} and V_{pq}) to this controller, i_d^* and i_q^*, in the positive and negative sequences, are calculated as (1.2).

$$i_{1d}^{*+}=\frac{2}{3}\frac{P^*}{V^+_{pd}},\ i_{1d}^{*-}=0,\quad i_{1q}^{*+}=\frac{-2}{3}\frac{Q^*}{V^+_{pd}},\ i_{1q}^{*-}=0 \tag{1.2}$$

1.2.1.2 Balanced Positive-Sequence Control (BPSC)

The balanced positive-sequence control (BPSC) is the other RCG method selected from different methods presented in [25], to be studied thoroughly using small-signal analysis. This strategy is used to deliver the reference active and reactive

powers, P^* and Q^*. The general reference current values, i.e., i_p^* and i_q^*, can be obtained as:

$$i_p^* = gv\,,\; i_q^* = bv_\perp \qquad i^* = i_p^* + i_q^* \tag{1.3}$$

where g and b can be considered as instantaneous conductance and susceptance [25]. For the BPSC strategy, the conductance and susceptance are defined as

$$i_P^* = G^+ v^+, \quad G^+ = \frac{2/3\, P^*}{\left|V^+\right|^2} \tag{1.4}$$

$$i_Q^* = B^+ v_\perp^+, \quad \mathrm{B}^+ = \frac{-2/3\, Q^*}{\left|V^+\right|^2} \tag{1.5}$$

According to (1.4) and (1.5), the reference currents only follow the positive sequence and become sinusoidal and balanced even under the unbalanced and low-voltage condition. The expression of these RCG equations in the positive and negative dq frames can be given by

$$\begin{bmatrix} i_d^{+*} \\ i_q^{+*} \end{bmatrix} = \begin{bmatrix} i_{Pd}^{+\,*} \\ i_{Pq}^{+\,*} \end{bmatrix} + \begin{bmatrix} i_{Qd}^{+\,*} \\ i_{Qq}^{+\,*} \end{bmatrix} = G^+ \begin{bmatrix} V_d^+ \\ V_q^+ \end{bmatrix} + B^+ \begin{bmatrix} -V_q^+ \\ V_d^+ \end{bmatrix} \tag{1.6}$$

$$i_d^{-*} = i_q^{-*} = 0 \tag{1.7}$$

1.2.1.3 Positive–Negative-Sequence Compensation (PNSC)

The next studied RCG method is called the PNSC. In this strategy, the reference current values contain a set of positive- and negative-sequence components designed to remove some oscillations from the instantaneous active/reactive powers. Using these equations, the reference currents i_p^* and i_q^* are obtained as

$$i_p^* = i_p^{+*} + i_p^{-*} = G^+ V^+ + G^- V^-, \quad G^+ = -G^- = \frac{P^*}{\left|V^+\right|^2 - \left|V^-\right|^2} \tag{1.8}$$

$$i_Q^* = i_Q^{+*} + i_Q^{-*} = B^+ V_\perp^+ + B^- V_\perp^-, \quad B^+ = -B^- = \frac{Q^*}{\left|V^+\right|^2 - \left|V^-\right|^2} \tag{1.9}$$

The reference-current equations in the positive dq frame will be similar to (1.6) and, in the negative dq frames are expressed as

$$\begin{bmatrix} i_d^{-*} \\ i_q^{-*} \end{bmatrix} = \begin{bmatrix} i_{Pd}^{-*} \\ i_{Pq}^{-*} \end{bmatrix} + \begin{bmatrix} i_{Qd}^{-*} \\ i_{Qq}^{-*} \end{bmatrix} = G^{-} \begin{bmatrix} V_d^{-} \\ V_q^{-} \end{bmatrix} + B^{-} \begin{bmatrix} -V_q^{-} \\ V_d^{-} \end{bmatrix} \tag{1.10}$$

1.2.2 Small-Signal Stability Analysis

Small-signal stability analysis (SSSA), as defined in [26], is the ability of the power system to maintain synchronism when subjected to small disturbances. In the case of a small disturbance, the equations that describe the resulting response of the system may be linearized for the purpose of analysis. The possible instability can be of two forms: (1) generator rotor angle increases due to lack of synchronizing torque, or (2) there would be rotor oscillations of increasing amplitude due to lack of sufficient damping torque. The SSSA using linear techniques provides valuable information about the inherent dynamic characteristics of the power system and aids in its design. In fact, the simulation alone does not produce the qualitative information and insight that analytical models can provide. Even with the abundant computing power available today, the simulation time can be too long for a complex power system, particularly when the simulation has to be repeated over a large, multi-dimensional parameter space to cover various design scenarios and to develop general conclusions. Numerical convergence can also be a major problem, especially when the models are obtained from different sources.

Traditional power systems theory deals with such time-varying behavior by using phasor-based models [26]-[28]. Another method which is more commonly used in power electronics is to transform the system model into a rotating (*dq*) reference frame in which balanced three-phase variables become dc quantities, thereby also permitting small-signal analysis [29]. The impedance-based system stability theory has also been generalized to such transformed *dq*-coordinate systems and has been used to analyze three-phase PWM converter interactions with their input filters [30]. Different small-signal methods, their utilities, and limitations were reviewed in [31].

Similar to the approaches based on the *dq* rotating frame impedances, the study in [32] focused on single-phase systems using the dynamic phasor approach to

determine the two-dimensional source and load impedances. This method was used to identify a steady-state operation, enabling a small-signal impedance-based analysis. The generalized Nyquist stability criterion was used to evaluate the system stability. The authors experimentally proved that this theory could be used for the stability analysis by injecting and measuring quantities at an electric port of the grid.

The impact of the PLL parameters on the dynamic and steady-state behavior of a voltage-source converter (VSC) in an HVDC transmission system is studied in [33], by using a linearized small-signal model of the converter system and its controls. It was shown that the maximum power transfer capability of the VSC is affected by the PLL gains and that the theoretical limit (obtained from static voltage stability analysis) is useful for very small PLL gains. The authors showed that the gains of the PLL, particularly at low system strength (parameterized by the short-circuit ratio (SCR)), significantly affect the operation of the VSC.

1.2.3 LVRT in Multi-DG Systems

Most of the studies in the literature on multi-DG systems are devoted to the anti-islanding methods. For example, the authors of [34] studied the effect of the positive feedback-based anti-islanding scheme on the small-signal stability of multiple DGs during grid-connected operation in power distribution systems. Based on the sensitivity analysis results, it was concluded that the destabilizing effect of the positive feedback anti-islanding control limits the maximum multi-DG penetration level in an existing distribution system. Experimental validation of an active islanding detection algorithm for multi-inverter systems was presented in [35]. The results showed that this algorithm has a very low impact on power quality and rapid islanding confirmation. Another study is presented in [36] for the multi-DG system with the consideration of different loading conditions, variations of grid stiffness levels and different types of DG controllers. It is shown that each DG unit is required to perturb at distinct frequencies without requiring any communication among the DGs. The flow of harmonic and negative-sequence currents in the autonomous operation of a multi-bus MV microgrid under nonlinear and

unbalanced load conditions are studied in [68]. Two controllers are then presented to regulate the microgrid voltage and to share the harmonic currents of the nonlinear loads among the DG units.

However, the detailed dynamic analysis and systematic design procedure to enhance the dynamic performance of multiple grid-connected converter-based DG units, equipped with advanced controllers to support the host grid under unbalanced conditions, are not reported in the literature. To fill out this gap, this thesis presents a detailed small-signal model for typical medium-voltage multi-bus power distribution systems comprising multiple DG units that are equipped with the recently developed balanced positive-sequence control method to support the host grid under unbalanced conditions.

1.2.4 Flexible Multi-Sequence Reactive Current Injection Method During LVRT

In the German standards, E.ON, VDN [19]-[20], [37], and the recent European code, i.e., ENTSO-E [38], large wind power plants are expected to remain connected to the grid even under a voltage sag down to zero. To support the power system stability, DG units are also required to inject reactive current proportional to the voltage drop, with a dead-band applied to the voltage change [25]. Therefore, the GCC-based DG units are designed such that the active and reactive current injection to the grid is controlled independently with the consideration of the maximum current limit of the converter [6], [23], [25], [39]. As a conventional approach, the reactive current is injected as per grid code requirement, and any remaining capacity is utilized for the active power injection [20]. The research in [25] showed that wind power plants might lose their synchronism with the grid fundamental frequency during severe faults. This event even worsens the situation during the LVRT. A frequency-based active current injection algorithm is then presented in [25] to solve the loss of synchronism.

The new LVRT standards [37] require the DG units to not only stay connected to the grid under severe short-term unbalanced grid faults but also inject both positive and negative sequence reactive currents proportional to the unbalanced

voltage sag characteristics. The existing study in the literature on the dynamic behavior of the converters under unbalanced conditions [23], [39], [41], only deals with the four conventional RCG techniques which none requires a certain amount of reactive current injection under the unbalanced faults. These conventional RCGs are only responsible for having the basic LVRT capability which means the GCC is only required to stay connected under unbalanced conditions. However, in addition to the nonlinear dynamics of a GCC, the presence of the positive- and negative-sequence injection in LVRT adds more coupling and complexity to the system in dynamic, transient, and stability studies. This requirement may even lead to critical instability problems under different conditions, e.g., severe unbalanced faults, weak grid conditions, and conventionally tuned control parameters. This is a significant difference between the conventional LVRT requirements [18]-[19] and the newly imposed LVRT requirement [37], [40] under short-term unbalanced faults. Therefore, the flexible multi-sequence reactive current injection (FMS-RCI) technique is presented in this thesis to meet the new grid code requirement [40]. Two control parameters (i.e., K^+ and K^-) are used in this method to inject the positive- and negative-sequence reactive currents, respectively, proportional to the amount of the positive-sequence voltage drop and negative-sequence voltage rise. A model-based control parameters design is then proposed, to find suitable values for K^+ and K^- parameters in weak grid conditions for stability purposes under the mentioned LVRT requirements. The interactions between different converter controllers (e.g., current control and PLL) and FMS-RCI controller, is studied and their effect on the system stability is evaluated using the small-signal stability analysis.

1.2.5 Effect of Induction Motors (Dynamic Loads) on the LVRT Studies of Distribution Generation Systems

In traditional power system studies, it was shown that large induction motors (IMs) might interact with the rotor dynamics and excitation systems of synchronous generators. It may lead to modal resonances, limit cycles, and voltage oscillations [42]. The highly nonlinear IM dynamics coupling the active power, reactive power,

voltage, and supply frequency dynamics affect the stability of medium-voltage (MV) distribution system operating in the isolated microgrid mode [43]. In [43], the authors studied the integrated modeling and stabilization methods of MV droop controlled microgrids with IM load. The presented model accounts for the impact of supply frequency dynamics associated with the droop control. It was shown that the active power drawn by the IM participates in shaping the gently damped eigenvalues of the system. Another control strategy for inverter-based DGs to support microgrid stability in the presence of IMs is presented in [44]. This control method is based on droop design and flow management of current components to enable the microgrid to withstand transient faults and resume stable islanded operation. It shows that the current injection control is more supportive to microgrid stability than P and Q control scheme. The study in [45] showed that the presence of IM loads in converter-based isolated microgrids might produce source-load admittance mismatch leading to medium-frequency instabilities. It was shown that the interactions between the lightly-damped dynamics of IMs and isolated VSC-based microgrid have a remarkable destabilizing effect.

The dynamic behavior of a microgrid with three DG units (a gas-turbine synchronous generator, a wind turbine with DFIG and a VSC-based DG) was studied in [46]. The study results showed that the presented power-sharing approach contributed to mitigating microgrid system transients, improving dynamic performance, and reducing frequency changes following disturbances subsequent to islanding. A small-signal model of a typical microgrid containing asynchronous generator based wind turbine, synchronous diesel generator, power electronic based energy storage and power network was studied in [47]. The results showed that a properly designed and controlled energy storage is an essential solution to the reliable operation of microgrid and the effective utilization of renewable energy resource. The dynamic behavior of grid-connected small-scale synchronous generators to the system faults and its sensitivity to the system parameters were investigated in [48]. It was shown that the three-phase faults mostly affect system behavior.

This thesis presents integrated modeling, analysis, and stabilization approach of GCC-based DG units in connection with an IM load. A detailed multi-stage small-signal model of an MV GCC-based DG unit with both dynamic and static loads is developed. This model is then used to assess the impact of the IM dynamics on the overall system stability as compared with the static load model and under different grid strength conditions.

1.3 Thesis Motivations and Objectives

1.3.1 Motivations

Motivated by the reviewed literature, each of the following areas requires a full study:

1) A detailed linear model of a GCC considering symmetrical components injection under unbalanced network conditions,
2) A small-signal stability analysis of a GCC considering LVRT requirements and different reference current generation strategies,
3) A dynamic study of a GCC operation under unbalanced network conditions considering different system parameters, such as the network short-circuit ratio, PLL parameters, angle of the ac network impedance, and line parameters,
4) A coordination study to obtain the optimal control parameters for a GCC to improve the host grid stability under unbalanced conditions,
5) A dynamic performance analysis of multiple GCC-based DG units, known as a multi-DG system, equipped with advanced grid-support controls considering the unbalanced and weak grid conditions,
6) Modeling and dynamic analysis of the DG units equipped with RCG controllers based on the new LVRT standards in which the DG units are required to inject both positive and negative sequence reactive currents proportional to the unbalanced voltage sag characteristics under severe short-term unbalanced grid faults [37],
7) A dynamic analysis of the active distribution systems with converter-based DGs, in the presence of dynamic loads (induction motors), under unbalanced

conditions considering both the stiffness of the host grid and the new multi-sequence grid code requirements.

1.3.2 Objectives

To address the problems above, the following objectives are identified for this thesis work:

1) A state-space model of GCCs, in dispatchable DG applications, based on symmetric components should be developed for small-signal stability analysis under unbalanced and low-voltage conditions. Because power distribution systems are naturally unbalanced (due to their lines and loads characteristics, and increasing penetration of DG units), such a tool is necessary to investigate a reliable and secure operation. The results of the obtained analytical model should be compared to those of the nonlinear time-domain simulation model and a scaled-down laboratory prototype.
2) An improved model-based compensation method can be proposed using the presented state-space model of GCCs. This compensator can be used to enhance the dynamic behavior of the GCC under fault transients and low-voltage operation.
3) A detailed small-signal model for a medium-voltage multi-bus distribution system comprising multiple DG units should be developed under unbalanced conditions. The small-signal stability analysis should be performed to study the dynamic characteristics of such configuration.
4) A full characterization of the system should be obtained to assess the impacts of the following terms on the multi-DG system stability: (i) PLL control parameters, (ii) current control parameters, (iii) strength of the host grid, (iv) location of the fault, and (v) operation modes of DG units. Furthermore, the developed model can be used to provide an improved design and coordination of the control parameters of different DG considering various grid strengths and dynamic interactions in the system.
5) A thorough study on the application of the new LVRT requirements on DG units demanding for the injection of the positive- and negative-sequence of

the reactive current during the short-term grid fault. A dynamic analysis should be performed on the stability of the GCC-based DG units employing the FMS-RCI method under different grid strengths. This study can propose a model-based method to design the efficient controlling parameters for the FMS-RCI.

6) The impact of dynamic loads (induction motors) on the active distribution systems with converter-based DGs should be investigated, and the dynamic analysis and performance improvement of such system should be performed under unbalanced conditions. A detailed small-signal model of an induction motor with symmetrical components should be augmented to the model of the GCC. This model can be used to provide an improved dynamic performance of DGs in active distribution systems with dynamic loads.

Although the primary motivation and application intended for these developments are related to medium-voltage DGs connected to the distribution systems, the modeling, stability analysis, and the presented compensators can be extended to different power system sizes and voltage levels under unbalanced conditions.

1.4 Thesis Outline

The thesis is organized as follows.

Chapter 2: Stability Analysis of a GCC-Based DG Units under Unbalanced and Weak Grid Conditions - This chapter presents a detailed small-signal model and analysis of the dynamics of a grid-connected VSC equipped with the recently developed BPSC and PNSC methods to support the grid under unbalanced conditions. The impacts of the short-circuit ratio, angle of the ac system impedance, and phase-locked-loop parameters on the transient behavior of the VSC are thoroughly studied and characterized. Furthermore, to improve the dynamic performance of grid-connected VSCs, a simple yet effective current-control-based compensator is developed to mitigate possible instabilities associated with the low-

voltage operation. Comparative simulation and experimental results validate the theoretical analysis and the effectiveness of the proposed compensation scheme.

Chapter 3: Improved LVRT Performance of Multiple DG Units under Unbalanced and Weak Grid Conditions - This chapter initially presents a detailed small-signal modeling framework for typical medium-voltage multi-bus power distribution systems with multiple DG units, equipped with grid-support functions to operate under the unbalanced conditions. In addition, to precisely study the interactions among DG units, four different control modes in DG units are considered to study the system dynamics under low-voltage and unbalanced conditions and at different grid strengths. Using the proposed detailed state-space models and based on the small-signal stability analyses, different control parameters are re-designed by utilizing the eigenvalue analysis on the complete multi-DG system. As a second contribution, the sensitivity analyses are performed to study the effects of different system parameters, such as line characteristics, loading levels, and unbalanced fault characteristics, on the stability of the multi-DG system under unbalanced faults. Comparative simulation and experimental results are also reported to show the accuracy and effectiveness of the theoretical analyses.

Chapter 4: Enhanced Model-Based Control Design of GCC-Based DG Units Equipped with Flexible Grid-Support Controller - In this chapter, first, a multi-stage linear model of the augmented nonlinear system dynamics with the flexible positive- and negative-sequence current injection function is developed, and the small-signal stability analysis is performed on the system dynamic behavior before, during, and after the fault. Using this model, the characterization of the impact of the grid strength, converter control parameters, and proportionality constants of the FMS-RCI method is reported in this chapter. Second, a new and effective model-based controller design method is proposed to maintain the system stability during and after the fault with the consideration of the mutual interaction among different system controllers. Finally, the time-domain simulations and laboratory experiments validate the accuracy and effectiveness of the proposed control method.

Chapter 5: LVRT Performance Improvement in GCC-Based DG Units with Dynamic Loads - This chapter presents comprehensive integrated modeling, stability analysis and LVRT performance improvement methods for GCC-based DG units in the presence of an IM load considering different grid strengths. A detailed multi-stage small-signal model of the complete system is obtained, and the eigenvalue analysis is conducted considering both static and dynamic load modeling. Furthermore, a sensitivity analysis is performed to investigate the effect of the length of the power line between the DG unit and the IM on the stability and LVRT performance of the entire system. Finally, the LVRT performance of the DG unit under an unbalanced grid fault is investigated using three different reference current generation strategies to indicate the best strategy to provide a stable and efficient LVRT performance under strong and weak grid conditions. The time-domain simulation and experimental lab results are also presented to validate the effectiveness of the proposed approaches.

Chapter 6: Conclusions and Future Work - The contributions of this thesis and suggestions for future research work are presented in this chapter.

1.5 Thesis Contributions

The contributions of this thesis to the research field are as follows:

1) The development of a comprehensive *dq*-frame small-signal model for the study of the dynamic performance of GCCs with different RCG techniques in unbalanced systems. A state-space model is used to develop an improved model-based compensation method. This compensator enhanced the dynamic behavior of the GCC system under fault transients and weak grid condition.

2) The development of a detailed analytical model for the grid-connected multi-DG system considering the recent RCG strategies in the decoupled double synchronous reference frame (DDSRF). This model is used to perform the dynamic analysis and performance improvement of the multi-DG system equipped with advanced grid-support controls under unbalanced fault conditions. Also, the

interactions among DG units operating in different control modes (e.g., PV or PQ control modes) and under different grid strengths are assessed.

3) The full characterization of the studied systems through the development of detailed linearized state-space models at three stages, i.e., before the fault, during the fault, and after the fault. The proposed modeling approach considers different operating points at these three stages to analyze the system dynamics on the fault occurrence and clearance. This model is used to improve the control system designs. Using the developed models, the impacts of the following factors on the stability of the studied systems are analyzed under the unbalanced fault conditions: (1) parameters of the current and voltage controllers, (2) the PLL control parameters, (3) strength of the host grid, (4) control modes of the DG units, (5) the connecting line parameters, and (6) the location of the fault. Furthermore, the proposed state-space models are used to provide an improved design and coordination of the control systems in the DG units by re-designing the parameters of different controllers.

4) The study of the modeling and dynamic analysis of the DG units equipped with the RCG controllers based on the new LVRT standards which require the DG units to not only stay connected to the grid but also inject both positive and negative sequence reactive currents proportional to the unbalanced voltage sag characteristics under severe short-term unbalanced grid faults. This method is called the flexible multi-sequence reactive current injection (FMS-RCI) technique A model-based control parameters design is then proposed based on the small-signal stability analysis of the multi-stage linearized state-space model of the mentioned system, to find suitable values for the FMS-RCI controlling parameters in weak grid conditions for stability purposes under new LVRT requirements. The developed models and the proposed techniques are also applied to a more complex system with two DG units to consider the interactions between DG units on the LVRT performance of the entire system while using the FMS-RCI method.

5) The integrated modeling, analysis, and stabilization approach of GCC-based DG units in connection with an IM load. A detailed multi-stage small-signal model

of an MV GCC-based DG unit with both dynamic and static loads is developed in the DDSRF while employing the FMS-RCI strategy. The model includes the exact 10^{th} order model of the IM load and the 25^{th} order model of GCC-based DG unit along with the network dynamics. The participation factor analysis (PFA) is also conducted to identify the contribution of different states to the dominant eigenvalues of the GCC-based DG system with dynamic load model. The comprehensive multi-stage linearized model is then used to assess the impact of the IM dynamics on the overall system stability as compared with the static load model and under different grid strength conditions and, to propose a model-based controller design method based on the small-signal stability analysis to improve the LVRT performance of the GCC-based DG system. The proposed method could identify the optimum value for the control parameters of the system to improve its LVRT performance under different grid conditions and, at the same time, maintain its ability to retrieve the stable condition considering its relative stability margins.

Chapter 2

Stability Analysis of a GCC-Based DG Unit under Unbalanced and Weak Grid Conditions

According to the new grid codes, the grid-connected converters (GCCs) used in distributed generation (DG) units should withstand different grid faults [49]. Among hundreds of studies on new grid codes and low-voltage ride through (LVRT) technologies in GCCs, some recent works have analyzed the stability of such systems [25], [49]-[51]. In [52], some different reference current generation (RCG) methods are presented to comply with the power system LVRT requirements. In this chapter, the balanced positive-sequence control (BPSC) and positive–negative-sequence compensation (PNSC) strategies are selected to be studied thoroughly using small-signal stability analysis. In fact, the study of the dynamic behavior of a GCC under unbalanced network condition using small-signal stability analysis with positive/negative voltage and current state variables has not yet been addressed in the literature. The small-signal stability analysis is based on the fact that the perturbations studied in the system are small in magnitude, in the sense that they do not excite significant nonlinear behaviors, thus allowing the nonlinear dynamics of the system to be represented by a linearized model, for studies around an equilibrium point. It is a simplification of the dynamic behavior providing general information to power engineers, which cannot be easily retrieved from nonlinear simulations and analyses [53]. The unbalanced condition can considerably affect the dynamic behavior of a GCC. Therefore, a full

characterization of the unbalanced system is needed (e.g., such as the impacts of the phase-locked loop (PLL) parameters and different RCG strategies) to obtain an accurate assessment of the dynamic behavior of a GCC under unbalanced conditions.

Studies in [50] and [51] are based on the data analysis methods. The main drawback of these methods is that they need time-domain data of the system under study, and the observed dynamic response depends on the specifically analyzed perturbation, although they can be applied to any system by the use of nonlinear simulations [54]. Also, such methods mainly provide information on the modes of the system. Thus, some information, such as damping ratios and oscillation frequencies can only be estimated. If additional information regarding mode shapes and participation factor analysis (PFA) is needed, then a model-based analysis is necessary, and the system must be analyzed by its linearized model, normally represented in the state space [55], [56]. Because small-signal stability analysis is originally used in the large power transmission systems, several simplifications are often applied. Important among these is the consideration of a balanced three-phase system, which allows the power system to be represented by its single-phase equivalent [57], and the consideration of a phasor-domain model for the analyzed power system. These simplifications are needed for the development of a linear model with a defined operating point [58].

In this chapter, a state-space model of GCCs in dispatchable DG applications is presented for small-signal stability analysis under unbalanced and low-voltage conditions. Because power distribution systems are naturally unbalanced (due to their lines and loads characteristics, and increasing penetration of DG), such a tool is necessary to investigate a reliable and secure operation [59]. Therefore, the development of a *dq*-frame small-signal model is presented in this chapter for the study of the dynamic performance of GCCs with different RCG techniques in unbalanced systems. The presented state-space model is then used to develop an improved compensation method. This compensator has enhanced the dynamic behavior of the GCC system under fault transients and low-voltage operation. The obtained analytical model presented in this chapter is compared to the dynamic

behavior observed from the nonlinear detailed time-domain simulations and also a scaled-down laboratory prototype. The results show the accuracy of the proposed state-space models.

2.1 Studied Power System and Controllers Equations

Figure 2.1 shows a converter-based DG system connected to a power system. The grid is modeled as a Thevenin equivalent consisting of an equivalent resistance and inductance R_s and L_s, respectively. The line impedance between the source terminal and the point of common coupling (PCC) is Z_g. V_c is the voltage of the DG terminal that is connected to the PCC through the filter (R_f and L_f). Because the DG-side converter regulates the dc-link voltage, the dc-link voltage is considered constant in the study of GCCs. Such a system is widely used in studies related to LVRT and converter controls to support power grids under unbalanced condition [49], [59]-[61].

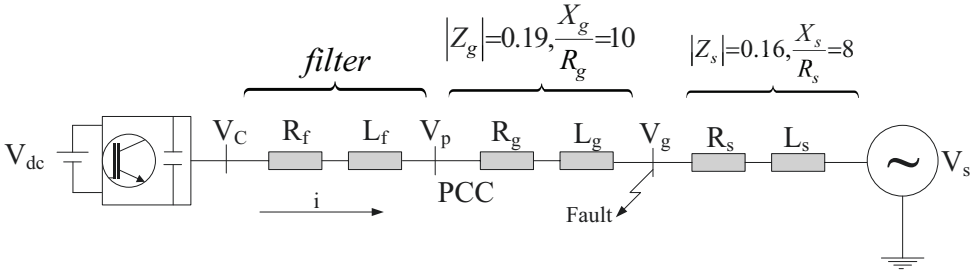

Figure 2.1 Test system

According to Figure 2.1, the ac side dynamics of the interfacing converter system is as follows:

$$L_f\left(\frac{di}{dt}\right) = -R_f i + V_c - V_p \tag{2.1}$$

$$L_g\left(\frac{di}{dt}\right) = -R_g i + V_p - V_g \tag{2.2}$$

2.1.2 Balanced and Unbalanced Systems

In a balanced network, the voltage and current can be simply expressed in the positive-sequence *dq* reference frame as:

$$L_f \frac{d}{dt}\begin{bmatrix} i_d \\ i_q \end{bmatrix} = -R_f \begin{bmatrix} i_d \\ i_q \end{bmatrix} + \begin{bmatrix} V_{cd} \\ V_{cq} \end{bmatrix} - \begin{bmatrix} V_{pd} \\ V_{pq} \end{bmatrix} - L_f \omega \begin{bmatrix} -i_q \\ i_d \end{bmatrix} \tag{2.3}$$

$$L_g \frac{d}{dt}\begin{bmatrix} i_d \\ i_q \end{bmatrix} = -R_g \begin{bmatrix} i_d \\ i_q \end{bmatrix} + \begin{bmatrix} V_{pd} \\ V_{pq} \end{bmatrix} - \begin{bmatrix} V_{gd} \\ V_{gq} \end{bmatrix} - L_g \omega \begin{bmatrix} -i_q \\ i_d \end{bmatrix} \tag{2.4}$$

By neglecting the zero sequence components, a three-phase signal in an unbalanced network can be decomposed into the positive and negative sequence components [62]. The detailed description of the transformations from $\alpha\beta$ to dq^+, dq^- can be found in [62]. Based on these transformations, system equations can be expressed by (2.5)-(2.8) during unbalanced condition.

$$L_f \frac{d}{dt}\begin{bmatrix} i_d^+ \\ i_q^+ \end{bmatrix} = -R_f \begin{bmatrix} i_d^+ \\ i_q^+ \end{bmatrix} + \begin{bmatrix} V_{cd}^+ \\ V_{cq}^+ \end{bmatrix} - \begin{bmatrix} V_{pd}^+ \\ V_{pq}^+ \end{bmatrix} - L_f \omega \begin{bmatrix} -i_q^+ \\ i_d^+ \end{bmatrix}, \tag{2.5}$$

$$L_f \frac{d}{dt}\begin{bmatrix} i_d^- \\ i_q^- \end{bmatrix} = -R_f \begin{bmatrix} i_d^- \\ i_q^- \end{bmatrix} + \begin{bmatrix} V_{cd}^- \\ V_{cq}^- \end{bmatrix} - \begin{bmatrix} V_{pd}^- \\ V_{pq}^- \end{bmatrix} + L_f \omega \begin{bmatrix} -i_q^- \\ i_d^- \end{bmatrix} \tag{2.6}$$

$$L_g \frac{d}{dt}\begin{bmatrix} i_d^- \\ i_q^- \end{bmatrix} = -R_g \begin{bmatrix} i_d^- \\ i_q^- \end{bmatrix} + \begin{bmatrix} V_{pd}^- \\ V_{pq}^- \end{bmatrix} - \begin{bmatrix} V_{gd}^- \\ V_{gq}^- \end{bmatrix} + L_g \omega \begin{bmatrix} -i_q^- \\ i_d^- \end{bmatrix} \tag{2.7}$$

$$L_g \frac{d}{dt}\begin{bmatrix} i_d^+ \\ i_q^+ \end{bmatrix} = -R_g \begin{bmatrix} i_d^+ \\ i_q^+ \end{bmatrix} + \begin{bmatrix} V_{pd}^+ \\ V_{pq}^+ \end{bmatrix} - \begin{bmatrix} V_{gd}^+ \\ V_{gq}^+ \end{bmatrix} - L_g \omega \begin{bmatrix} -i_q^+ \\ i_d^+ \end{bmatrix}, \tag{2.8}$$

In unbalanced conditions, there are four current components to be controlled as presented above, i.e., i_d^+, i_q^+, i_d^- and i_q^-. Therefore, the applied current control system consists of four independent PI controllers in the positive and negative *dq* frame, as shown in Figure 2.2.

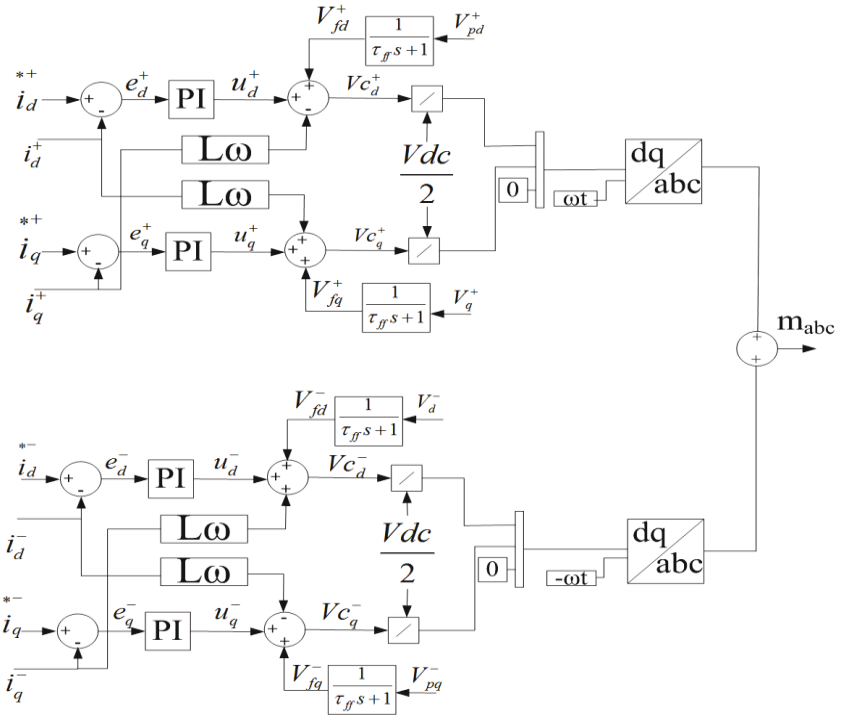

Figure 2.2 Current controller block in positive and negative *dq* frames.

2.1.3 Traditional RCG Techniques

In the first control technique, the reference current is generated based on the traditional RCG method. Using the feedback from PCC voltage measurement (V_{pd} and V_{pq}) to this controller, i_d^* and i_q^* are calculated based on the equations of (1.2). This controller is called RCG strategy-1 (RCGS-1).

In the second strategy, i_d^* and i_q^* are generated using PI active power and voltage controllers as presented in [33]. This controller is called RCG strategy-2 (RCGS-2).

2.1.4 Improved RCG Techniques for Grid Support

The BPSC and PNSC are selected as improved RCG techniques to be studied in the small-signal analysis and to be compared to two conventional GCC control strategies. The equations for these strategies are already presented in Sections 1.2.1.2 and 1.2.1.3.

2.2 State-Space Model

A linearized mathematical model of the studied power system (see Figure 2.1) in the standard form of

$$\Delta \dot{X} = A\Delta X + B\Delta U \tag{2.9}$$

is developed. This model is used to 1) design the controllers more accurately considering the system dynamics, 2) investigate the effectiveness of the proposed compensation method, 3) examine the system sensitivity to various control parameters variations, and 4) analyze the system dynamics in GCC integration into power grids with different characteristics (particularly connection of a GCC to a weak grid). The list of state variables for each strategy is presented in TABLE 2.1.

TABLE 2.1 List of state variables for four strategies

BPSC and PNSC	RCGS-1	RCGS-2
$X=[i_d^+, i_q^+, i_d^-, i_q^-, \int e_d^+dt, \int e_q^+dt, \int e_d^-dt, \int e_q^-dt, \int \omega dt, \int v_q^+dt, v_{fd}^+, v_{fq}^+, v_{fd}^-, v_{fq}^-]^T$	$X=[i_d, i_q, \int e_d dt, \int e_q dt, \int \omega dt, \int v_q dt, v_{fd}, v_{fq}]^T$	$X=[i_d, i_q, \int e_d dt, \int e_q dt, \int \omega dt, \int v_q dt, v_{fd}, v_{fq}, \int e_p dt]^T$

The input variable matrix in all methods is:

$$u=[V_{gd}^+, V_{gq}^+, V_{gd}^-, V_{gq}^-] \tag{2.10}$$

The linearized equations of controllers are divided into three parts: 1) PLL equations, 2) current controller and PWM generator equations and, 3) RCG equations. The state variables $\int \omega dt, \int v_q^+ dt$ and $\int v_q dt$ are obtained from the PLL equations. The other state variables are attained from the equations of the current controllers and RCG strategies.

2.2.2 PLL Equations

The linear model of the utilized PLL system is shown in Figure 2.3. Equation (2.11) represents the dynamics of the PLL controller where ω is the angular frequency, and θ is the phase angle obtained from the PLL. θ is synchronized to the PCC ac voltage.

$$\theta = \int \omega dt \ , \ \omega = \omega_0 + K_{p2} V_{pq} + K_{i2} \int V_{pq} dt \tag{2.11}$$

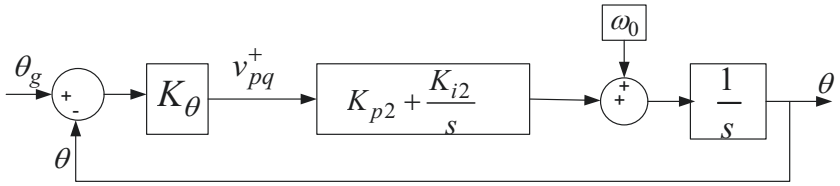

Figure 2.3 PLL system.

In the study of the unbalanced system condition, the V_{pq}^+ voltage is measured and fed into the PLL to synchronize θ and to prevent the effect of any negative sequence of the PCC voltage on the performance of the PLL. Therefore, the linearized form of (2.11) in the new frame is:

$$\Delta\theta = \int \Delta\omega dt \ , \ \Delta\omega = K_{p2} \Delta V_{pq}^+ + K_{i2} \int \Delta V_{pq}^+ dt \tag{2.12}$$

where V_{pq}^+ is the positive sequence of the PCC voltage in the q frame.

2.2.3 Current Controller and PWM Generator Equations

Equation sets of (2.3)-(2.4) and (2.5)-(2.8) are linearized to obtain the differential equations of the current state variables presented in TABLE 2.1. The linearized equations of this part are all obtained based on the diagram shown in Figure 2.2. The equations of the output voltage of the VSC (V_c) are derived as

$$\begin{aligned} &\Delta V_{cd}^+ = \Delta u_d^+ - L_f \omega_0 \Delta i_q^+ + \Delta V_{fd}^+ \ , \quad \Delta V_{cq}^+ = \Delta u_q^+ + L_f \omega_0 \Delta i_d^+ + \Delta V_{fq}^+ \ , \\ &\Delta V_{cd}^- = \Delta u_d^- + L_f \omega_0 \Delta i_q^- + \Delta V_{fd}^- \ , \quad \Delta V_{cq}^- = \Delta u_q^- - L_f \omega_0 \Delta i_d^- + \Delta V_{fq}^- \ , \end{aligned} \tag{2.13}$$

in which Δu is the output signal of the PI current controllers in the positive and negative dq frames and ΔV_f is the feedforward PCC voltage passed through the low-pass filters shown in Figure 2.2. The equations of Δu_d^+ and ΔV_{fd}^+ are

$$\Delta u_d^+ = K_p \ \Delta e_d^+ + K_i \int \Delta e_d^+ dt \tag{2.14}$$

$$\Delta V_{fd}^+ = \frac{\Delta V_{pd}^+}{\tau_{ff} s + 1} \Rightarrow \Delta \dot{V}_{fd}^+ = \frac{1}{\tau_{ff}} (\Delta V_{pd}^+ - \Delta V_{fd}^+) \tag{2.15}$$

where K_p and K_i are the proportional and integral gains of the PI current controllers. The Δu and ΔV_f in the other axes can be obtained similarly. Also, Δe in (2.14) represents the error between the reference and the measured currents and equals to $\Delta e = i^* - i$ in each axis. The i^* variables are obtained from the RCG equations.

2.2.4 RCG Equations

Based on the selected RCG strategy to generate i^*, the linearized equations will be different. The linearized i^* equations for the BPSC and PNSC strategies are derived with details in Appendix A. The linearized i^* equations of RCGS-1 and RCGS-2 can be similarly driven.

2.3 Case Studies and Simulation Results

The simulation results for the four aforementioned control techniques are presented in Figure 2.4. A one-phase to ground fault, between t=0.4 s to t=0.6 s, occurs and causes an unbalanced voltage. The grid voltage (V_g) drops to zero during the fault, and no protection or tripping schemes are provided for the GCC in the simulations. As illustrated, the BPSC is the only method that shows a balanced three-phase current during the fault. Moreover, high maximum phase currents, resulted by the other three strategies, may cause a trip in the protection system and failure in successful fault ride through. In the case of 1.0 pu active power delivery, the maximum phase current value, during the fault, is less than 2.0 pu for the BPSC strategy; but, in all other three methods, this value is around 3.0 pu. The only problem in the BPSC results is the transient behavior of the GCC in the fault occurrence and clearance. The phase current value on fault occurrence in all methods are high (i.e., 4.7 pu for RCGS-1, 3.7 pu for RCGS-2, 3 pu for PNSC, and 2.5 pu for BPSC).

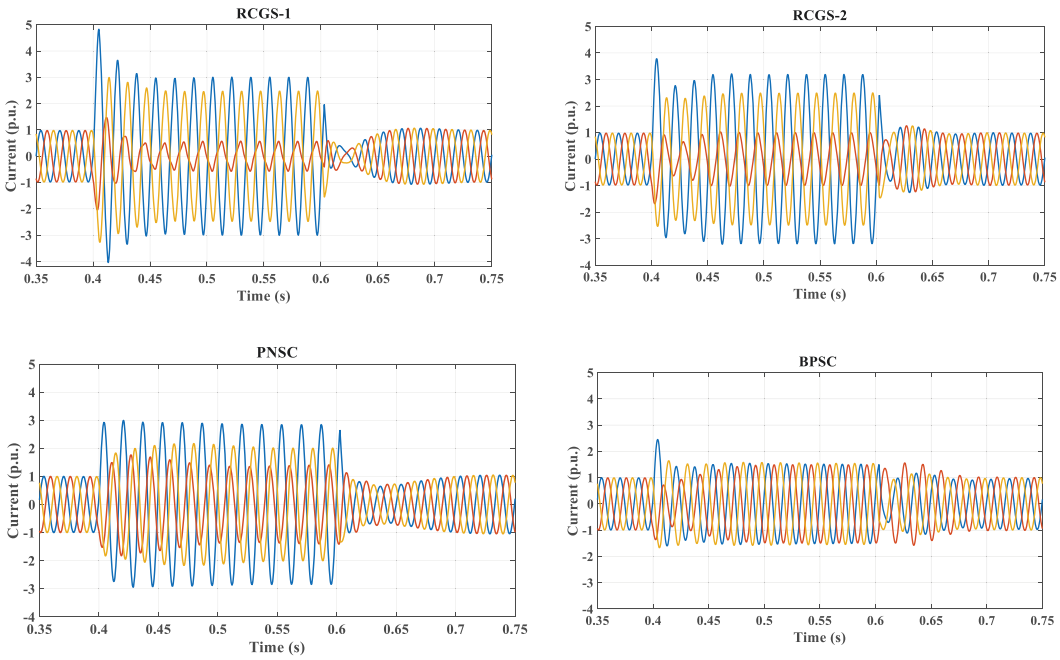

Figure 2.4 Three-phase current results of the LVRT behavior with four RCG strategies.

The short-circuit ratio (SCR) is a standard definition to quantify the strength of an ac system as compared to the rating of the connected VSC [26]. If the ac network impedance at the fundamental frequency is considered as Z_s, and the rated ac voltage and power of the VSC are V_{rated} and P_{rated}, respectively, then the SCR is defined as $SCR = \frac{V^2_{rated}/Z_s}{P_{rated}}$ [33]. System SCR is almost constant during this case study. Based on [26], a strong grid is known with the SCR higher than 3, and in a weak grid, the SCR would be between 2 and 3. Even though the SCR is obtained using steady-state values, it represents a measure of how bus voltages are affected during the dynamic system events [63]. Therefore, in the next sections, the performance of the system is also studied with the consideration of different grid strengths.

2.3.2 State-Space Model Validation

To show the validity of the obtained state-space models, the time-domain response of the state-space model with the BPSC strategy is compared to the time-domain response of the nonlinear model simulated in MATLAB-SIMULINK. Figure 2.5 shows a comparison of the positive *d*-axis current of the detailed nonlinear model

and that of the state-space model. In Figure 2.6, the negative *d*-axis current results are also shown for the same case for a comparison between two models. Both figures show that the proposed state-space model is successfully accurate as the two traces are nearly identical.

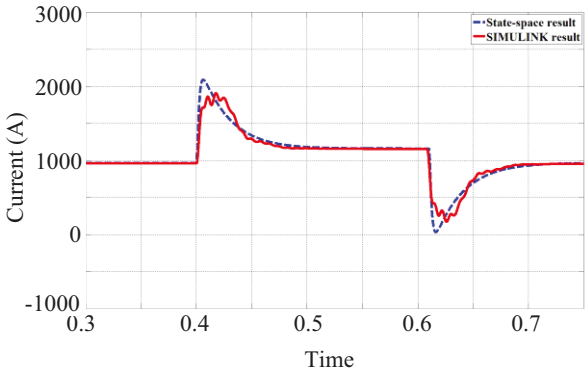

Figure 2.5 Positive d-axis current for one-phase-to-ground fault between t=0.4 s to t=0.6 s.

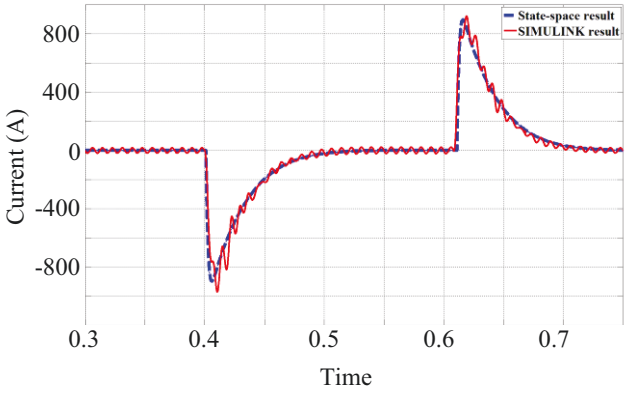

Figure 2.6 Negative *d*-axis current for one-phase-to-ground fault between t=0.4s to t=0.61s.

2.3.3 Case Study 1: Small-Signal Stability Analysis of Systems with Different X/R Ratios

As presented in [33], the maximum power transfer by the GCC depends on the angle of the ac system impedance. Thus, the effect of the variation of the X/R ratio of the system in the performance of the presented strategies is studied in this case.

The eigenvalues locus for X/R variation from 10 to 1 for the BPSC and PNSC strategies with SCR=3 are shown in Figure 2.7. As illustrated, the BPSC strategy is more sensitive to X/R changes, and it gets unstable for X/R<2.6. Repeating this test for a stronger system with SCR=6 shows that the BPSC strategy remains stable

even for X/R ratio of 1. Using the PNSC strategy, the system is stable when X/R changes from 10 to 1, for both SCR=3 and SCR=6. As shown in Figure 2.7(b), the eigenvalue locus of the PNSC strategy for SCR=3 presents negligible changes in poles. The same study for the other two conventional controllers (RCGS-1 and RCGS-2) shows that these approaches also remain stable for this range of X/R ratio changes in SCR=3. Therefore, in case of low X/R ratio, the PNSC strategy and the conventional control methods will have more stable results in comparison to that of the BPSC in weaker grids (SCR≤3) [64].

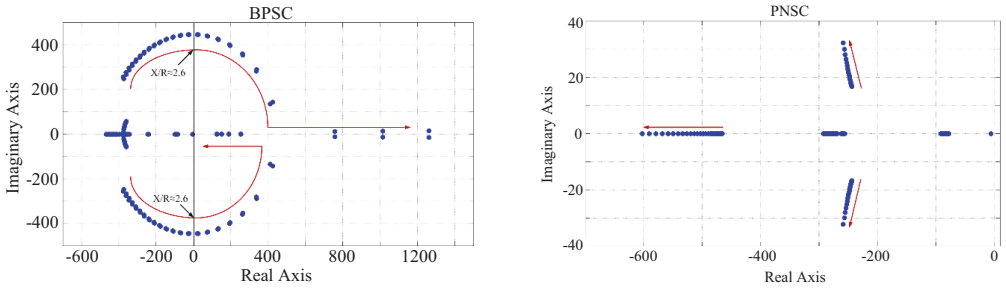

(a) (b)

Figure 2.7 Eigenvalue locus for X/R changes for (a) BPSC, (b) PNSC, SCR=3.

To verify the developed small-signal model, the simulation results of the non-linear model, for a GCC with the BPSC strategy are obtained. Figure 2.8 (a) and (b) demonstrate the GCC current in the dq^+ axes for the cases of connection to weak (SCR=3) and strong (SCR=6) grids, respectively. These results demonstrate the effect of different system SCRs in the case of low X/R ratio (i.e., X/R=1 for both cases). The results show instability in the case of the weak grid. However, the system is stable when connected to a strong grid with similar controller parameters. The simulation results of Figure 2.8 verify the conclusions obtained from the linear models.

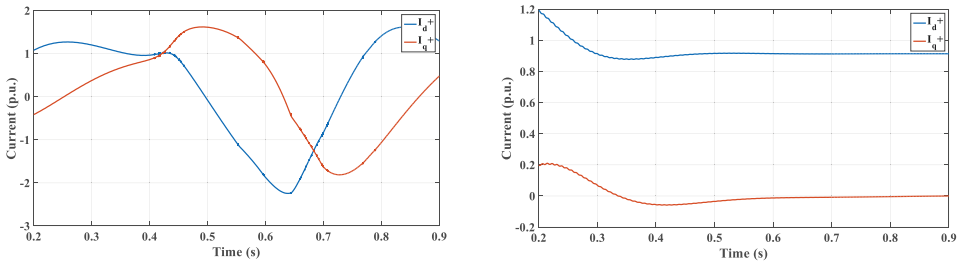

(a) (b)

Figure 2.8 The positive sequence current in the dq^+ frame for different system SCRs and low X/R ratio in BPSC when X/R=1 and (a) SCR=3, (b) SCR=6.

Additional studies reveal that the most dominant poles in the BPSC strategy that become unstable for X/R<2 are λ_{11}-λ_{14}. The PFA results for these eigenvalues are shown in TABLE 2.2. It is indicated that these eigenvalues are mostly dependent on the states x_3, x_4, x_7, and x_8,i.e., i_d^-, i_q^-, $\int e_d^- dt$ and $\int e_q^- dt$. These parameters are shown in Figure 2.2. As illustrated, all parameters affect V_c^-. In the BPSC strategy, positive sequence voltage is forwarded to the current reference generator; so, it is controlled by the current controller. Because the negative components of the PCC voltage are not forwarded to the controller, they are not controlled, and the system is highly affected by changing the X/R ratio. However, the PNSC strategy does not have this problem because both positive and negative components are controlled. Therefore, the system is not highly depended on the X/R changes in the PNSC strategy.

TABLE 2.2 Participation factor analysis on the most effective eigenvalues of the BPSC when X/R changes.

	X_1	X_2	X_3	X_4	X_5	X_6	X_7	X_8	X_9	X_{10}	X_{11}	X_{12}	X_{13}	X_{14}
$\lambda_{11,12}$	0	0	0.245	0.245	0	0	0.245	0.245	0	0	0	0	0.009	0.009
$\lambda_{13,14}$	0	0	0.25	0.25	0	0	0.25	0.25	0	0	0	0	0	0

The PFA for RCGS-1 shows that the effective poles when the X/R ratio changes depend on i_d and $\int e_d dt$, as presented in TABLE 2.3. Because the negative and positive sequences are not controlled separately, and because the effective parameter (i_d) is controlled by the current controller, the sensitivity of this system to the grid strength is considerably less than that of the BPSC strategy, as presented in Figure 2.7. Dominant poles of RCGS-2 show negligible variation with X/R changes.

TABLE 2.3 PFA on RCGS-1 most effective eigenvalues when X/R changes.

	X_1	X_2	X_3	X_4	X_5	X_6	X_7	X_8
$\lambda_{4,5}$	0.494	0	0.483	0.011	0.005	0	0	0.005

2.3.4 Case Study 2: Impact of the PLL Parameters and System SCR

It was shown in [33] that for low SCRs, the VSC performance is considerably affected by the PLL gains. However, a quantitative study is missing in the literature on GCCs performance with newly introduced RCG strategies under unbalanced and low-voltage conditions. Hence, an analytical study on the behavior of the GCC, with new RCG techniques under unbalanced and low-voltage conditions, is presented in this section.

The eigenvalue locus for the PLL gain K_{p2} that changes from 0.1 to 10 (with the steps of 0.1) is plotted in Figure 2.9. In these analyses, the operating point is P=1.0 pu, X/R=9 and K_{i2} is set to 5* K_{p2} for convenience in root locus plots [33]. As shown in Figure 2.9, the BPSC and PNSC strategies are more sensitive to K_{p2} changes when SCR=3; they get unstable from K_{p2}=1.4. From now on, this value is called $K_{p2\text{-}threshold}$. However, the other two conventional controllers are stable for this case until $K_{p2\text{-}threshold}$=2.8. Therefore, in the case of using the BPSC or PNSC strategies, lower PLL gain selection is necessary to guarantee the system stability.

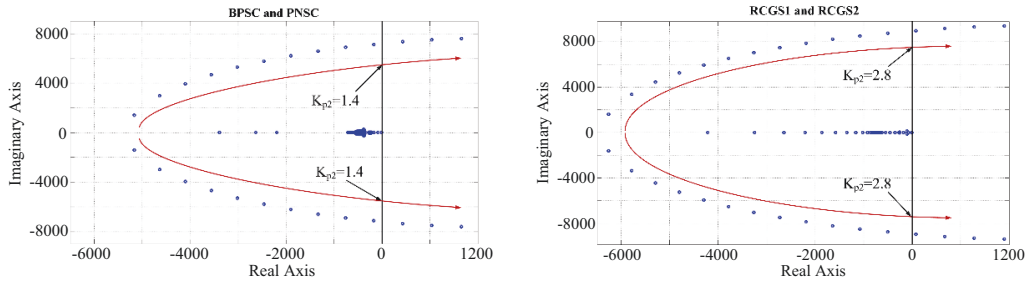

Figure 2.9 Eigenvalue locus for PLL gains changes for (a) BPSC and PNSC, (b) RCGS-1 and RCGS-2; when SCR=3.

When a converter is connected to a weak grid, the dynamics of the control system and stability issues become more complicated. Besides, because the GCC controller parameters are often designed considering the connection to strong grids, in the case of a weak grid the performance of the GCC control system would become problematic. In Case Study 1, the effect of changing the X/R ratio on system poles was studied. In this case, the value of the system SCR is changed while the X/R ratio is fixed at 10, and its effect on the system stability with different RCG methods is studied. TABLE 2.4 presents the results of the small-signal

analysis of four strategies with different system SCRs. It is observed that the improved RCG strategies are also more sensitive to the system SCR, i.e., they are unstable for very weak grids (SCR=1.3) even for very low K_{p2} values.

TABLE 2.4 PLL parameter change results

SCR	$K_{p2\text{-}threshold}$ in BPSC and PNSC	$K_{p2\text{-}threshold}$ in RCGS-1 and RCGS-2
1.3	unstable for all K_{p2}	0.9
2.2	0.4	1.9
3	1.4	2.8
6	stable for all K_{p2}	stable for all K_{p2}

The simulation results of the non-linear model for a GCC with the BPSC strategy is presented in Figure 2.10. The results show instability in the case of connection to a weak grid. However, the system is stable when connected to a strong grid with similar controller parameters. The value of K_{p2} is 2 in both cases. The results verify the conclusions obtained from the small signal analysis considering the effect of power system strength in designing the PLL control parameter.

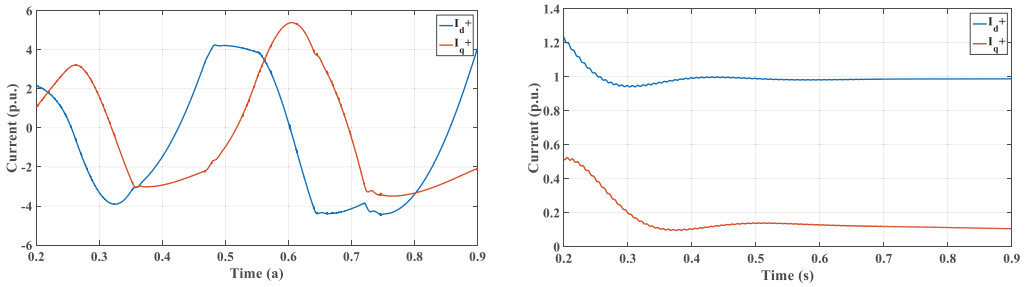

Figure 2.10 The positive sequence current in dq^+ frame for BPSC when K_{p2} =2 and (a) SCR=3, (b) SCR=6.

Applying the PFA on these controllers for K_{p2}=1 and SCR=3 shows that the sensitive poles for the BPSC and PNSC are λ_2 and λ_3 that are mostly dependent on x_2, x_9 and x_{12} as presented in TABLE 2.5. x_2, x_9, and x_{12} are dependent on i_q^+, $\int \omega\, dt$ and V_{fq}^+ respectively. V_{fq}^+ is the filtered feedforward signal from V_{pq}^+ that is fed into PLL as the control signal. V_{pq}^+ then contributes in controlling ω. i_q^+ is also affected

by V_{pq}^{+} as shown in (2.5). Therefore, it is reasonable for these poles to vary the most by changing K_{p2}.

The same study for RCGS-1 and RCGS-2 show that the most sensitive poles to the PLL parameters are λ_2 and λ_3 that depend on $\int \omega\, dt$ (i.e., x_5) and V_{fq} (i.e., x_8). The results for RCGS-1 are presented in TABLE 2.6. Therefore, changing PLL parameters in all methods affects the dominant poles that are highly connected with PLL signals. Thus, taking into account the results of TABLE 2.4 will help in keeping system stable for different SCRs.

TABLE 2.5 PFA on the BPSC and PNSC for PLL gains changes.

		X_1	X_2	X_3	X_4	X_5	X_6	X_7	X_8	X_9	X_{10}	X_{11}	X_{12}	X_{13}	X_{14}
BPSC	$\lambda_{2,3}$	0	0.198	0	0	0	0.036	0	0	0.306	0	0	0.459	0	0
PNSC	$\lambda_{2,3}$	0.008	0.194	0	0	0	0.035	0	0	0.309	0	0	0.451	0	0

TABLE 2.6 PFA on RCGS-1 for PLL gains changes.

	X_1	X_2	X_3	X_4	X_5	X_6	X_7	X_8
$\lambda 2$	0	0.033	0	0	0.228	0	0	0.738
$\lambda 3$	0	0.038	0	0	0.700	0	0	0.261

2.3.5 Case Study 3: Damping Ratio of Dominant Poles

The damping ratio, ξ, represents the rate of decay in the amplitude of oscillations. For an oscillatory mode denoted by a complex eigenvalue $\sigma \pm j\omega$, the damping ratio is defined as

$$\xi = \frac{-\sigma}{\sqrt{\sigma^2 + \omega^2}} \tag{2.16}$$

Considering the damping ratio for the dominant poles of the studied strategies, Figure 2.11 shows the results of the BPSC strategy. As presented, for the system with SCR=2.2, the PLL control parameter (K_{p2}) should be less than 0.4 to have $\xi > 0$. Also, in this case, ξ starts to decay from the beginning (i.e., K_{p2}=0.1) which represents an oscillatory behavior. However, for the system with SCR=3, the selected K_{p2} can be larger, and ξ starts to decrease from K_{p2}=0.3, which shows a non-oscillatory behavior for this mode before K_{p2}=0.3. For a stronger grid with

SCR=6, there is a negligible change in ξ, and it stays almost constant at 1. The same trends are observed for ξ in the PNSC strategy while changing K_{p2}. These results also confirm the obtained results in Case Study 2 for the PLL parameters change.

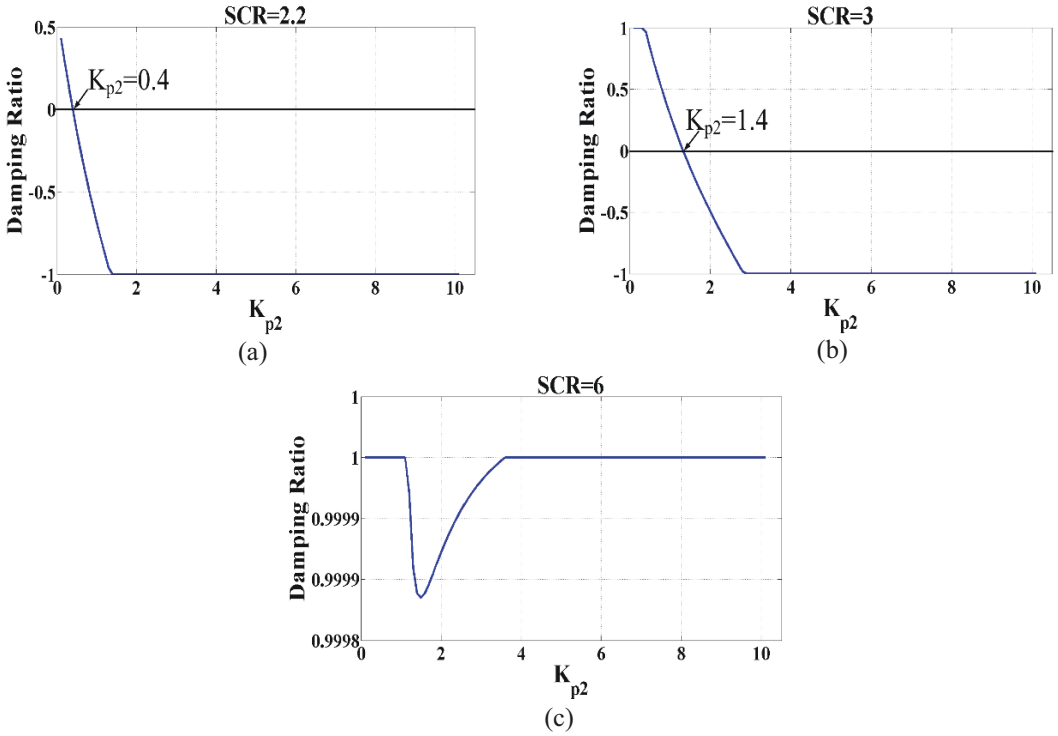

Figure 2.11 Damping ratio versus *Kp2* of BPSC for (a) SCR=2.2, (b) SCR=3 and (c) SCR=6.

Considering ξ when X/R changes, the results of Figure 2.12 and Figure 2.13 are obtained for the BPSC and PSNC strategies, respectively. For the BPSC, it is illustrated that by increasing X/R, the damping ratio is also increased. Therefore, the system shows lower stability with lower X/R values.

For the PNSC strategy, Figure 2.13 reveals that for both SCR values, ξ remains almost constant close to 1. The minor changes show that increasing X/R results in higher ξ. These results again show the lower sensitivity to X/R changes in the PNSC in comparison to the BPSC strategy.

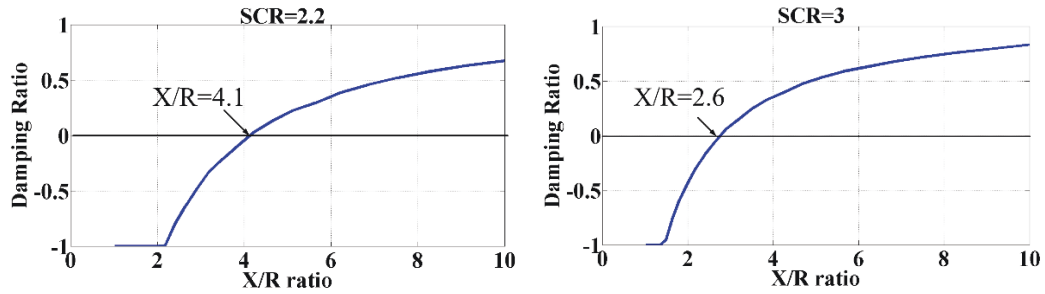

(a) (b)

Figure 2.12 Damping ratio versus X/R of BPSC for (a) SCR=2.2, (b) SCR=3.

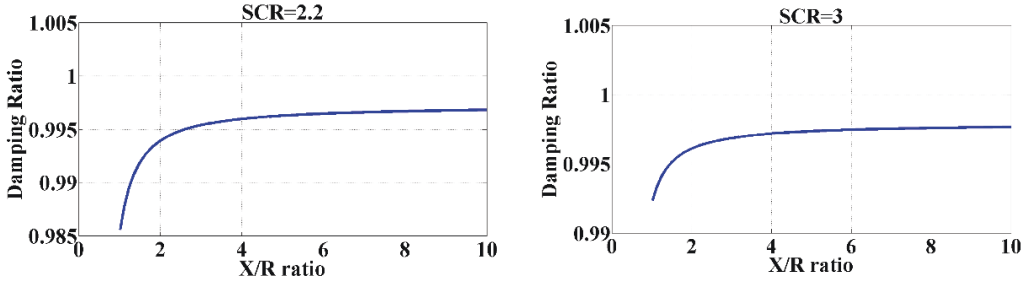

(a) (b)

Figure 2.13 Damping ratio versus X/R of PNSC for (a) SCR=2.2, (b) SCR=3.

2.3.6 Case Study 4: Maximum Phase Current of Four Strategies

Conventional controllers showed higher stability in the case of weak grids. However, one of the most important characteristics of RCG techniques, during the fault, is the maximum phase current value (I_{max}) which affects the protection tripping and LVRT failure. Therefore, in this case, the I_{max} characteristic during the fault is studied.

As presented in [39], the expressions of the I_{max} for the BPSC and PNSC strategies are as follows:

$$I_{\max_{abc},BPSC} = \frac{P^2 + Q^2}{V_{p+}^2} \tag{2.17}$$

$$I_{\max_{abc},\text{PNSC}} = \begin{bmatrix} \dfrac{P^2(V_2)^2 + Q^2(V_1)^2}{(V_{p+}^2 - V_{p-}^2)^2} \\ \dfrac{(V_2)^2\left[\frac{1}{2}P + \frac{\sqrt{3}}{2}Q\right]^2 + (V_1)^2\left[\frac{1}{2}Q + \frac{\sqrt{3}}{2}P\right]^2}{(V_{p+}^2 - V_{p-}^2)^2} \\ \dfrac{(V_2)^2\left[\frac{1}{2}P - \frac{\sqrt{3}}{2}Q\right]^2 + (V_1)^2\left[\frac{1}{2}Q - \frac{\sqrt{3}}{2}P\right]^2}{(V_{p+}^2 - V_{p-}^2)^2} \end{bmatrix} \tag{2.18}$$

where V_{P+} and V_{P-} stand for the positive and negative components of the PCC voltage, respectively, and, V_1 and V_2 are:

$$V_1 = V_{p+} - V_{p-} \quad , \quad V_2 = V_{p+} + V_{p-} \tag{2.19}$$

The I_{max} expression for RCGS-1 is as follows:

$$I_{\max,\text{RCG1}} = \frac{\frac{2}{3}P^*}{V_1} \tag{2.20}$$

Figure 2.14 illustrates the I_{max} values for these three RCG methods when SCR=6. As presented, the BPSC strategy has a considerable lower I_{max} value during the fault in comparison to the PNSC and RCGS-1. The maximum phase current value in the BPSC strategy is 1.19 p.u. while this value is 1.4 p.u. for the PNSC and RCGS-1. Therefore, although the BPSC shows more instability in weak grids when compared to the PNSC and the conventional controllers, it is a more reliable strategy to be chosen in the case of severe faults; because it presents lower I_{max} and decreases the chance of tripping in protection devices and allows to ride through such severe faults.

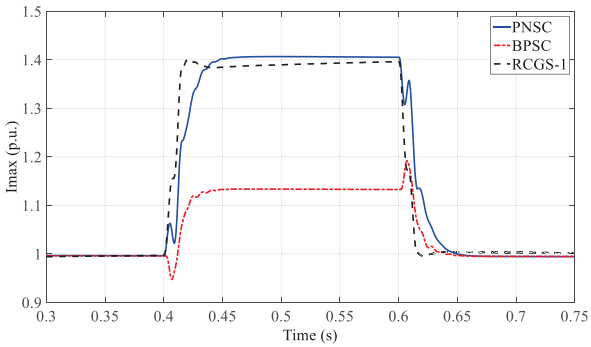

Figure 2.14 $I_{\max}$ for different RCG strategies.

2.4 Proposed Compensation Method to Improve the Transient Behavior

In this section, an improved current controller (CC) design is proposed using the obtained state-space model to improve the transient performance and reduce the maximum phase current in fault occurrence and clearance time. Typically, the design of the CC in the *dq* frame is based on considering the closed-loop CC as a first-order low-pass filter with unity gain and the time constant of τ_i as $G_i(s)=\frac{1}{\tau_i s+1}$ [24]. The simplified block diagram of the current-controlled VSC system in the positive and negative *d* axis is shown in Figure 2.15. The same block diagram applies to the positive and negative *q* axis. It is observed that the plant pole at $s=\frac{-R_f}{L_f}$, which is quite close to the origin, makes the magnitude and the phase of the loop gain drop from a low frequency. Therefore, in designing the compensator ($K_{PI}(s)$), a zero is set to $s=\frac{-K_i}{K_p}$ to cancel the plant pole. Besides, the loop gain is assumed to be $s=\frac{K_p}{L_f}$ to provide the mentioned $G_i(s)$ for the closed-loop transfer function. Therefore, in the traditional method, the values of K_p and K_i in the PI controller are selected as $K_p=\frac{L_f}{\tau_i}$, $K_i=\frac{R_f}{\tau_i}$.

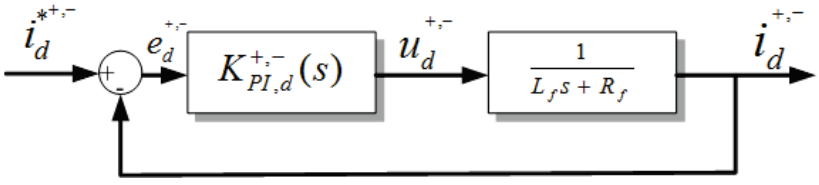

Figure 2.15 Block diagram of the current-controlled VSC system in the *d*+- channel.

However, as shown in Section 2.3, using the CC designed with this method presents a high maximum phase current in transients (Figure 2.4). To solve this problem, a new CC design method is proposed in this chapter. In the proposed method, the parameters of the four PI controllers, in the *dq*+- frame, are determined based on the eigenvalue analysis of the obtained state-space model. To find the

proper values of K_p and K_i, the eigenvalue locus of the system poles are studied in the following steps. First, the value of K_p is kept constant (i.e., $K_p = \frac{L_f}{\tau_i}$) while the value of K_i is changed with a coefficient (α) from 0.1 to 10. As presented in Figure 2.16(a), increasing the value of K_i moves the dominant poles toward the LHP which provides a more stable system. However, four farther poles have moved toward the right, and their imaginary part is also increased. Therefore, based on (2.26), the damping ratio (ξ) of these poles is decreased which can result in even higher over-shoots of current on transients in the BPSC.

In the next step, the value of K_i is kept constant on $K_i = \frac{R_f}{\tau_i}$, and the value of K_p is increased with the same coefficient. The result in Figure 2.16(b) demonstrates that the dominant poles move toward the RHP which is not desirable. On the other hand, the imaginary part of the four farther poles is decreasing faster. The desirable point about this case is that the imaginary parts of two of these poles decrease to zero which represent $\xi \geq 1$.

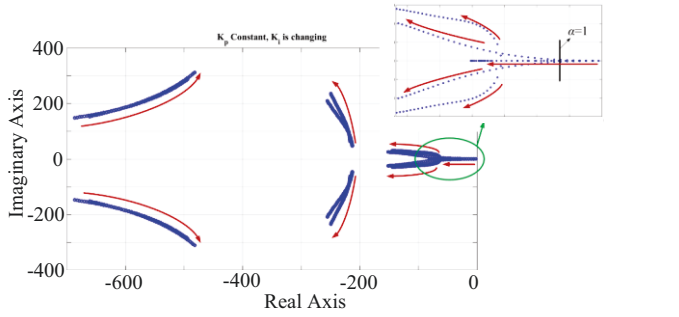

(a)

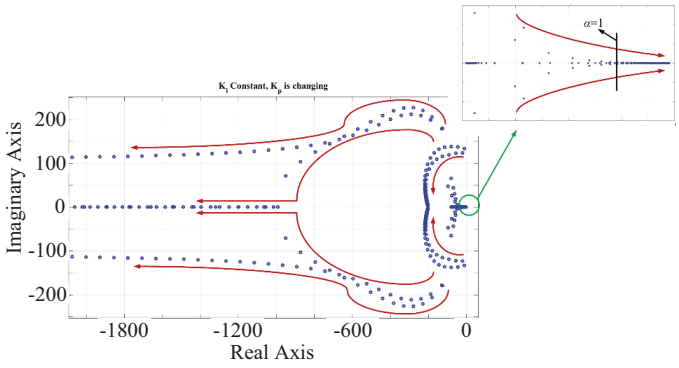

(b)

Figure 2.16 Eigenvalue locus of changing (a) only K_i, and then (b) K_i, in BPSC strategy

To obtain satisfactory results, it is proposed to combine two mentioned steps. First, the α coefficient of K_i is kept fixed on a selected value; then, both K_i and K_p are simultaneously changed with a similar coefficient (g) changing from 0.1 to 4 (i.e. $K_i = g \times \alpha \frac{R_f}{\tau_i}$, $K_p = g \frac{L_f}{\tau_i}$). The results for three different α values are shown in Figure 2.17. It is observed that as α increases, the most dominant poles move farther from the origin. The value of α=5 is selected here because it has moved the dominant poles of the system far enough from the origin representing satisfactory stability.

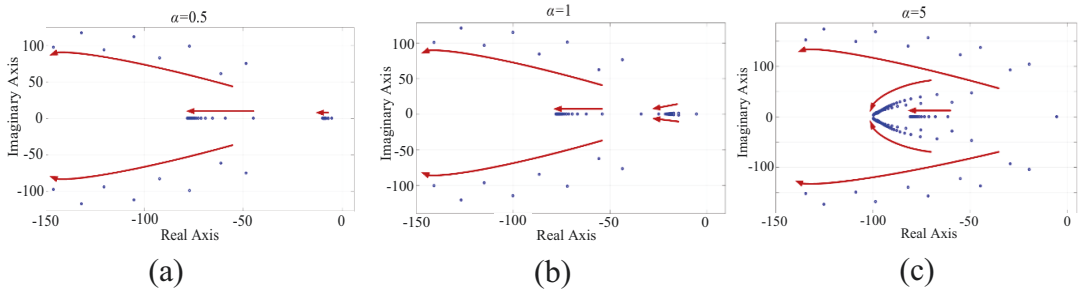

Figure 2.17 Eigenvalue locus for most dominant poles when (a) α=0.5, (b) α=1 and, (c) α=5.

The eigenvalue locus of the complete system poles are shown in Figure 2.18 for α=5 and g changing from 0.1 to 4. In this case, in addition to the movement of the most dominant poles toward the left (Figure 2.17(c)), the farther poles (representing the higher natural frequencies of the system) also move toward the left, as shown in Figure 2.18. This results in a higher damping ratio of the faster poles which solves the high over-shoot problem.

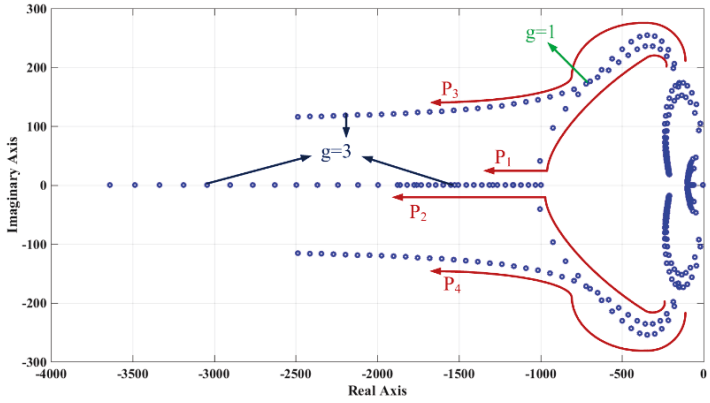

Figure 2.18 The eigenvalue locus of the complete system poles when α=5.

The damping ratio changes of the demonstrated poles of Figure 2.18 (P_1 to P_4) are presented in Figure 2.19. The value of ξ, which is obtained from (2.26), is increased and for g>1.5 two poles (P_1, P_2) represent over-damped behavior, and the other two (P_3, P_4) show high damping ratio close to 1. Therefore, shifting P_1-P_4 to the left by increasing the value of g, decreases the maximum overshoot.

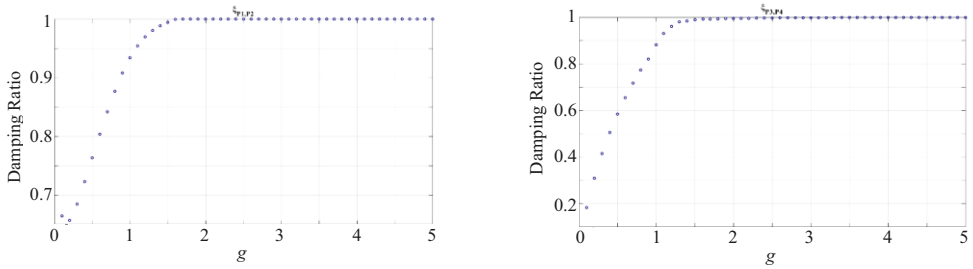

Figure 2.19 Damping ratio versus g coefficient for the fastest poles (a) P_1, P_2, (c) P_3, P_4

However, increasing the value of g is also restricted because of the limitation on the time constant of the current controller (τ_i). This time constant should be chosen enough smaller than the switching time of the switches (i.e., $\frac{1}{\tau_i} < 0.2\omega_{sw}$ [65] in which ω_{sw} is the angular switching frequency). Assuming a reasonable value for the VSC switching frequency of 5 kHz [24] the value of $\frac{1}{\tau_i}$ should be smaller than 6.28×10^3. Therefore, the value of the undamped natural frequency of the CC system (ω_n) should satisfy $\omega_n = \frac{2}{3}(\frac{1}{\tau_i}) < \frac{2}{3}(0.2\omega_{sw})$ [24]. ω_n represents the distance of each pole from the origin. P_1 has the maximum ω_n when g is increased. Therefore, the limitation, on increasing the value of g, is to keep the real part of P_1 lower than 4000. By choosing g=3, this limitation is satisfied.

The simulation results of the positive sequence current in the dq frame for the BPSC strategy are shown in Figure 2.20. Figure 2.20(a) illustrates the cases for two different g values while α=5. It is demonstrated that with g=3, the maximum overshoot value is considerably decreased in both fault occurrence and clearance incidents. It verifies the results obtained from the eigenvalue analysis and Figure 2.19. In Figure 2.20(b) the same signals are shown for different α values while g=3.

For the case of α=5, the transient oscillations are damped quickly and the settling time is remarkably improved.

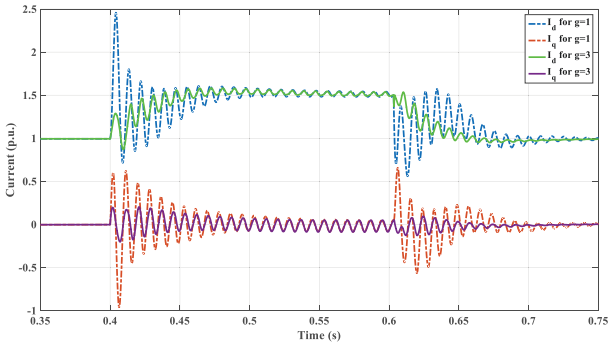

(a)

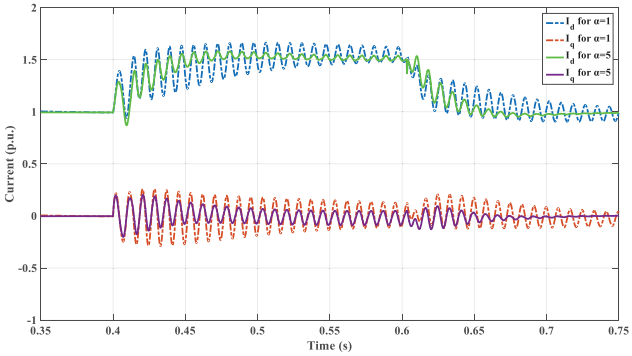

(b)

Figure 2.20 Positive sequence current in dq^+ frame for BPSC strategy with (a) different g values and, (b) different α values.

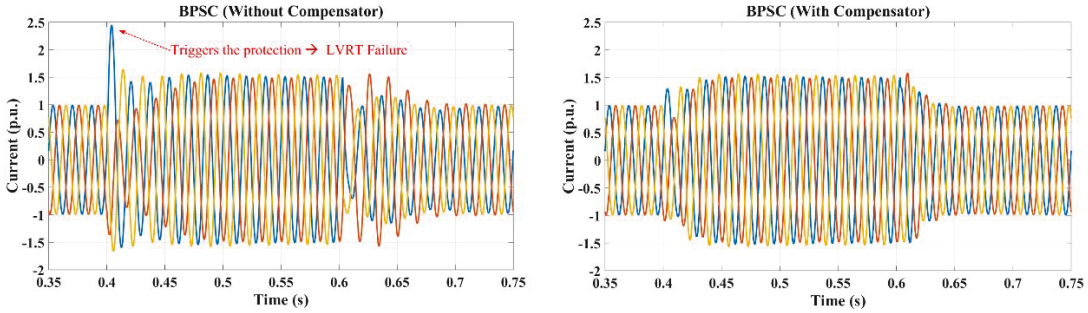

(a) (b)

Figure 2.21 Three-phase current results in BPSC strategy using: (a) CC without applying the compensator (b) CC with applying the improved compensator.

Therefore, a reasonable and effective choice for controller parameters can be $K_p = 3\times\frac{L_f}{\tau_i}, K_i = 3\times\frac{5\times R_f}{\tau_i}$ (i.e., α=5 and g=3). The improved results of applying this CC in the simulation model for the three-phase sinusoidal current is shown in

Figure 2.21. As presented, the high phase current value on the fault occurrence is removed, and the system also represents a considerably faster response.

2.5 Experimental results

The improved and traditional RCG strategies are validated using a scaled down 1.0 kVA laboratory prototype as shown in Figure 2.22. The key components for the laboratory setup are a dSPACE DS1104 real-time control system, three-leg VSC (a Semistack intelligent power module, which includes gate drives, six insulated gate bipolar transistors (IGBTs), and protection circuit), 60-Hz three phase grid, interfacing transformer, and a sensor box to sample the voltage and current of the PCC. The VSC inductor currents are measured by HASS-50-S current sensors whereas the voltages are measured by LEM-V-25-400 voltage sensors. The converter is interfaced to a dSPACE1104 control card using a CMOS/TTL interfacing circuit. The pulse-width modulation and the converter controllers are implemented on the dSPACE1104 control card supported with a TMS320F240-DSP coprocessor structure for switching signal generation. The dSPACE1104 interfacing board is equipped with eight digital-to-analog channels and eight analog-to-digital channels to interface the measured signals to/from the control system. The software code is generated by the Real-time-WorkShop under the MATLAB/Simulink environment. The grid stiffness is changed by connecting series inductors to the ac grid so that SCR at the PCC can be varied.

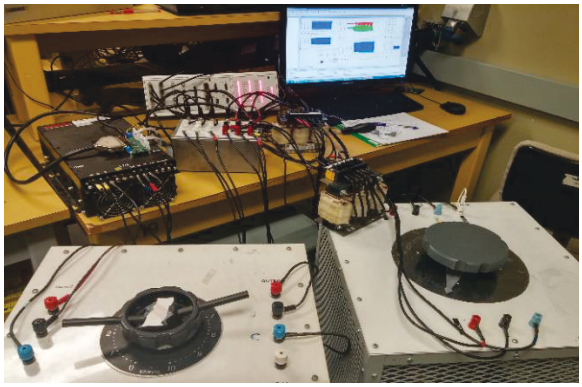

Figure 2.22 Experimental test setup.

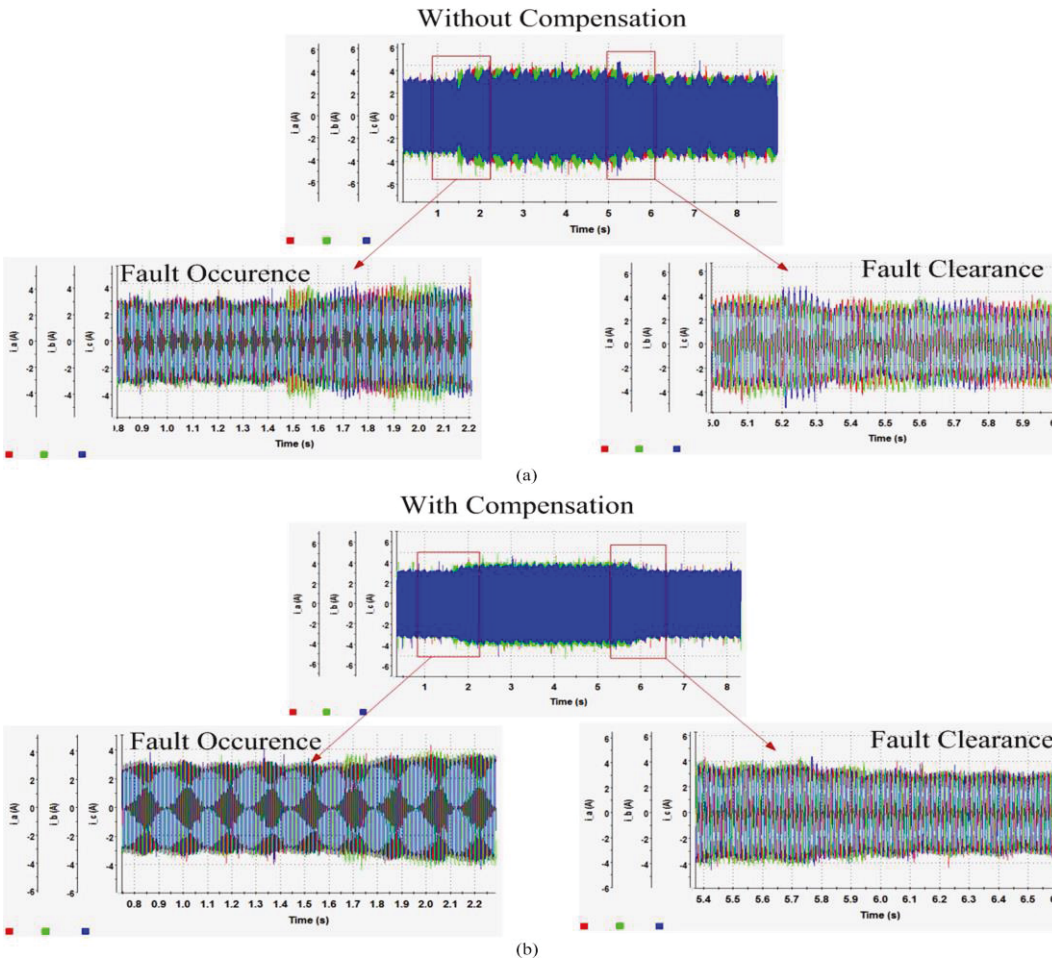

Figure 2.23 The effect of applying the proposed compensation method on BPSC behavior for fault transients in experimental setup: (a) without compensation, (b) with the proposed compensation method.

2.5.2 System Performance with the Proposed Compensator

The performance of the system with the BPSC RCG method is investigated in the experimental setup using both traditional and the compensated CCs, proposed in Section V. The system experiences a single-phase-to-ground fault for 4 s. The compensation coefficients are chosen as g = 1 and α = 2 to prevent high current transients. As shown in Figure 2.23, both the magnitude and oscillations of the converter current in both fault occurrence and fault clearance are reduced using the proposed compensation method. Considering the limitation on the maximum current of the converter switches and other protection fuses in the system, these high phase values on the current can trigger the protection systems and result in a

failure in LVRT. Therefore, the experimental results also reveal the capability of the proposed compensation method in enhancing the system performance under unbalanced fault conditions.

2.5.3System Performance under Different PLL Parameters

It is shown in Section 2.3.4 that the system stability is higher when lower *PLL* parameters (K_{p2} and K_{i2}) are chosen. In this section, this fact is also illustrated using the experimental test system. Figure 2.24(a) shows the results of the BPSC strategy. It is observed that for lower K_{p2} (starts from K_{p2}=1) the system remains stable. Then, K_{p2} is increased gradually, and it is illustrated that the system has lost the stability for K_{p2}>25.

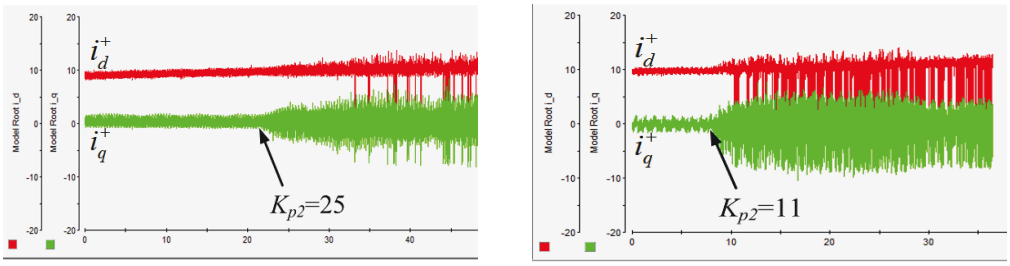

(a) (b)

Figure 2.24 The effect of increasing K_{p2} on experimental test system stability under (a) higher SCR and, (b) lower SCR.

2.5.4 System Performance under Different SCRs

As presented earlier, the system SCR should be considered in designing the system controllers. The effect of SCR on selecting *PLL* parameters is studied using the small-signal model. To validate the results, two different system SCRs are implemented in this section, and the previous tests of Subsection 2.5.3 are repeated. The results are presented in 2.5.4. It is again observed that in lower SCRs, PLL gain selection is more restricted, and K_{p2} has a lower threshold to maintain the system stability. For example, in this case, the system remains stable until K_{p2}=25 for higher SCR; but, for a system with lower SCR system loses its stability for K_{p2}>11. Therefore, in designing system controllers, the power system strength effects on selecting the PLL parameters should be properly considered.

2.6 Summary

Due to the increased penetration level of VSC interfaced resources, the utilization of interfacing VSCs to support host grids under unbalanced conditions (e.g., due to grid voltage unbalance, unbalanced load conditions and unsymmetrical faults) becomes essential. However, detailed dynamic analysis and systematic design procedure to enhance the dynamic performance of grid-connected VSCs equipped with grid-support controllers are not reported in the literature. To fill in this gap, this chapter presents a detailed small-signal model and analysis of the dynamics of a grid-connected VSC equipped with the recently developed balanced positive-sequence control and positive/negative-sequence control methods to support the grid under unbalanced conditions. The effects of the short-circuit ratio, angle of the ac system impedance, and phase-locked-loop parameters on the transient behavior of the VSC are thoroughly studied and characterized. Furthermore, to improve the dynamic performance of grid-connected VSCs, a simple yet effective current-control-based compensator is developed to mitigate possible instabilities associated with the low-voltage operation. Comparative simulation and experimental results validate the theoretical analysis and the effectiveness of the proposed compensation scheme.

Chapter 3

Improved LVRT Performance of Multiple DG Units under Unbalanced and Weak Grid Conditions

The distributed generation (DG) is an alternative and efficient method to supply electric power to customers in the modern electricity market. Nowadays, there is a growing interest in connecting more DG units to the utility distribution networks to satisfy the increasing demand, provide simplified and effective connections, and avoid the high investment costs for system upgrades. To gain DG advantages, the existing distribution and transmission systems are being used to receive and transfer power from one location to another. For an effective integration of DG units into the power networks, the low-voltage ride-through (LVRT) requirements have recently recommended for large DG installations [66], [67]. According to the existing grid codes, the grid-connected converters in DG units should withstand and remain connected during certain faults [18]-[20]. Therefore, several reference current generation (RCG) methods, based on the positive-negative sequence control strategy, are reported in the literature [6], [23], [66] to provide the LVRT requirements in the grid-connected voltage-source converter (VSC)-based DG units.

The stability analysis of a single DG unit with consideration of the LVRT requirements are studied in [25], [41], [49], [50], [67]. In [14]-[15], a multi-bus microgrid is studied in the islanded mode considering the voltage regulation with symmetrical components under unbalanced conditions. The negative-sequence current injection is presented in [41] and [68] to compensate for the unbalanced

load demands. The study in [69] presents a tuning method for the line drop compensator to control the coordination of a DG unit with other regulating devices in a multi-DG structure. However, the dynamic interactions among multiple DG units, controlled in the decoupled double synchronous reference frame (DDSRF) under unbalanced conditions, have not been addressed in the literature. The existing literature on multi-DG systems lacks the study of: (1) detailed analytical models for the grid-connected multi-DG system considering the recent RCG strategies in DDSRF; (2) an assessment of the interactions among DG units operating in different control modes and under different grid strengths; and (3) the dynamic analysis and performance improvement of the multi-DG systems equipped with advanced grid-support controls under unbalanced fault conditions. Therefore, to fill in this gap, comprehensive and detailed state-space models of a multi-DG system considering its DDSRF controllers for operation under unbalanced grid conditions, are developed in this chapter.

Although the small-signal model is usually used to assess the dynamic behavior of a power system around one operating point, the controllers developed in the small-signal sense enhanced the dynamic performance of the system even in the case of large disturbance [70]-[71]. To verify the effectiveness of the small-signal analysis, the designed systems can be tested under large-signal disturbances using the time-domain simulations. This approach is widely used in the power systems [70]-[73]. Therefore, the full characterization of the studied system is presented in this chapter by proposing the detailed linearized state-space models at three stages, i.e., before the fault, during the fault, and after the fault. The proposed modeling approach considers different operating points at these three stages to analyze the system dynamics on the fault occurrence and clearance. This model is used to 1) analyze the dynamic interactions of the multi-DG system with grid support capabilities in DDSRF, and 2) improve the control system designs.

In this chapter, using the developed models, the impacts of the following factors on the stability of the studied system are analyzed under the unbalanced fault conditions: (1) parameters of the current and voltage controllers, (2) the phase-locked loop (PLL) control parameters, (3) strength of the host grid, (4) control

modes of the DG units (e.g., PV or PQ control modes), (5) the connecting line parameters, and (6) the location of the fault. Furthermore, the proposed state-space models are used to provide an improved design and coordination of the control systems in the DG units by re-designing the parameters of different controllers considering a range of factors including the grid strength and the control modes of DG units.

Nonlinear models, for time-domain simulations, are implemented to verify the stability analyses and dynamic studies performed by the proposed state-space models. Finally, a laboratory-scale system is implemented to experimentally validate the dynamic performance analysis obtained from the developed models. The key results of the proposed models and control coordination guidelines, presented in this chapter, can be very useful for system integrators to characterize and improve the dynamic performance of the multiple grid-connected VSC-based DG units controlled in the DDSRF.

3.1 System structure and Control Strategy Principles

A single-line diagram of the understudy medium-voltage (MV) multi-bus distribution system is shown in Figure 3.1. This system is designed based on a typical Northern Ontario, Canada rural distribution system. It comprises a 10 MVA, 27.6 kV radial distribution system with two dispatchable three-wire 1.0 MVA, 480 V DG units. Studying a two-DG system as a model of an active distribution system with multiple DG units has been widely used in the literature [36], [74]-[75]. Unlike the study of a single-DG system, the two-DG system facilitates the study of the interactions between DG units and their effects on the entire system performance and stability. Also, the study of the effect of different parameters, in the power and control systems, on such interactions can be investigated. These aspects are thoroughly studied in this chapter using a detailed linear state-space model in the DDSRF. The modeling approach can be extended to systems with a higher number of DG units.

The DG units are connected to the MV feeder via step-up Y/Δ transformers. The system parameters are given in TABLE 3.1. The system line impedances (Z_0 to Z_3 in Figure 3.1) are characterized by their reactance to resistance (X/R) ratio which is a practical and typical feature in MV lines. The system loads are fed through two sub-feeders (Feeder 1 and 2) as shown in Figure 3.1. The DG units can supply any amount of positive- and negative-sequence currents within the pre-specified limits. The dc-side of each VSC is equipped with a combination of the main energy resource (e.g., a fuel cell) and a fast dynamic response energy storage system (e.g., a supercapacitor) so that the hybrid source provides an almost constant dc-bus voltage for the inverter [36], [59], [61], [75]. Therefore, the energy source of each DG unit is modeled by a dc voltage source. The loads do not absorb any zero-sequence and third-order harmonic currents from the MV feeders as they are connected to the MV feeders via Y/Δ transformers. The system loads are presented by their equivalent constant impedance models. This approach can effectively model typical distribution system loads with a simple impedance-based model with excellent accuracy [73].

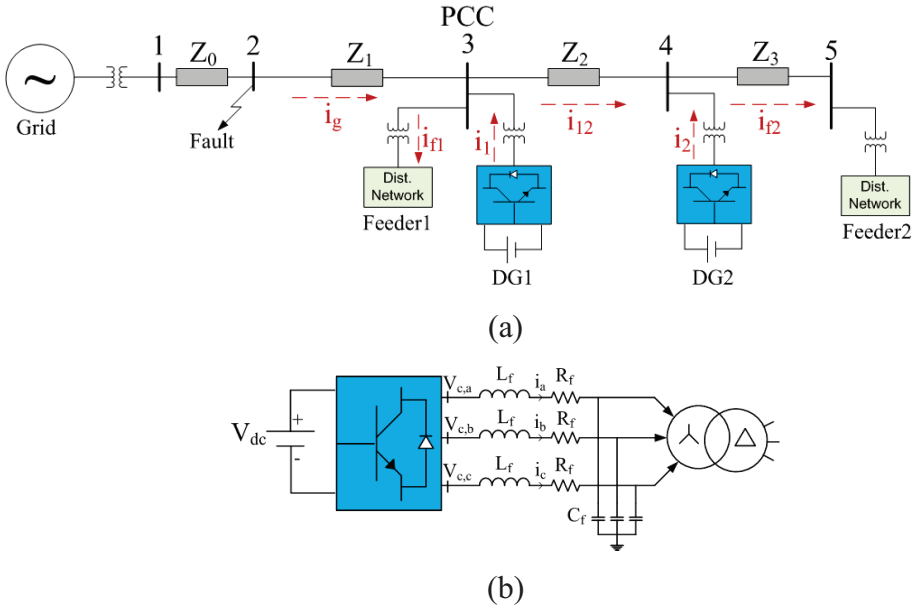

Figure 3.1 (a) The MV multi-bus distribution system under study (b) Structure of the converter-based DG units.

TABLE 3.1 System parameters

DG1 and DG2		Line Parameters		Load Parameters	
Rating	1.0 MVA, 480 V	Z_0	0.0068 + 0.0845i p.u.	P_{f1}	0.5 p.u.
V_{dc}	1.2 kV	Z_1	0.0017 + 0.0042i p.u.	P_{f2}	0.5 p.u.
C_{dc}	12 mF	Z_2	0.0086 + 0.0116i p.u.	Q_{f2}	0.1 p.u.
R_f, L_f	2 mΩ, 100 μH	Z_3	0.0048 + 0.0065i p.u.		
PI current control pameters, K_{p_init}, K_{i_init}		0.1, 2			
System rated voltage: 27.6 kV System rated power: 10 MVA (base power) System Short-Circuit Ratio (SCR): 8.5					

The balanced positive sequence control (BPSC) strategy [6], [39], [52] is selected in this chapter as the RCG method. This strategy is used to generate the inverter reference currents to deliver the demanded active and reactive powers, P^* and Q^*. Its advantage, in comparison to other available RCG methods, is the ability to generate a balanced and sinusoidal three-phase current during unbalanced network condition to provide the grid support [23]. The block diagram of the implemented control system on each DG unit is shown in Figure 3.2. The subscript "*meas.*" indicates the measured values.

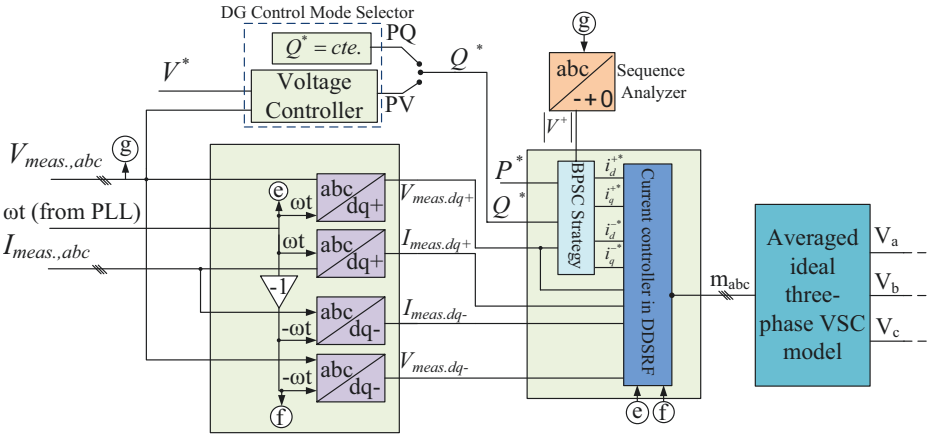

Figure 3.2 Structure of the implemented control system in DG units considering both traditional and improved RCGs and different DG control modes.

Each DG unit can operate in one of the PQ or PV control modes (CM). In the case of operation in the PV-CM, the reference reactive power Q^* is generated using a voltage controller unit, as shown in Figure 3.2. However, when the DG is operating in the PQ-CM, the value of Q^* is determined by the system operators.

The initial design of all PI controllers is done based on the methods presented in [24]. In the following sections, the control parameters of different controllers will be designed more accurately using the small-signal and eigenvalue analysis of the obtained three-stage dynamic model of the complete multi-DG system to ensure effective system operation.

3.2 State-Space Model

The three-stage linearized mathematical model of the studied distribution system (see Figure 3.1) is developed to 1) provide a more accurate design for the controllers considering the system dynamics and possible interactions among DG units, 2) investigate the effect of different DG control modes on the system stability improvement, 3) improve the stability performance of the system by differentiating the system dynamics before, during and after the fault, 4) examine the multi-DG system sensitivity to the control and system parameters variations, and 5) analyze the system dynamics in MV multi-DG system integration into power grids with different characteristics (particularly the connection to a weak grid).

3.2.1 Model Development

To develop a state-space model in the standard form of $\Delta \dot{X} = A\Delta X + B\Delta U$ and $\Delta Y = C\Delta X + D\Delta U$, first, the symbols of all currents and bus voltages are assigned as presented in TABLE 3.2. The directions of system currents are shown in Figure 3.1. In addition, to keep the equations more straightforward and to prevent any possible mistake due to the complication of the equations, the following mathematical method is used in this thesis to obtain the final state and input matrices:

$$\begin{aligned} &\Delta \dot{X} = A_2 \Delta \dot{X} + A_1 \Delta X + B_1 \Delta U \Rightarrow \\ &(I - A_2)\Delta \dot{X} = A_1 \Delta X + B_1 \Delta U \Rightarrow \\ &\Delta \dot{X} = \underbrace{(I - A_2)^{-1} A_1}_{A} \Delta X + \underbrace{(I - A_2)^{-1} B_1}_{B} \Delta U, \end{aligned} \tag{3.1}$$

Therefore, the final state and input matrices of the system would be $A = (I - A_2)^{-1} A_1$ and $B = (I - A_2)^{-1} B_1$, respectively.

TABLE 3.2 List of the system parameters in the state-space model.

V_g	Grid voltage (bus1 in Figure 3.1)	V_{P1}, V_{P2}	PCC voltage of DG1 and DG2, respectively
i_g	Current flowing from grid to DG1	i_{f1}, i_{f2}	Currents flowing to feeder1 and feeder2, respectively
i_{12}	Current flowing from DG1 to DG2	i_1, i_2	Currents flowing out from DG1 and, DG2, respectively
$e_{v_{P2}}$	The error between the reference and the measured PCC voltage at DG2	e_1,e_2	The error between the reference and the measured values of i_1 and i_2, respectively

For the case of DG1 and DG2 operating in PQ-CM and PV-CM, respectively, the system is modeled with 47 state variables, as follows:

$$\begin{aligned} X_{47\times1} = [&i_{gd}^{+}, i_{gq}^{+}, i_{gd}^{-}, i_{gq}^{-}, i_{1d}^{+}, i_{1q}^{+}, i_{1d}^{-}, i_{1q}^{-}, i_{2d}^{+}, i_{2q}^{+}, i_{2d}^{-}, i_{2q}^{-}, \\ &\int e_{1d}^{+} dt, \int e_{1q}^{+} dt, \int e_{1d}^{-} dt, \int e_{1q}^{-} dt, \int e_{2d}^{+} dt, \int e_{2q}^{+} dt, \int e_{2d}^{-} dt, \\ &\int e_{2q}^{-} dt, \omega_1, v_{p_1q}^{+}, \omega_2, v_{p_2q}^{+}, v_{f_1d}^{+}, v_{f_1q}^{+}, v_{f_1d}^{-}, v_{f_1q}^{-}, v_{f_2d}^{+}, v_{f_2q}^{+}, \\ &v_{f_2d}^{-}, v_{f_2q}^{-}, \int e_{v_{P2}}^{+} dt, i_{12d}^{+}, i_{12q}^{+}, i_{12d}^{-}, i_{12q}^{-}, i_{f2d}^{+}, i_{f2q}^{+}, i_{f2d}^{-}, i_{f2q}^{-}, \\ &v_{p_1d}^{+}, v_{p_1d}^{-}, v_{p_1q}^{-}, v_{p_2d}^{+}, v_{p_2d}^{-}, v_{p_2q}^{-}]^T \end{aligned} \tag{3.2}$$

and the input variable matrix is

$$u_{5\times1} = [\mathrm{V}_{gd}^{+}, \mathrm{V}_{gq}^{+}, \mathrm{V}_{gd}^{-}, \mathrm{V}_{gq}^{-}, \mathrm{V}_{P_2}^{*}] \tag{3.3}$$

in which V_{P2}^{*} represents the reference value for the voltage at the PCC of DG2 (bus4 in Figure 3.1). The linearized equations can be presented for four main control systems: 1) the PLL, 2) the current controller, 3) the RCG equations, and, 4) the voltage controller. The linearization process of the PLL, current controller and the RCG equation (the BPSC strategy) are based on the details in Appendix A. In the case of a DG unit operating in the PV mode, a voltage controller generates the Q^{*} value. The linearized PI voltage controller dynamics are as follows:

$$\Delta Q^{*} = K_{pV}\ \Delta e_v + K_{iV} \int \Delta e_v dt \tag{3.4}$$

where

$$\Delta e_v = \Delta V_{P_i}^* - \Delta(\sqrt{V_{P_i,d}^{+2} + V_{P_i,q}^{+2}} + \sqrt{V_{P_i,d}^{-2} + V_{P_i,q}^{-2}}) \quad (3.5)$$

in which K_{pV} and K_{iV} are the proportional and integral gains of the PI compensator and Δe_v represents the error between the reference and the measured voltages of the related PCC. The complete linearized matrices for the state-space model are presented in the Appendix B.

3.2.2 Three-Stages Modeling Method

Deriving linearized models for a grid-connected converter-based DG unit is fundamental to analyze its dynamic performance under grid faults and to coordinate different controllers. Under low-voltage conditions, a DG unit will be subjected to different operating conditions; hence, using one linearized model for these various conditions is not reasonable [76]. Therefore, a three-stage modeling method is adopted in this chapter. The first stage characterizes the DG unit dynamics before any fault occurrence. In this small-signal model, the initial condition is obtained from the normal DG unit operating condition.

The second stage considers the DG unit dynamics during the fault period. Therefore, the steady-state condition of this stage is obtained from the system status during any fault under study. Based on the type of the fault (one-, two- or three-phase to ground) and its severity (known by the phase voltage dip value) the small-signal model response will be different. This method provides the possibility of studying many different operating points for various fault conditions.

The third stage characterizes the system dynamics after fault clearance. The DG unit tries to return to the normal before-fault condition; therefore, the initial state of this stage is the final state obtained from the second stage, i.e., during-fault. The process of this three-stage modeling is depicted in Figure 3.3. This model also provides the possibility of studying the system performance on fault occurrence and clearance transients.

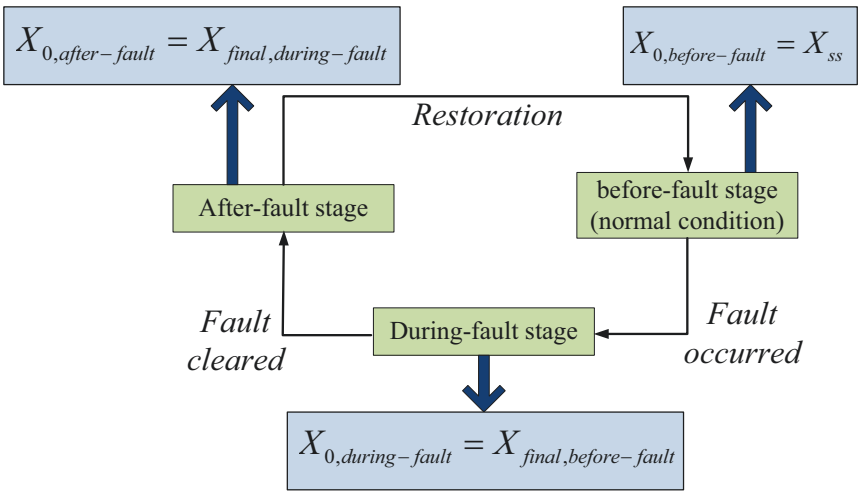

Figure 3.3 Process of the three-stage system modeling.

3.2.3 Model Validation

In Figure 3.4, the time-domain response of the obtained state-space model is compared to the time-domain response of the detailed nonlinear model simulated in Matlab-Simulink to verify the validity of the obtained dynamic model. The model validation results show excellent accuracy between the responses of both models. A sample case is shown in Figure 3.4, in which, DG1 operates in the PQ mode, and DG2 operates in the PV mode. The voltage reference of DG2 drops by 10% at t=3s. Figure 3.4(a) shows a comparison of the positive d-axis current of DG2 and Figure 3.4(b) illustrates the generated active power of the same DG. Both figures show the accuracy of the obtained state-space model where the responses are nearly identical.

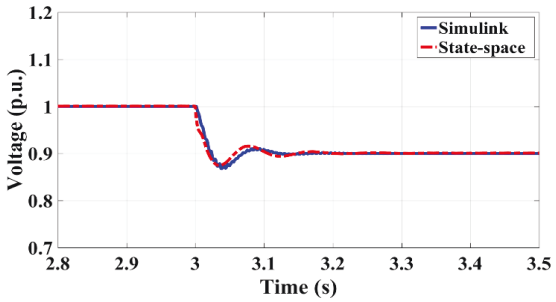

(a)

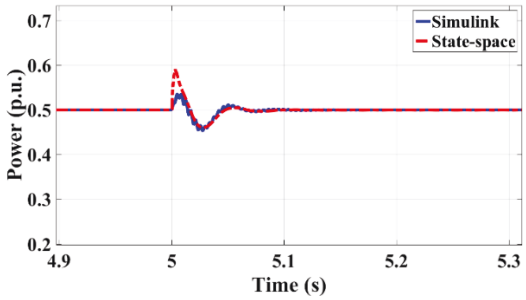

(b)

Figure 3.4 State-space model validation for (a) the positive *d*-axis current of DG2 and, (b) the generated active power on DG2.

3.3 Improved Design of Control systems

To consider the grid strength in the studied system behavior, two different grids with different SCR values are connected to the multi-DG system. In addition, three various control mode combinations on both DG units and four different fault locations are considered. TABLE 3.3 represents the details of different cases studied in this chapter for system analysis.

TABLE 3.3 Different cases considered in the system studies.

Analysis domain	a) Small-signal analysis b) Time-domain simulations
DG control modes (CM)	a) First CM: DG1 operates in PQ mode; DG2 operates in PV mode b) Second CM: DG1 operates in PV mode; DG2 operates in PQ mode c) Third CM: DG1 and DG2 operate in PV mode
Grid Strengths	a) Strong grid (SCR > 3) b) Weak grid (2 < SCR < 3)
Fault locations	a) Bus1 b) Bus2 c) Middle of the line between DG1 and DG2 (middle of Z_2) d) Bus4

To achieve an accurate design for system controller parameters considering the grid strength and mutual interactions among DG units, the eigenvalue analysis is performed on the three-stage small-signal model of the MV multi-DG system of TABLE 3.1 with the DG units configured in three different CMs. Two different cases for grid strength are studied as 1) strong (SCR=8.5), and 2) weak (SCR=2.5).

Figure 3.5 illustrates the effect of grid weakness on the system eigenvalues during an unbalanced fault with all controller parameters designed initially based on the methods presented in [24]. It is observed that when the connected grid is weak, the multi-DG system is initially unstable for the during-fault stage, with the poles placed in the right-half-plane (RHP). Therefore, a study should be conducted on improving the system stability to keep the multi-DG system stable in a weak grid condition.

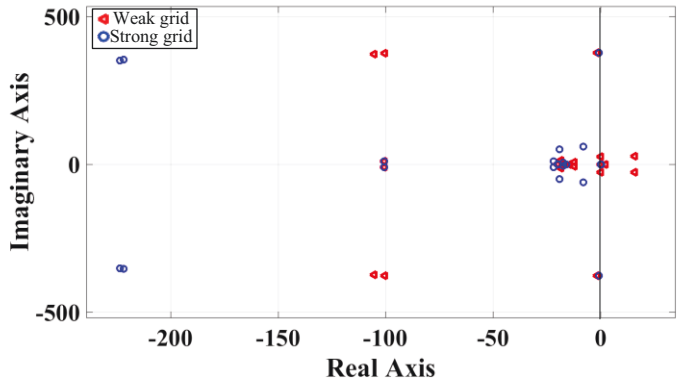

Figure 3.5 Effect of grid strength on system dominant poles during the unbalanced fault.

3.3.1 Current Controller Parameters Design

The initial design of the control parameters in the current controller is based on the pole-zero cancellation method described in [24]. However, this method is mainly developed for a simple single DG unit system connected to a strong grid. Therefore, in the first step, the effect of variation of the current controller PI compensator parameters in both DG units (i.e., K_{p_1}, K_{i_1}, K_{p_2}, and K_{i_2}) are studied. The key results for the before-fault stage are presented in Figure 3.6. In all CMs, for the strong and weak grids, increasing the current controller parameters with the same coefficient g_i (g_i increased from 1 to 9.5) in both DG units, results in moving the most dominant poles of the complete system to the left. It represents a more stable system in the case of sudden disturbances. When the connected grid is weak, there are two initially unstable poles which move toward the left-half plane (LHP) by increasing the g_i coefficient, as shown in Figure 3.6(b). Therefore, in the case of connection to a weak grid, the initial design of the current controller parameters may fail. These parameters should be modified (increased by the g_i coefficient) to

keep the system stable under disturbances. However, increasing the g_i more than 9.5 in these two cases, causes some initially non-dominant poles to move toward the imaginary axis representing a more susceptible system to the disturbances. The eigenvalue analysis results of this test case for the third CM are also shown in Figure 3.6(c) and (d). Therefore, in the case of the connection to a weak grid, in all CMs, selecting a higher g_i coefficient will guarantee the system stability.

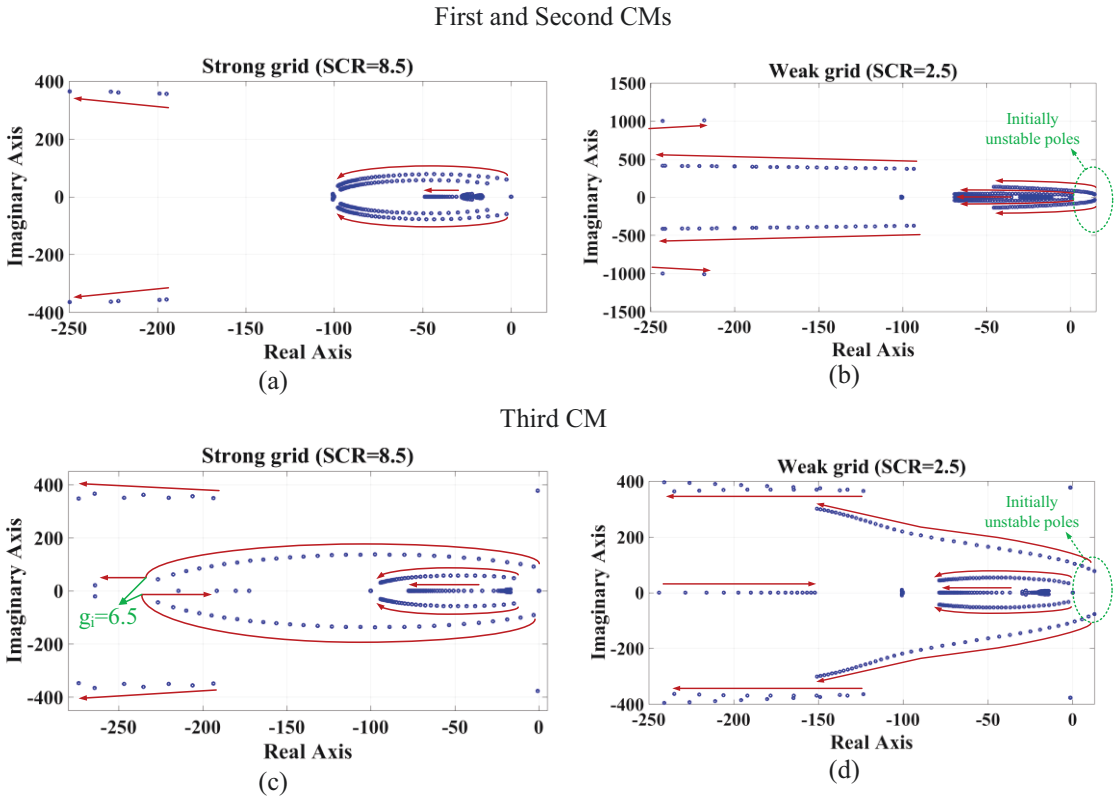

Figure 3.6 Eigenvalue locus of the current controller parameters tuning in all CMs considering strong and weak grid conditions.

When a fault occurs, the DG units are responsible for providing most of the load power. Therefore, it is essential to study the dynamic characteristics of the injected power of DG units. The obtained linearized models for the during-fault and after-fault stages are used to illustrate how the maximum overshoot value (MOV) of the active power in both DG units is reduced by modifying the current controller parameters in the first CM. The results are shown in Figure 3.7. It reveals that by selecting the suggested controller parameters, the transient response of both DG units considering their injected active power fluctuations is improved. The MOV is reduced by almost 62% and 83% on fault occurrence and clearance, respectively.

This is an important characteristic especially when there are sensitive loads connected to the DG units.

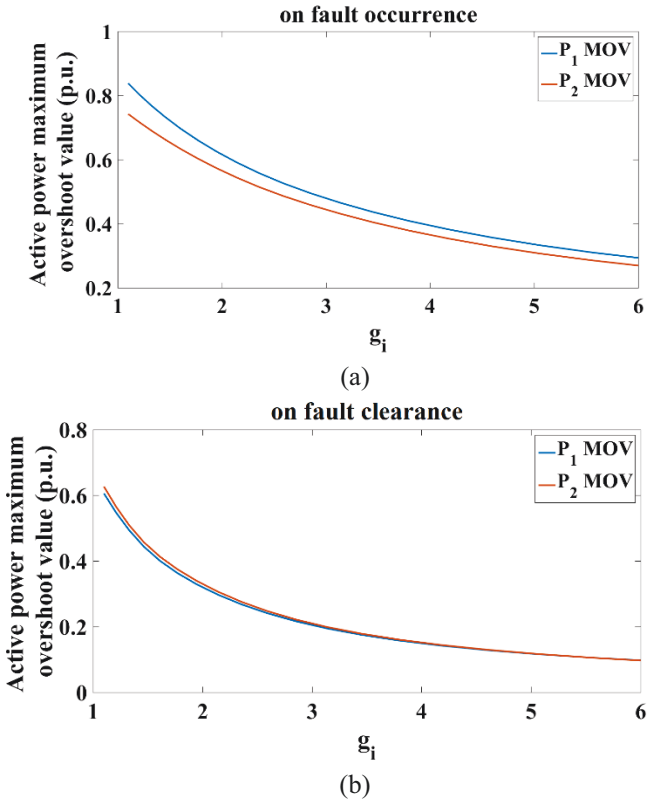

Figure 3.7 Impact of the suggested current controller parameters modification on the active power maximum overshoot value on (a) fault occurrence and (b) fault clearance.

3.3.2 Voltage Controller Parameters Design

After selecting the attained values in Section 3.3.2 for the current controller parameters (the most inner control loop), similar analyses are performed to select more accurate values for the voltage controller parameters (the first outer control loop) for different grid strengths. The initial parameters of the voltage controller are designed based on the standard approach presented in [24]. As demonstrated inFigure 3.8, in the first and second CMs for the strong and weak grids connection, increasing the initially designed value of the voltage controller PI parameters, with the gain of g_v, moves the most dominant poles to the left; until they reach a knee point demonstrated in Figure 3.8(a) and (b). This point is critical in the case of a weak grid from where the mentioned poles move back toward the right. Therefore, for connection to a weak grid, keeping g_v lower than three is recommended.

In the third CM, for both strong and weak grids, increasing the g_v coefficient after a certain point moves two of the dominant poles toward the right-hand plane. Therefore, in this CM, the initially designed voltage controller parameters should be increased carefully. In the next cases, g_v is set to 3 for all CMs.

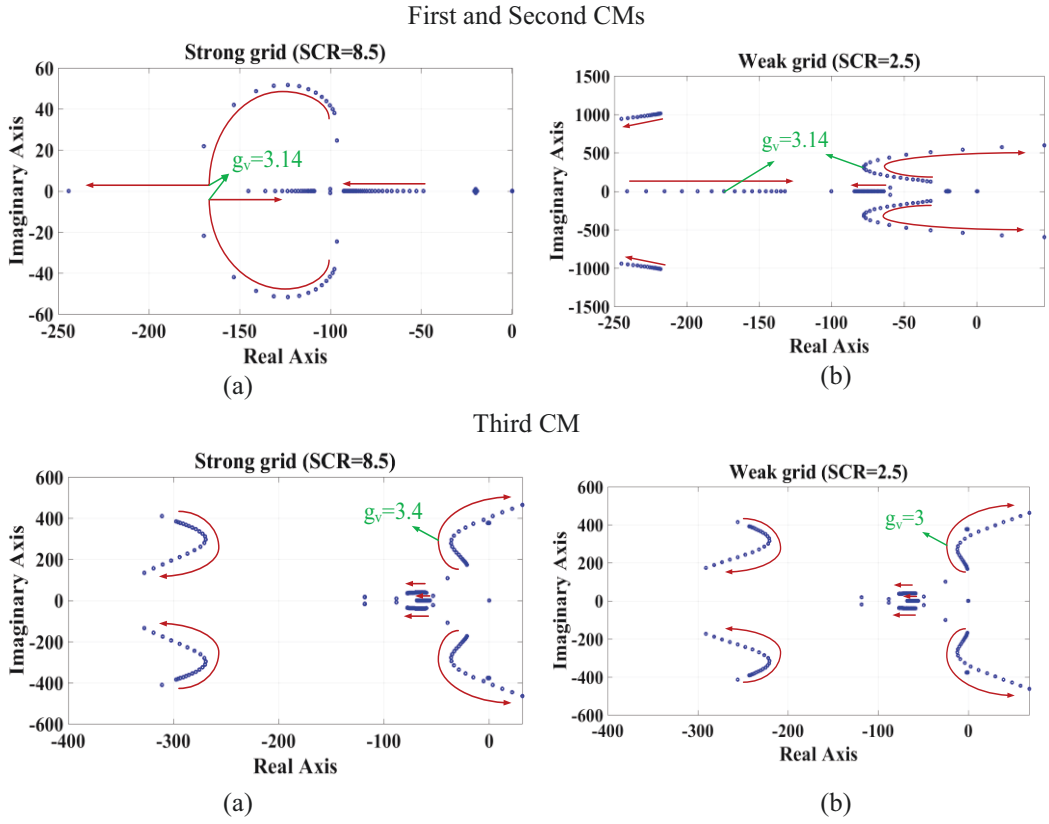

Figure 3.8 Eigenvalue locus of the voltage controller parameters tuning in all CMs considering strong and weak grid conditions.

Figure 3.9 shows the impact of the abovementioned voltage controller parameters modification on the MOV of the positive and negative PCC voltage components, based on the results of the small-signal analysis. These results are obtained using the linearized models for the during-fault and after-fault stages. It is observed that the MOV of the positive components are reduced by 3% and 10% on fault occurrence and fault clearance, respectively; whereas the MOV of the negative components remain low as they were in the initial case.

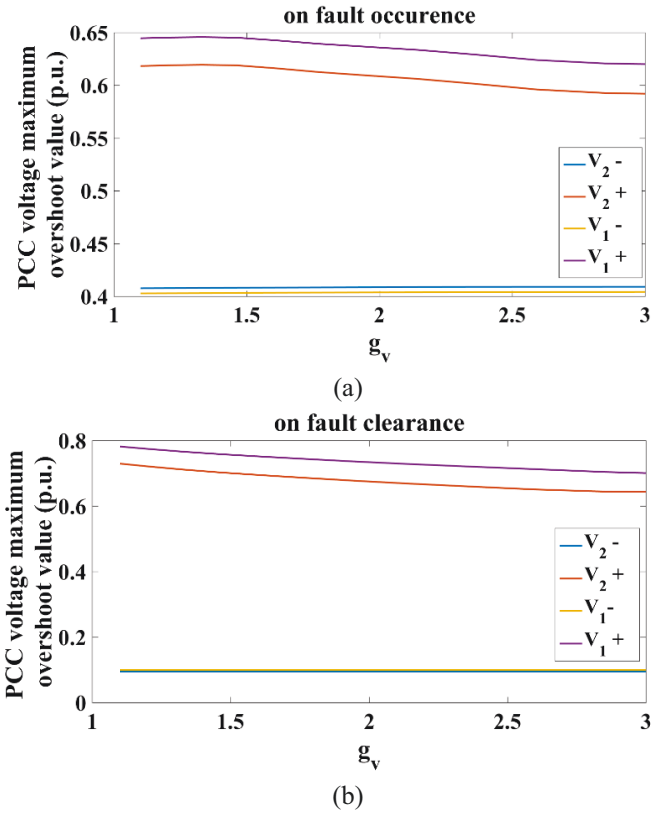

Figure 3.9 Impact of the voltage controller PI parameters modification on the maximum overshoot value of the positive and negative components of the PCC voltages on (a) fault occurrence and, (2) fault clearance.

3.3.3 PLL Controller Parameters Design

The study of the effect of PLL control parameters (i.e., K_{p_PLL} and K_{i_PLL} in both DG units) using the eigenvalue analysis is presented in this section. The PLL control parameter K_{p_PLL} is increased, starting from 0 (and setting K_{i_PLL} =5 K_{p_PLL} [33]), for different grid strengths in different CMs. For all CMs and in the case of a strong grid, increasing the K_{p_PLL} value to a certain point makes some of the most dominant poles slowly move away from the origin whereas keeping the left poles far enough from the origin. However, by increasing the K_{p_PLL} value in the case of a weak grid, although the same most dominant poles move toward left, the system becomes unstable when some other poles move to the RHP. Therefore, if the connected grid is not strong enough, keeping the initially designed PLL control parameters is more reasonable.

3.4 Time-Domain Performance Improvements

To verify the effectiveness of the proposed control parameters in enhancing the dynamic performance of the system under large-signal disturbances, the nonlinear time-domain simulation model is used. In the following tests, the DG units are operating in the first CM, the BPSC strategy is used as the RCG method, and the unbalanced fault location is on bus1 (see Figure 3.1).

Figure 3.10(a) shows the DG units currents when the system is connected to a strong grid (SCR=8.5), and the control parameters are designed based on the traditional methods of [24]. By connecting this system to a weak grid (SCR=2.5) and keeping the control parameters unchanged, the system shows instability during the fault, as presented in Figure 3.10(b). To verify the eigenvalue analysis results, the control parameters are modified, based on the results of Section 3.3, to move the most dominant poles to a more stable region. Therefore, as shown in Figure 3.11, by tuning the mentioned control parameters, the system presents a stable performance during the fault condition when the connected grid is still weak.

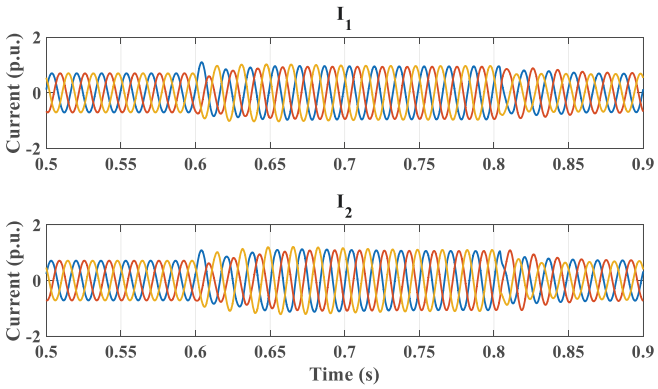

(a)

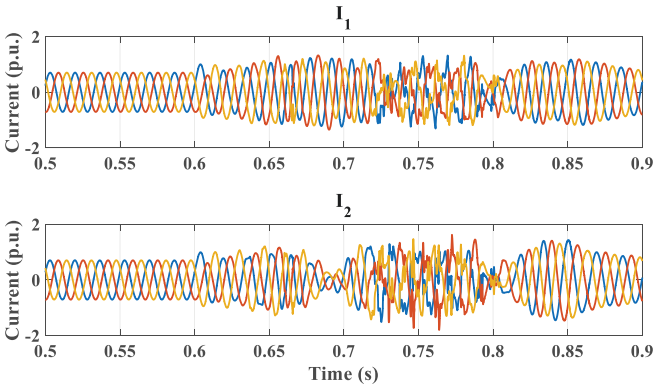

(b)

Figure 3.10 Effect of grid strength on the system performance under the unsymmetrical fault using the traditional control parameters design: (a) strong grid, (b) weak grid.

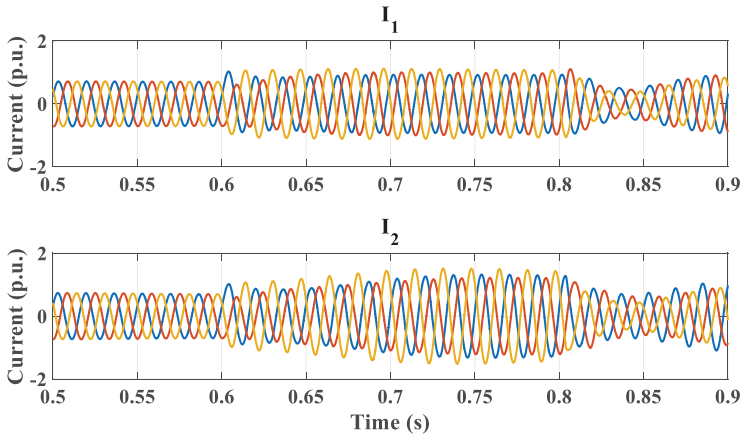

(c)

Figure 3.11 Effect of using the proposed control parameters in the first CM when connected to a weak grid.

Figure 3.12 illustrates the improvement in the transient performance of the PCC voltages and the active and reactive powers in both DG units by comparing the results of the initial and improved controller parameters design when the connected grid has SCR=4.

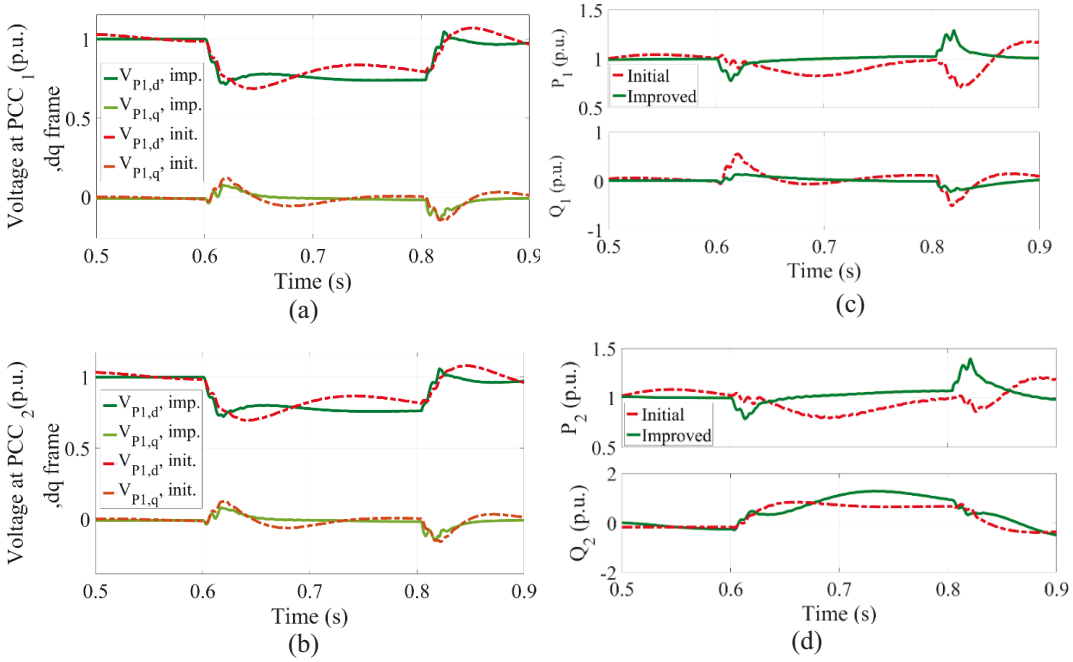

Figure 3.12 Effect of selecting the proposed control parameters in transient performance improvement of the PCC voltage of (a) DG1 and, (b) DG2, and in the active/reactive powers of (c) DG1 and, (d) DG2.

3.5 Sensitivity Studies

After control parameters modification as presented in Section 3.4, the small-signal analysis is used in this section to investigate the sensitivity of the multi-DG system to variations in the system parameters such as 1) different loading levels, 2) DG units operating power and, 3) different DG and fault locations. The detailed time-domain simulation model is used to verify the results of the developed linear model. Also, the time-domain model is used to perform the sensitivity analysis with respect to different locations of the unbalanced fault.

3.5.1 Effect of Loading Level

The total connected load to a multi-DG system may vary during the time; therefore, studying the effect of loading level variation on the complete system stability should be considered. To conduct this study, the total load connected to the system through feeders 1 and 2 is gradually changed from 0.2 p.u. to 1 p.u at a constant power factor of 0.98.The operating power of both DG units is kept constant at 0.2 p.u. The system SCR is 8.5 in all cases (i.e., connection to a strong grid). The results of the small-signal stability analyses showed that, in all CMs, one of the most dominant poles moves toward right representing lower damping factor for this pole. However, among all CMs, the second CM illustrated less sensitivity to the loading level variations. Therefore, in the case of having variable loads connected to the system feeders, setting the DG units on the second CM will yield better stability margins and transient response.

3.5.2 Effect of DG Operating Power

This study is conducted to illustrate the effect of variation in the operating power of a single DG unit, whereas the operating power of the other DG unit is kept constant. The results of this sensitivity analysis in the first CM are illustrated in Figure 3.13. In the first test case, DG1 is generating a constant amount of active power at 0.2 p.u. whereas the operating power of DG2 changes from 0.2 p.u. to 1 p.u., as shown in Figure 3.13(a). In the next study, DG2 is generating a constant

amount of active power at 0.2 p.u. whereas the operating power of DG1 changes from 0.2 p.u. to 1 p.u., as illustrated in Figure 3.13(b). The results reveal that changing the operating power of DG1, which is placed closer to the grid, shows a relatively higher effect in moving some of the dominant poles toward the right and so, affecting the relative stability margins.

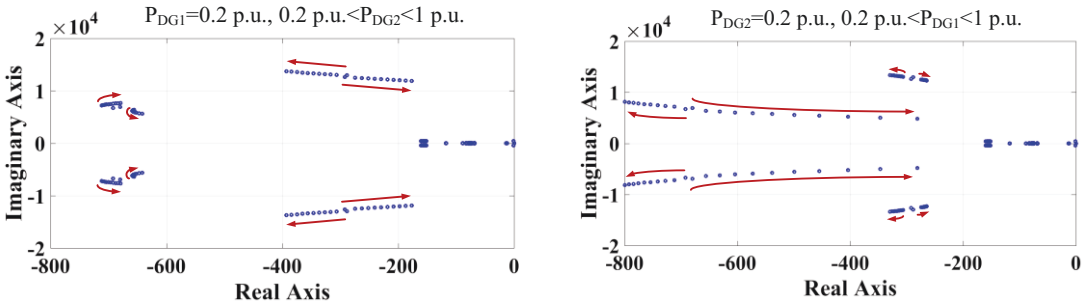

Figure 3.13 Eigenvalue locus of the effect of changing the operating power of only one DG in the first CM; a) P_{DG2} is changing, b) P_{DG1} is changing.

3.5.3 Effect of DG Location

One of the most important features in a multi-DG system is the study of the interactions among DG units and how they affect the whole power system performance. The length of the connecting line between DG units is considered as one of the effective system parameters in defining this interaction. Therefore, in this section, the influence of the length of the line between the DG units (i.e., Z_2 in Figure 3.1(a)) on the system dynamic behavior, for three CMs, is studied. The other lines characteristics are constant and SCR=8.5.

Figure 3.14 illustrates the eigenvalue locus of increasing the absolute value of Z_2 from 0 to 5 times its original value (shown in TABLE 3.1). As presented in Figure 3.14(a) and (b), in the first and second CMs, the illustrated system poles move toward left up to a certain point; however, in the third CM, the most dominant poles are not affected considerably.

In all CMs, increasing Z_2 means placing the DG units farther from each other. Hence, their interactions decrease which is the reason for the initial improvement in system stability. This result verifies the time-domain based results reported in

[77]. However, increasing the line length also results in higher loss and voltage drop along the line. Therefore, in the first CM, the voltage drop across the line reduces the ability of DG2 to keep its voltage at 1.0 p.u. Also, because the voltage at bus4 is not controlled in the second CM, a higher voltage drop in the line makes the system more unstable. However, because both DG units control their bus voltages in the third CM, the mentioned knee point happens at a very long length of Z_2.

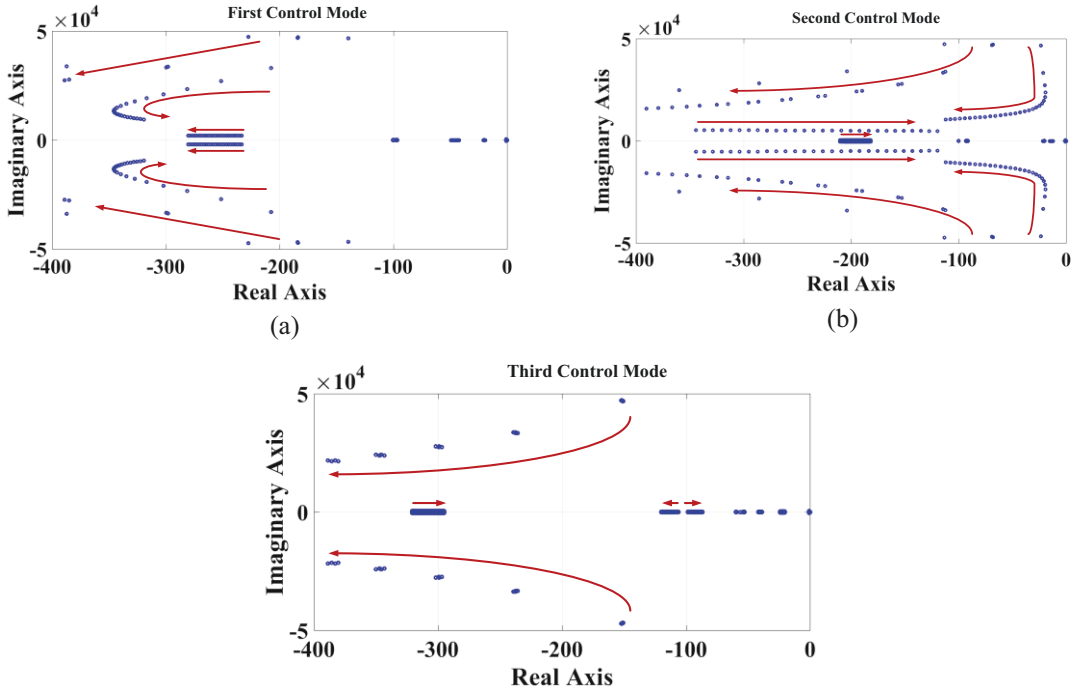

Figure 3.14 Eigenvalue locus of the effect of the length of the line between DG units in different CMs.

The effect of the length of the line between the DG units (Z_2) is also studied using the detailed nonlinear time-domain simulation model to verify the obtained results. First, in the second CM and in the case of connection to a strong grid, the length of Z_2 is increased to three times its original length. The results are shown in Figure 3.15(a) which show instability during the fault. However, changing the control mode to the third CM in the same test case keeps the system stable during the same fault (Figure 3.15(b)). Therefore, based on the results of both linear model and nonlinear simulations, in the case of a long line between two DG units, the third CM works best in maintaining the system stability during sudden transients such as unbalanced faults.

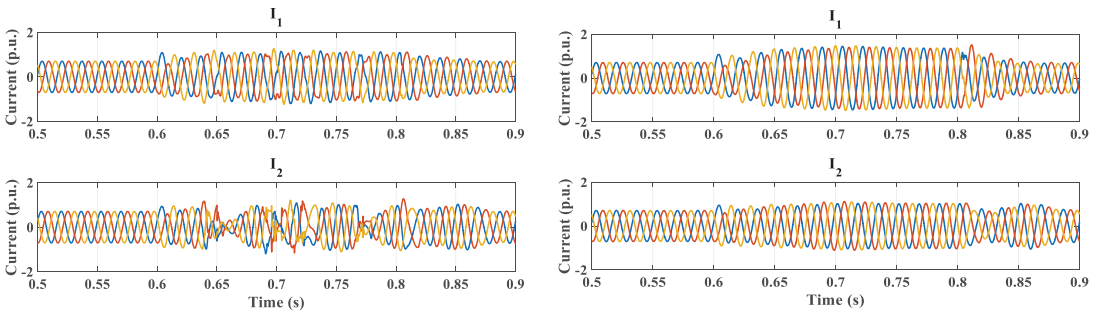

(a) (b)

Figure 3.15 Effect of a long line between the DG units in (a) second CM and, (b) third CM.

TABLE 3.4 Simulation results for three CMs under different fault locations

		Fault location			
		Bus1	Bus2	Mid. Z_2	Bus4
First CM	$I_{1,max}$ (p.u.); balance	0.96; B*	0.91; B	1.46; U*	0.87; B
	$I_{2,max}$ (p.u.); balance	1.09; B	1.38; B	0.88; B	1.45; U
	$I_{g,max}$ (p.u.); balance	1.94; U	2.04; U	9.29; U	8.66; U
Second CM	$I_{1,max}$ (p.u.); balance	1.19; B	1.57; U	1.58; U	1.54; U
	$I_{2,max}$ (p.u.); balance	0.90; B	0.89; B	0.89; B	0.89; B
	$I_{g,max}$ (p.u.); balance	1.87; U	2.10; U	9.35; U	8.65; U
Third CM	$I_{1,max}$ (p.u.); balance	1.12; B	1.29; B	1.27; B	1.18; B
	$I_{2,max}$ (p.u.); balance	0.87; B	0.91; B	0.93; B	0.96; B
	$I_{g,max}$ (p.u.); balance	1.84; U	2.05; U	9.34; U	8.63; U

* "B" stands for Balanced and, "U" stands for Unbalanced

3.5.4 Effect of the Fault Location in Different Control Modes

The same nonlinear time-domain model is used to perform a new study on the effect of the fault location on system performance. As mentioned before, in all of the previous tests the unbalanced fault occurred on bus2.

In this test, first, the unbalanced fault occurs in the middle of the line between the DG units (i.e., middle of Z_2), in three CMs. The results showed that during the fault, the first and second CMs represent a small unbalance on their current with the maximum phase current value (I_{max}) of approximately 1.5 p.u occurring in the DG operating in the PV mode. In the third CM, the value of I_{max} is lower, and both

currents remained balanced. Therefore, when there is a higher chance of fault occurrence between the DG units, the third CM may decrease the risk of activating the protection devices in the converter-based DG units due to over-current.

TABLE 3.4 summarizes the simulation results obtained for the four different fault locations mentioned in TABLE 3.3, in three studied CMs. It is observed that when the fault happens in the middle of Z_2 or on bus4, although the value of the maximum phase value in the grid current ($I_{g,max}$) becomes high, this value stays under 1.6 p.u. for the DG currents in all CMs. Also, in all studied fault locations, the third CM is the only mode in which both I_1 and I_2 remain balanced during the fault.

3.6 Experimental Results

The experimental test setup consists of the same main units described in Section 2.5. The grid stiffness is changed by connecting series inductors to the ac grid so that SCR of the studied system can be varied. For the strong grid condition, the SCR is approximately 5, and for the weak grid condition, the SCR is 2.5. In all test cases, the system is operated in the first CM, and it experiences a single-phase-to-ground fault for approximately three seconds. The sinusoidal three-phase value of i_1 and the PCC voltage in the positive and negative dq frame are shown for each test case.

Figure 3.16 Experimental test setup.

Figure 3.17 shows the effect of system strength on the design of the current

controller parameters. The initially designed values for K_p and K_i in both converters are 7.5 and 10, respectively. In the case of connection to a weak grid, decreasing the value of K_p parameters to 4.95 triggers the protection system and disconnects the converters. However, when the system is connected to a strong grid, the controllers operate properly, and the system stays connected during the fault. Figure 3.17(c) reveals that for a strong grid, the protection system is triggered when the K_p value is decreased to 1.56. These results verify the analytical studies of Section 3.3.

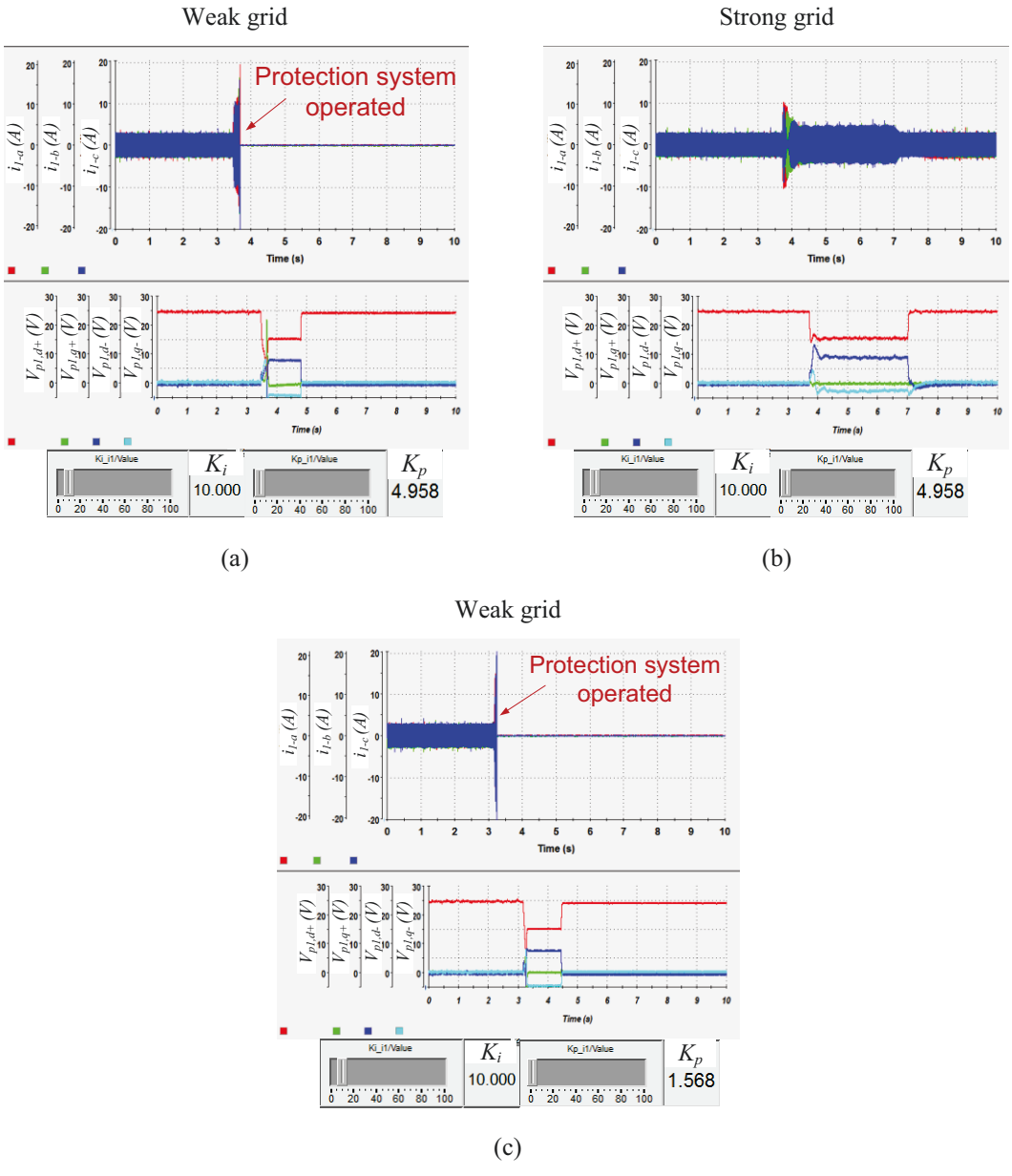

Figure 3.17 Experimental results showing the effect of system strength on designing the current controller.

The effect of the system strength on the design of the PLL parameters is presented in Figure 3.18. First, the same values of the PLL parameters are set for the connection to strong and weak grids. It is shown that in the case of a weak grid, both the current and voltage waveforms experience high oscillations during the unbalanced fault. However, in this case, selecting lower PLL parameters improves the system performance during the same fault. These results verify the analytical studies in Section 3.3.3 using the eigenvalue analysis on the small-signal model of the system.

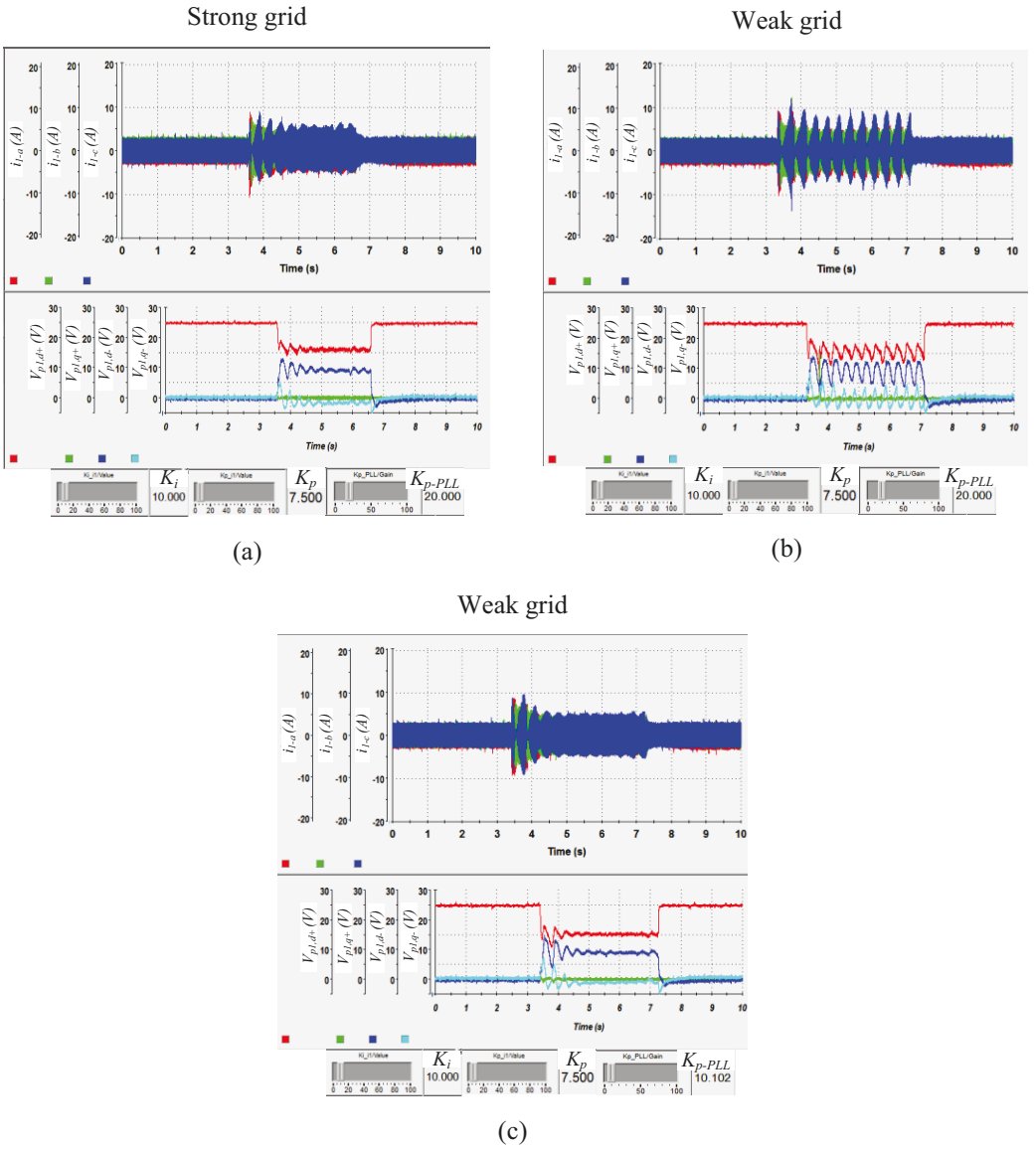

Figure 3.18 Experimental results showing the effect of system strength on designing the PLL parameters.

3.7 Summary

Due to the increased integration of multiple distributed generation (DG) units into the distribution network, riding through short-term faults and supporting the host grid have been requested by the new grid codes in many countries. However, the literature lacks the detailed dynamic analysis and control coordination of multiple grid-connected converter-based DG units, equipped with advanced controllers in the synchronous reference frame. To fill this gap, this chapter initially presents a detailed small-signal modeling framework for typical medium-voltage multi-bus power distribution systems with multiple DG units equipped with grid-support functions to operate under the unbalanced conditions. This model encompasses the positive and negative sequences of the current and voltage and is developed for three stages of the fault (i.e., before, during and after the fault) to cover a wide range of system operating points. In addition, to precisely study the interactions among DG units, four different control modes in DG units are considered to study the system dynamics under low-voltage and unbalanced conditions and at different grid strengths. Using the proposed detailed state-space models and based on the small-signal stability analyses, different control parameters are re-designed using the eigenvalue analysis on the complete multi-DG system. As a second contribution, sensitivity analyses are performed to study the effects of different system parameters, such as line characteristics, loading levels, and unbalanced fault characteristics, on the stability of the multi-DG system under unbalanced faults. Comparative simulation and experimental results are also reported to show the accuracy and effectiveness of the theoretical analyses.

Chapter 4

Enhanced Model-Based Control Design of GCC-Based DG Units Equipped with Flexible Grid-Support Controller

The capability of the LVRT is nowadays an important mandate for the converter-interfaced DG (CI-DG) units. To comply with the new grid code requirements, the CI-DG units are designed such that the active and reactive current injection to the grid is controlled independently by a grid-connected converter (GCC) considering the maximum current capacity of the converter [6], [25], [23]. As a conventional approach, the reactive current is injected as per grid code requirement, and any remaining capacity is utilized for the active power injection. However, in [25], it was shown that wind power plants might lose their synchronism with the grid fundamental frequency during severe faults. This, not only, does not support the voltage during the LVRT, but even worsens the situation. A phase-locked loop (PLL) frequency-based active current injection algorithm is then introduced in [25] to solve the loss of synchronism problem. The impact of the bandwidth of the dc and ac voltage controllers on the system stability during grid fault was studied through the small-signal analysis in [78]. In this study, time-domain simulations are carried out to guarantee the stability of the system in the case of large disturbances. However, neither [25] nor [78] studied the effect of any unbalanced grid fault on the LVRT performance of the GCCs.

The injected currents into the grid may include negative-sequence components to impede the effects of the unbalanced fault. The most common way to control a current vector with positive- and negative sequence components is to design the current controller based on two synchronous reference frames [6], [23], [78]-[80], with the value of their rotating frequency equal to the fundamental grid frequency but in the positive and negative directions.

In addition to the nonlinear dynamics of a GCC (e.g., due to the PLL), the presence of the reactive reference current generation proportional to the voltage dip magnitude adds more coupling between the converter injected current and the grid voltage at the PCC. However, the existing literature lacks the study of the modeling and dynamic analysis of the DG units equipped with the reference current generation (RCG) controllers based on the new LVRT standards [37], [40]. The new LVRT standards [37], [40] require the DG units to not only stay connected to the grid but also inject both positive and negative sequence reactive currents proportional to the unbalanced voltage sag characteristics under severe short-term unbalanced grid faults. In the following, this important requirement will be referred to as required positive- and negative-sequence injection and low-voltage ride-through (RPNSI-LVRT) requirement. The existing study in the literature on the dynamic behavior of the converters under unbalanced conditions [37], [41], only deals with the four conventional RCG techniques which none requires a certain amount of reactive current injection under the unbalanced faults. These conventional RCGs are only responsible for having the basic LVRT capability (and not the RPNSI-LVRT capability) which means the GCC is only required to stay connected under unbalanced conditions. In this sense, the RPNSI-LVRT capability has an additional requirement of injecting both positive and negative sequence reactive currents proportional to the unbalanced voltage sag characteristics. Therefore, in addition to the nonlinear dynamics of a GCC, the presence of the RPNSI-LVRT adds more coupling and complexity to the system in dynamic, transient, and stability studies. The presence of the RPNSI-LVRT requirement may lead to critical instability problems under different conditions, e.g., severe unbalanced faults, weak grid conditions, and conventionally tuned control

parameters. This is a significant difference between the conventional LVRT requirements [18]-[19] and the newly imposed RPNSI-LVRT requirement [37], [40] under short-term unbalanced faults. The flexible multi-sequence reactive current injection (FMS-RCI) technique [40] is presented to meet the RPNSI-LVRT requirement, which uses two control parameters (i.e., K^+ *and* K^-) to inject the positive- and negative-sequence reactive currents, respectively, proportional to the amount of the positive-sequence voltage drop and negative-sequence voltage rise.

To fill in the existing gaps in the literature and solve the aforementioned problems, the following contributions are accomplished in this chapter. In Section 4.1, a multi-stage linearized state-space model (i.e., before, during, and after the fault) is developed for a DG unit to analyze the dynamic performance and stability of the system under the RPNSI-LVRT requirement. This method provides the possibility of studying the imposed RCG methods before and during the unbalanced faults with different operating points. The impact of two coefficients, K^+, and K^-, in the FMS-RCI technique on the dynamic performance and the transient stability of the DG control system is studied in Section 4.2. A model-based control parameters design is then proposed, in Section 4.3, to find suitable values for K^+ and K^- parameters in weak grid conditions for stability purposes under RPNSI-LVRT requirements. The interactions between different converter controllers (e.g., current control and PLL) and FMS-RCI controller, in the DDSRF, is studied and their impact on the system stability is analyzed using the small-signal stability analysis. The parameters of the current controller are also designed based on the developed state-space model to have RPNSI-LVRT capability. In Section 4.4, the developed models and the proposed techniques are also applied to a more complex system with two DG units to consider the interactions between DG units on the RPNSI-LVRT performance of the entire system while using the FMS-RCI method. Finally, the proposed analytical design methods are tested using experimental test cases in Section 4.5. The results are promising and demonstrate the effectiveness of the developed models and proposed approaches in improving the stability of the DG systems under severe unbalanced faults when the RPNSI-LVRT is required by the grid code.

4.1 Converter-Interfaced DG Unit and the LVRT Requirements

Figure 4.1 represents a CI-DG unit which is designed based on a typical Northern Ontario, Canada rural distribution system. It consists of a 27.6 kV radial distribution system connected to a dispatchable three-wire DG unit. The system parameters are given in TABLE 4.1.

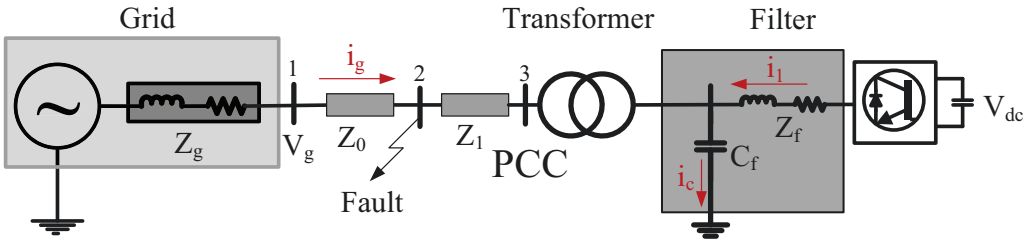

Figure 4.1 CI-DG unit.

TABLE 4.1 System parameters

DG unit		Line Parameters (p.u.)		System Parameters
Rating	5.0 MVA, 480 V			System rated voltage: 27.6 kV
V_{dc}	1.2 kV	Z_0	0.0068 + 0.0845i	System rated power: 10 MVA (base power)
C_{dc}	12 mF	Z_1	0.0017 + 0.0042i	
R_f, L_f	2 mΩ, 100 μH			Short-Circuit Ratio (SCR): 5.5

The grid frequency synchronization and active/reactive current control procedure are performed at the low voltage side of the GCC. The DG current controller is designed in the DDSRF on the *dq* coordinates, with the rotating frequencies in the positive and the negative directions with respect to the fundamental grid frequency; hence, it controls the positive- and negative- sequence current components.

During normal operation, the implemented current controller in the DDSRF receives its reference values based on the active and reactive power demands by the upstream system or the DG unit. Therefore, the reference currents are generated according to the equations presented in (1.2).

Based on the conventional LVRT standards on the voltage limits [18]-[19], the CI-DG system is supposed to follow the grid code requirements, presented in Figure

4.2, and remain connected to the grid when a fault occurs. The typical reactive current injection curve of this grid code is shown in Figure 4.2(b) which implies that in the case of a voltage sag less than 50%, the p.u. reactive current injection is proportional to the p.u. value of the voltage sag with the slope of 2. Besides, based on this grid code, when the voltage sag is more than 50%, the whole thermal limit is devoted to the reactive current injection (i.e., i_q=1 p.u.). Besides, according to this grid code for the Type 2 generating plants, which includes the system under study in this thesis, it is required that: "Three-phase short circuits or fault-related symmetrical voltage dips must not lead to instability above the Limit Line 1 in Figure 4.2 or to disconnection of the generating plant from the grid". However, this standard did not distinguish between the negative and positive components of the reactive current injection.

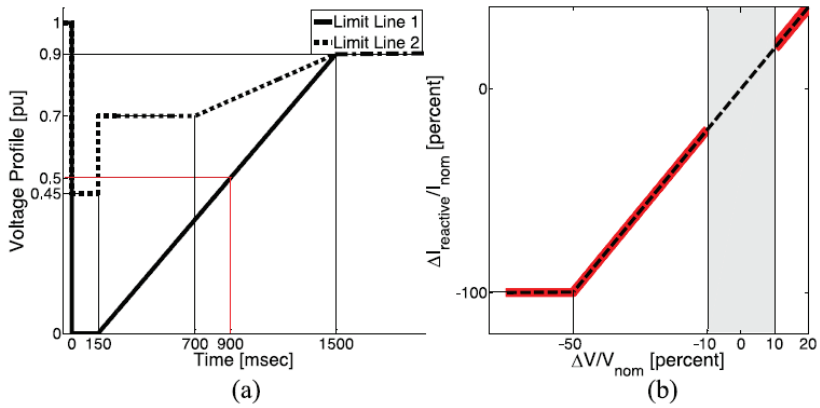

Figure 4.2 German E.ON. Grid code for LVRT [19] (a) voltage limits; (b) reactive current injection.

The injection of negative-sequence current has been recently presented in the German grid code, VDE-AR-N 4120 [37]. This code was published in 2015 describing the connection of generation plants to the high voltage network and, for the first time, requiring the negative sequence current injection by these units in the case of the unbalanced faults. As mentioned earlier, this is referred to as the RPNSI-LVRT requirement in this thesis. Under unbalanced grid faults, the classical synchronous generators provide short-circuit current which consists of the positive and negative sequence currents. On the other hand, DG units or transmission systems such as high voltage dc (HVDC) or flexible ac transmission systems

(FACTS) with a fully rated VSC usually repress the negative sequence current [81]. Generally, the converter of these units employs a decoupled current controller on positive and negative sequences. Therefore, the current objective is to independently control both sequence components to meet the requirements of the new grid codes. In this chapter, two different equations are used for the injection of the symmetrical components of the reactive current in each sequence. From now on, this method is called the flexible multi-sequence reactive current injection or FMS-RCI; which is obtained based on the recent German grid code [40]. As illustrated in Figure 4.3(a), the condition for the flexible positive sequence reactive current injection (FPS-RCI) is almost the same as the one imposed in Figure 4.2(b); but, the flexible slope of the ratio of the i_q^{*+} injection to the positive sequence voltage dip is defined as K^+.

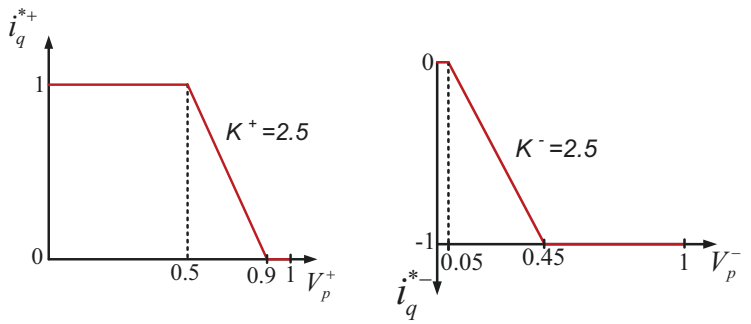

Figure 4.3 Reactive current injection based on the new grid codes [37]: (a) FPS-RCI, (b) FNS-RCIs.

On the other hand, the flexible negative-sequence reactive current injection (FNS-RCI) is proportional to the negative sequence voltage value when it is higher than 0.05 p.u. with the flexible slope of K^-. The whole criteria on both components for the case of $K^+ = K^- = 2.5$ can be expressed as follows:

$$FPS-RCI:\begin{cases} eq_1^+: \quad \Delta V_p^+ > 90\% \quad \rightarrow \quad i_q^{*+} = \dfrac{-2}{3}\dfrac{Q^*}{V^+_{pd}} \\ eq_2^+: \quad 50\% < \Delta V_p^+ < 90\% \quad \rightarrow \quad i_q^{*+} = K^+ \Delta V_p^+ \\ \qquad\qquad\qquad\qquad\qquad\quad = K^+(0.9 - V_p^+)_{p.u.} \\ eq_3^+: \quad \Delta V_p^+ < 50\% \quad \rightarrow \quad i_q^{*+} = 1\ p.u. \end{cases} \tag{4.1}$$

$$FNS-RCI:\begin{cases} eq_1^-: \quad \Delta V_p^- < 5\% \quad \rightarrow \quad i_q^{*-} = 0 \\ eq_2^-: \quad 5\% < \Delta V_p^- < 45\% \quad \rightarrow \quad i_q^{*-} = K^- \Delta V_p^- \\ \qquad\qquad\qquad\qquad\qquad\qquad = K^-(0.05 - V_p^-)_{p.u.} \\ eq_3^-: \quad \Delta V_p^- > 45\% \quad \rightarrow \quad i_q^{*-} = -1\ p.u. \end{cases} \tag{4.2}$$

For example, if the positive-sequence voltage drops below 50%, there will be 1p.u. of the positive-sequence reactive current injection. If the total magnitude of the injected reactive current (obtained from the positive and negative sequences) reaches the maximum thermal limit of the converter, the active current injection will be set on zero. Otherwise, the injected value of the active current sequences will follow the traditional equations of (1.2), still respecting the converter current rating. The schematic diagram of the FMS-RCI method is shown in Figure 4.4.

Any oscillation in the positive sequence of the PCC voltage (V_{pd}^+) appears in $\frac{\partial i_d^{*+}}{\partial V_{pd}^+}$ which is directly presented in the linearization of (1.2). Therefore, the RCG block is affected by the variations of the PCC voltage. This will take the system modes to the unstable region which may result in the operation of the protection devices and LVRT failure. Therefore, to improve the stability performance of the system, a low-pass filter (LPF) with the time-constant of 3 ms is employed on the positive sequence of the PCC voltage in the RCG block, as shown in Figure 4.4.

Because the RCG is an outer loop compared to the current controller, it should have a slower response time. Therefore, an LPF with the time constant of τ_1 is designed on V_{pd}^+ sampling to implement (1.2). The relation between the actual and the reference currents in *dq* frames, for both sequences, can be approximated by

$$i_{d(q)} = \frac{1}{\tau_i s + 1} i_{d(q)}^* \tag{4.3}$$

where τ_i is the time-constant of the closed-loop current controller [24]. Therefore, the value of τ_1 should be chosen carefully compared to τ_i. The effect of using the LPF on system stability will thoroughly be discussed in Section 4.3.2.

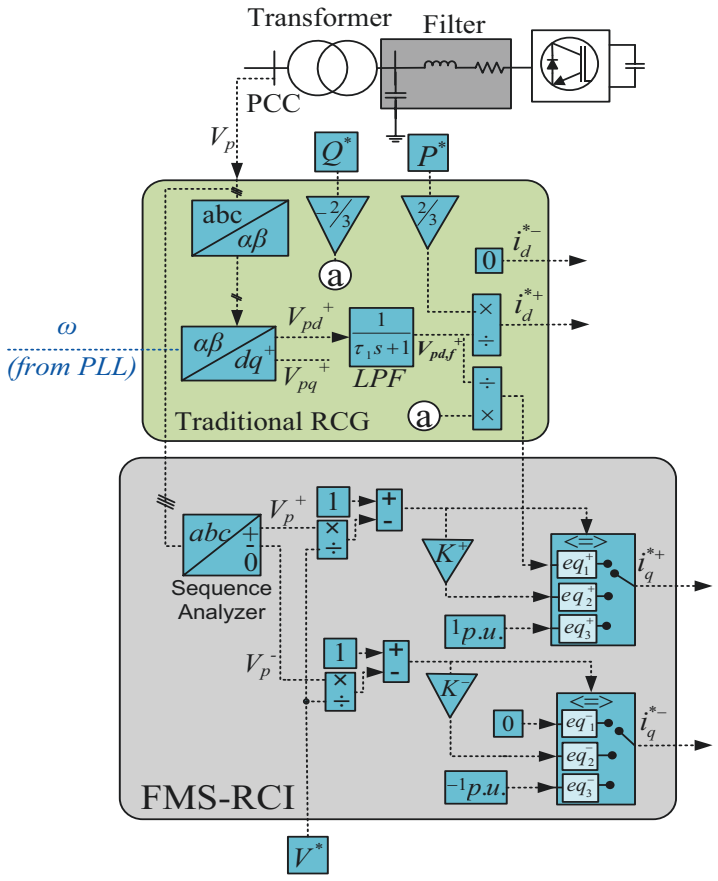

Figure 4.4 Reference current generation diagram.

To illustrate the effectiveness of using this filter, the time-domain simulation results are presented in Figure 4.5. In this test case, the RCG method is switched to the FMS-RCI at t=0.3 s. As shown in Figure 4.5(a), the generated reference current in the dq frame gets unstable after 50 ms when there is no LPF applied to the positive sequence voltage extraction on PCC. However, when the LPF is applied, the generated current is remained stable and steady. This effect is also visible in Figure 4.5(b) where the three-phase signal of the PCC voltage is demonstrated at the same test case. The importance and the effectiveness of the application of this LPF are also studied using the eigenvalue analysis, and the results are presented in Section 4.3.2.

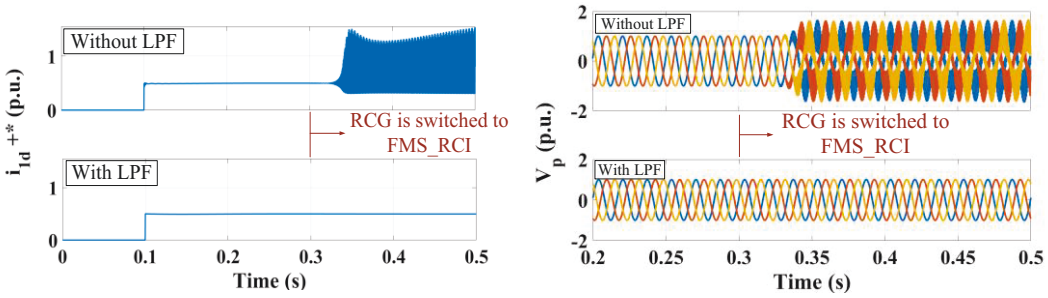

(a) (b)

Figure 4.5 Effect of using the low-pass filter in the implementation of the RCG block.

4.2 Multi-Stage Linearized Model

The dynamics of the grid-connected converter are highly nonlinear. Besides, according to (1.2), (4.1) and (4.2) and because there are many feedback loops through low-pass filters (in the implementation of the current controller and the PLL), they add more non-linearity to the system. To obtain a detailed small-signal stability analysis in this chapter, the complete CI-DG unit system in the DDSRF is linearized in three different stages: before, during and after the fault. This multi-stage state-space modeling is obtained based on the approach presented in 3.2.2.

During a fault, the converter loses its capability, partially or completely, to inject or absorb active power; so, a voltage violation may occur. To prevent any disconnection of the DG unit during the fault, switching the RCG method from (1.2) to (4.1) and (4.2) is proposed based on the grid codes. In this chapter, the performance of an LVRT-capable CI-DG unit system is analyzed analytically.

Obtaining the linearized models for a CI-DG unit is essential to analyze its dynamic performance during LVRT and to set-up different controllers. A CI-DG unit will be subjected to different operating conditions under the fault; hence, employing one linearized model does not seem reasonable. Therefore, three stages are adopted in this chapter for accurate modeling, while considering the LVRT requirements. The first stage represents the CI-DG unit system dynamics before the fault occurrence. In this stage, the model input consists of the measured grid bus voltage (V_g) and the value of the active and reactive power demands (P^* and Q^*,

respectively). Also, the employed RCG method is based on (1.2). The steady-state values for the first stage are obtained from the normal system operation.

The second stage characterizes the CI-DG unit system dynamics during the fault period, where the generated reference currents are dictated by new LVRT requirements, presented in (4.1) and (4.2). The model inputs in this stage are V_g, the active power demand and the reference PCC voltage value (V^*).

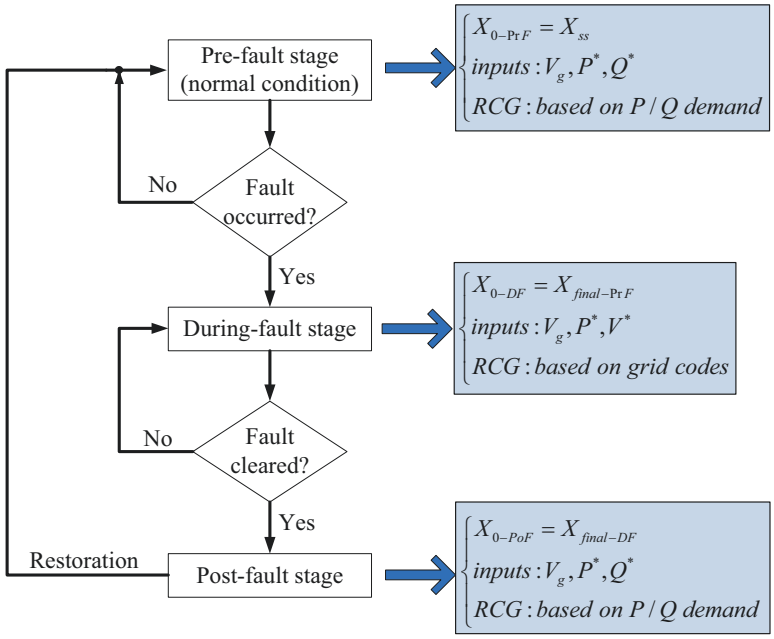

Figure 4.6 Diagram of the multi-stage modeling.

The third stage represents the CI-DG unit system dynamics after fault clearance. Current system dynamics, which is changed from its steady-state mode during the fault, tries to recapture the pre-fault condition. In this stage, the system is mainly reacting to its initial states instead of any external forces. This initial state is the final state obtained from the second stage, i.e., during-fault stage. The schematic diagram is illustrated in Figure 4.6. Subscripts "*0*" and "*final*" stand for the initial and final states, respectively; *SS* stands for the steady-state and, *PrF*, *DF* and *PoF* stand for the pre-fault, during-fault, and post-fault stages, respectively. Each stage and the related linearized models will be discussed in the following subsections.

In all stages, the generated reference current signals are fed into four proportional-integral (PI) regulators implemented in the DDSRF. This controlling

section is the same in all modeling stages; however, the method of generating the reference current values, the initial states, and the input matrices are different.

To obtain a detailed linearized model for the system with the consideration of all controllers, 23 state variables are defined as follows:

$$X_{23\times1} = [i_{gd}^{+}, i_{gq}^{+}, i_{gd}^{-}, i_{gq}^{-}, i_{1d}^{+}, i_{1q}^{+}, i_{1d}^{-}, i_{1q}^{-}, \int e_d^{+}dt, \int e_q^{+}dt, \int e_d^{-}dt, \int e_q^{-}dt, \omega, v_{pd}^{+}, v_{pq}^{+}, v_{pd}^{-}, v_{pq}^{-}, v_{fd}^{+}, v_{fq}^{+}, v_{fd}^{-}, v_{fq}^{-}, v_{pd,f}^{+}, v_{pq,f}^{+}]^T \tag{4.4}$$

where $\int e\,dt$ stands for the integral of the current signal error and $V^{+}_{p,f}$ stands for the output signal of the LPF which is used for sampling V_{pd}^{+} (see Figure 4.4). According to the number of state variables, there are 23 differential equations in the state-space model of the system. Therefore, to keep the equations more straightforward to follow, the mathematical method of equation (3.1) is again used in this chapter.

4.2.1 Pre-Fault Stage

The first stage characterizes the CI-DG unit dynamics before the fault occurrence. In this stage, the reference current signals are generated based on (1.2) to be fed into the four PI regulators implemented in the negative and positive sequences in the *dq* reference frames. In this stage, the model inputs include the active and reactive power demands required by the system operators (i.e., P^* and Q^*). The input matrix for the pre-fault stage is:

$$u = [v_{gd}^{+}, v_{gq}^{+}, v_{gd}^{-}, v_{gq}^{-}, P^*, Q^*] \tag{4.5}$$

In the pre-fault stage modeling, the origin is considered as the equilibrium point which is obtained in the normal operating condition of the CI-DG unit system. The final linearized forms of (1.2) can be easily obtained as follows:

$$\begin{aligned}
\Delta i_d^{*+} &= \frac{2}{3}\frac{1}{V^{+}_{pd,f,ss}}\Delta P^* + \frac{2}{3}P_{ss}^{\ *}\frac{-1}{(V^{+}_{pd,f,ss})^2}\Delta V^{+}_{pd,f}, \\
\Delta i_q^{*+} &= \frac{-2}{3}\frac{1}{V^{+}_{pd,f,ss}}\Delta Q^* + \frac{-2}{3}Q_0^{\ *}\frac{-1}{(V^{+}_{pd,f,ss})^2}\Delta V^{+}_{pd,f}, \\
\Delta i_d^{*-} &= 0, \Delta i_q^{*-} = 0
\end{aligned} \tag{4.6}$$

where the subscript *ss* stands for the steady-state values. The detailed linearized equations for the PLL and the current controller can be found in Sections 2.2.2 and 2.2.3. The comprehensive demonstration of the state and input matrices are provided in Appendix C. By defining any desired output in the system, the *C* and *D* matrices will also be obtained, and the final transfer function of the system will be expressed as:

$$H(s)=C(sI-A)^{-1}B+D \tag{4.7}$$

4.2.2 During-Fault Stage

The second stage considers the CI-DG unit dynamics during the fault period, where the reference current generation is dictated by the LVRT requirements. In this chapter, the FMS-RCI method will be used to meet the new grid codes requirements. The related equations are shown in (4.1) and (4.2). It can be seen that in each sequence of the reactive current reference generation, three different equilibrium points are considered based on the positive sequence voltage drop (in FPS-RCI) and the value of the negative sequence voltage (in FNS-RCI). These equilibrium points are shown in (4.1) and (4.2) by eq^{+}_{i} and eq^{-}_{i} in which *i* can be 1, 2 or 3.

In this case, the model input contains P^{*} and V^{*}. The input matrix for the during-fault stage is:

$$u=[v^{+}_{gd}, v^{+}_{gq}, v^{-}_{gd}, v^{-}_{gq}, P^{*}, V^{*}_{p}] \tag{4.8}$$

For the studied fault in this chapter, both sequences of the PCC voltage during the fault are placed in the intervals of $eq^{+}_{2,}$ and eq^{-}_{2} of (4.1) and (4.2) and the total value of the injected reactive current remained below 1 p.u. Therefore, the injection of the active current is made based on equation (1.2) and its linearized form would be the same as presented in (4.6) for Δi^{*+}_{d} and Δi^{*-}_{d}. The reference current values in *q* frame are calculated based on (4.1) and (4.2) to implement the FMS-RCI method for LVRT performance. Therefore, the linearized equations for eq^{+}_{2} and eq^{-}_{2}, which are the most complicated equilibrium points, are presented here:

$$\Delta i_q^{*+} = K^+(\Delta \mathrm{V}^* - \Delta\sqrt{{v_{pd}^+}^2 + {v_{pq}^+}^2}) = K^+(\Delta \mathrm{V}^* - m_{11}\Delta v_{pd}^+ - \mathrm{m}_{21}\,\Delta v_{pq}^+) \tag{4.9}$$

$$\Delta i_q^{*-} = -K^-(\Delta\sqrt{{v_{pd}^-}^2 + {v_{pq}^-}^2}) = K^-(-m_{31}\Delta v_{pd}^- - m_{41}\Delta v_{pq}^-) \tag{4.10}$$

In which:

$$m_{11} = \frac{v_{pd,ss}^+}{\sqrt{{v_{pd,ss}^+}^2 + {v_{pq,ss}^+}^2}}, \quad \mathrm{m}_{21} = \frac{v_{pq,ss}^+}{\sqrt{{v_{pd,ss}^+}^2 + {v_{pq,ss}^+}^2}} \tag{4.11}$$

$$m_{31} = \frac{v_{pd,ss}^-}{\sqrt{{v_{pd,ss}^+}^2 + {v_{pq,ss}^+}^2}}, \quad m_{41} = \frac{v_{pq,ss}^-}{\sqrt{{v_{pd,ss}^+}^2 + {v_{pq,ss}^+}^2}} \tag{4.12}$$

Based on these equations, A_1, A_2 and B_1 matrices are obtained in Appendix C to provide the final complete linear model of the during-fault stage, based on (3.1). Model initialization is made using the steady-state values of system parameters during the fault. Based on the grid code standards of Section 4.2, system performance during the first 150 ms from the fault occurrence is the primary concern in the LVRT studies [19]. Therefore, the steady-state values for this stage are obtained from the final states of this 150 ms period.

4.2.3 Post-fault Stage

This stage characterizes the CI-DG unit dynamics after the fault clearance when the system is trying to retrieve its normal condition which is the initial pre-fault operating point. Therefore, equations (1.2) are again valid to represent the RCG method, and the same linear model as the pre-fault can be used in this stage. However, the origin is not the equilibrium point anymore. Instead, the corresponding initial point can be extracted from the final states of the during-fault stage.

The main focus of this chapter is on the during- and post-fault stages; because these models make it possible to study the dynamics of the FMS-RCI method considering the LVRT requirements. In fact, the effect of the flexible selection of K^+, K^- and other controlling parameters on system stability performance during and after a fault can be thoroughly studied in this model with the consideration of different grid strengths and unbalanced fault characteristics.

4.2.4 Model Verification

To verify the effectiveness of the obtained linear model, the time-domain response of the state-space model is compared to the time-domain response of the detailed nonlinear model simulated in MATLAB-SIMULINK. The model validation results show an accurate agreement between both models responses. A sample case is shown in Figure 4.7. In this test, the system is operating in the pre-fault situation, and the DG active power reference drops by 10% at t=0.7s. Figure 4.7 shows a comparison of the positive *d*- and *q*-axis PCC voltage in the linear and nonlinear models. Both figures show the accuracy of the obtained state-space model as the two traces are nearly identical.

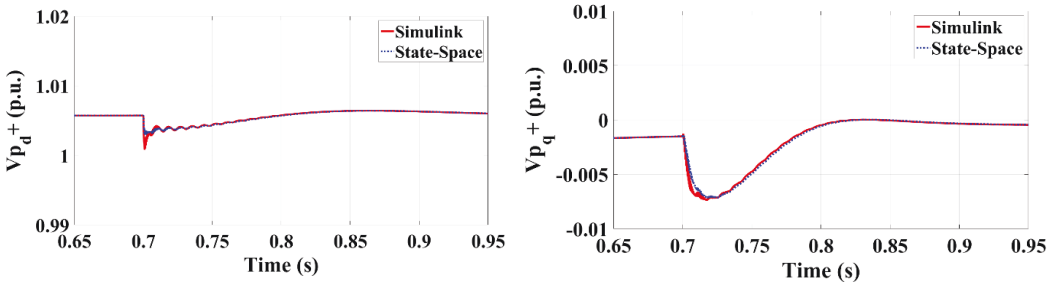

Figure 4.7 State-space model validation for (a) the positive *d*-axis and, (b) the positive *q*-axis PCC voltage when the reference active power drops by 10%.

4.3 Stability Analysis considering RPNSI-LVRT Requirements

To implement the FMS-RCI, the diagrams of Figure 4.3 and Figure 4.4 are used in this chapter. The initial design of the PI compensators in the current controller and the PLL is based on the gain-shaping method presented in [24]. Besides, reference [40] suggests selecting the typical value of 2.5 for both K^+ and K^- while the system is in eq_2^+ and eq_2^-, respectively. This value determines the ratio of the reactive current injection in both positive and negative sequences with respect to the positive sequence voltage dip and negative sequence voltage value.

4.3.1 FMS-RCI Performance in LVRT

One of the missing studies in the literature is a thorough analysis of the effect of the grid strength on the stability performance of the CI-DG unit while employing the FMS-RCI. The nature of CI-DG system interactions with the power system and their associated problems are highly dependent on the strength of the ac system. To show the effectiveness of the FMS-RCI method in comparison to the traditional RCG method of (1.2), the system performance is monitored under an unbalanced fault when the system is connected to a strong grid with SCR=5.5. In this test case, the detailed nonlinear model of the CI-DG unit of Figure 4.1 is implemented in MATLAB/SIMULINK, and a two-phase to ground fault at t=0.6 s occurred on bus2 and lasted for 200 ms. The CI-DG unit with the FMS-RCI remains stable during and after the fault, as shown in Figure 4.8(a). The positive and negative components of the PCC voltage for the traditional and FMS-RCI methods are shown in Figure 4.8(b).

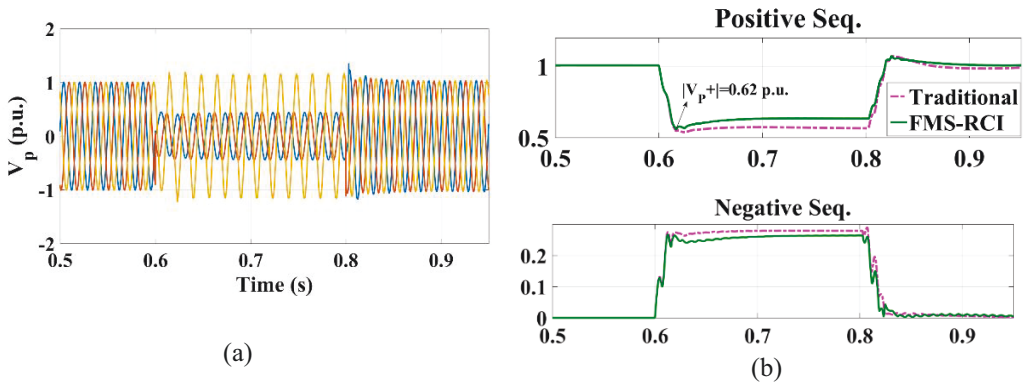

Figure 4.8 (a) PCC voltage showing the LVRT performance of the CI-DG unit when employing FMS-RCI; (b) PCC Voltage components for the traditional RCG and the FMS-RCI method.

4.3.2 Low-Pass Filter Design for the Positive-Sequence Voltage Extraction

As mentioned in Section 4.2, to improve the stability performance of the system, an LPF is used on the positive sequence extraction of the PCC voltage in the RCG block, presented in Figure 4.4. To illustrate the effectiveness of this method, the most dominant poles of the system before and after applying the LPF are shown in Figure 4.9, where the time constant of the filter, τ_1, is set to be three times τ_i (see

Eq. (4.3)) which is 3 ms. The system is connected to a strong grid (SCR=5.5), and all controlling parameters are designed basically. The value of both K^+ and K^- are set to 2.5. Figure 4.9 illustrates that the application of this LPF is necessary to employ the FMS-RCI method because there are four unstable poles in the pre-fault linear model of the system when there is no LPF applied on the positive sequence voltage extraction on the PCC. These eigenvalue analysis results confirmed the time-domain simulation results of Figure 4.5 where the system represented instability even for the pre-fault model.

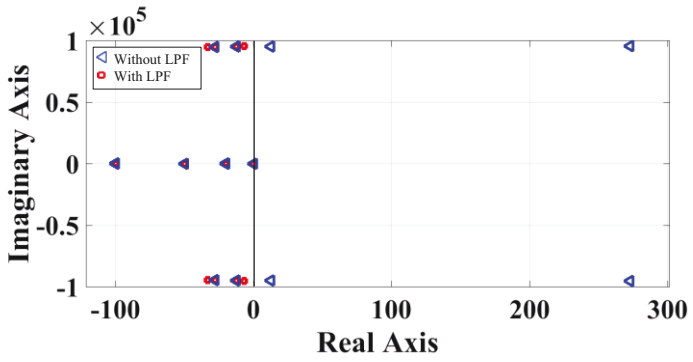

Figure 4.9 The dominant poles of the system, before and after applying the low-pass filter to V_{pd}^{+}, when the grid is strong.

Figure 4.10 shows the eigenvalue locus when τ_I changes from $1\times\tau_i$ to $20\times\tau_i$ for connection of the DG unit to a strong grid (SCR= 5.5). The linear model represents the complete CI-DG unit with all different controllers; therefore, the eigenvalue analysis includes all interactions among system and control loops. The results show that the design of this LPF does not affect the most dominant oscillatory poles remarkably. But, for τ_I>10 it moves one of the real poles towards the origin which is not desirable. Therefore, for this CI-DG unit selecting τ_I=10 seems reasonable.

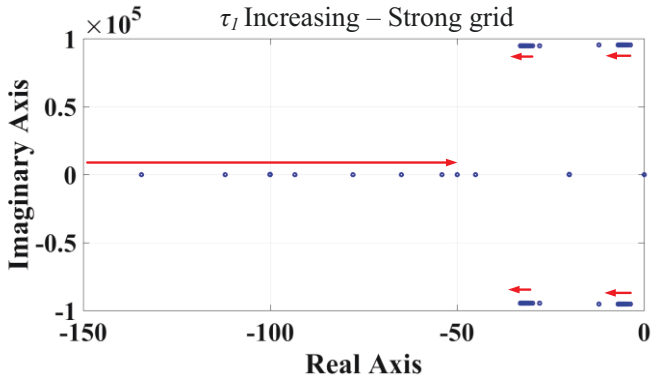

Figure 4.10 Eigenvalue locus of the effect of changing the value of τ_I from $1\times\tau_i$ to $20\times\tau_i$ for connection of the DG unit to a strong grid.

4.4 LVRT Performance Improvement in Weak Grid Condition

To illustrate the importance of the study of weak grid condition, the same CI-DG unit is connected to a weak grid with SCR=1.5 and, the same fault scenario of Section 4.3.1 is studied.

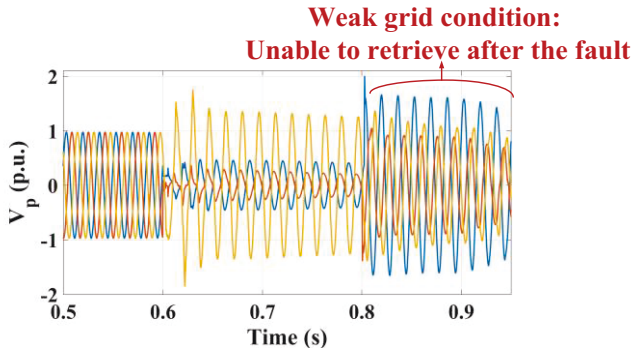

Figure 4.11 CI-DG unit performance employing FMS-RCI with the basic control parameters design when the connected grid is weak.

Figure 4.11 presents the LVRT performance of the CI-DG unit employing the FMS-RCI method with both K^+ and K^- set on 2.5. Compared to Figure 4.8(a), the system is highly unbalanced during the fault, and it is unable to retrieve its balance operation even after the fault is cleared. Therefore, a detailed study seems to be necessary with the consideration of the grid strength on the performance of the FMS-RCI employing DG units.

4.4.1 Re-Designing FMS-RCI Parameters Using Model-Based Design Method

The obtained detailed multi-stage linear model of the CI-DG system provides the possibility of studying the dynamic behavior of the during- and post-fault stages, separately, while respecting the newly imposed grid codes of the LVRT requirements under an unbalanced fault condition. Also, because the complete linear model of the system considers all of the system controllers (e.g., a current controller, PLL, FMS-RCI reference current generators, feed-forward filters, etc.) in details, the interactions among them are effectively considered in all small-signal stability analyses which will be presented in the following sections.

As the first step, the complete system poles are obtained in the post-fault stage for the cases of connection to a strong and weak grid. The results are shown in Figure 4.12. It is observed that the system poles in connection to a weak grid are remarkably placed closer to the imaginary axis which represents lower damping in system performance in the case of disturbances.

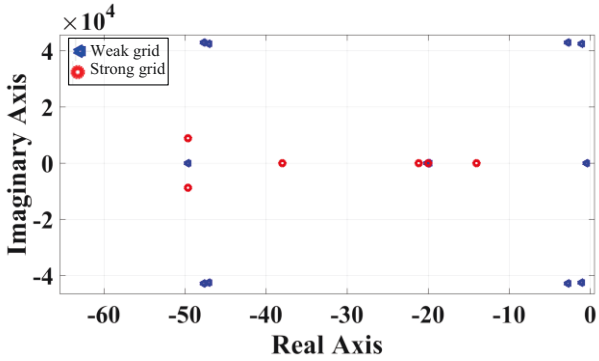

Figure 4.12 CI-DG system poles in connection to the strong and weak grid while employing FMS-RCI.

To start with the model-based design method, first, the effect of changing the FMS-RCI parameters on the stability of the CI-DG unit in connection to a weak grid is studied. Figure 4.13 demonstrates that there are two dominant pole-pairs connected to each FMS-RCI parameter, i.e., K^+ or K^- when their value is decreased; one pair moves away from the imaginary axis towards left while the other pair moves towards the imaginary axis. Therefore, the results reveal that the suggested constant values for K^+ and K^- in [40] are not the most accurate ones considering the

stability performance of the system during unbalanced grid condition. Especially, when the connected grid is not strong enough, the selection of these control coefficients should be made more carefully. In Figure 4.13(c), the value of K^+ and K^- are changed simultaneously from 2.5 to 1. In this range, all poles are finally placed far enough from the imaginary axis which represents a more stable and damped system compared to when the K^+ and K^- are set to 2.5.

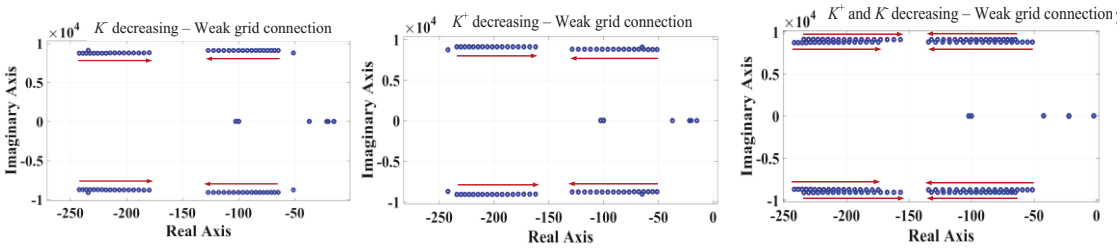

Figure 4.13 Eigenvalue locus showing the effect of changing the FMS-RCI parameters.

One important point about these findings is that they show how changing the values of K^+ and K^- affect the transient stability of the system while all other system dynamics are taken into account. Therefore, the initial design of the FMS-RCI parameters can be modified based on this eigenvalue analysis results to guarantee a stable performance of the CI-DG unit in connection to a weak grid. As mentioned before, the initial design of all controller compensators is done basically based on satisfying a stable phase and gain margin using the Bode plot. Besides, because the FMS-RCI parameters are effective when the system is in eq_2^+ or eq_2^-, the above-presented eigenvalue locus is obtained using the during-fault stage model. The results for the post-fault stage are also obtained which revealed similar trends. Hence, only the results of the during-fault model are shown in this step. Therefore, this method suggests a higher stability margin for the case of a DG unit connected to a weak grid.

The other remarkable point about this model-based compensator design method is that, although the results are obtained using the small-signal stability analysis, they are applicable in the large-signal stability analysis of the same system. To verify this statement, the obtained new values for K^+ and K^- (i.e., K^+ and

K^- set to 1) are used in the same detailed nonlinear model of the system when the connected grid is weak with SCR=1.5. The result is shown in Figure 4.14. Comparing this with Figure 4.11 reveals that by decreasing the value of FMS-RCI parameters, the large-signal stability of the system is also improved. As shown, the system could retrieve its stable and balanced operation after fault clearance which yields reliable system operation. The system is returned to the pre-fault steady-state after about 200 ms of the fault clearance. These results demonstrate that the proposed model-based method is able to improve the overall LVRT performance of the system when the conned grid is not strong enough.

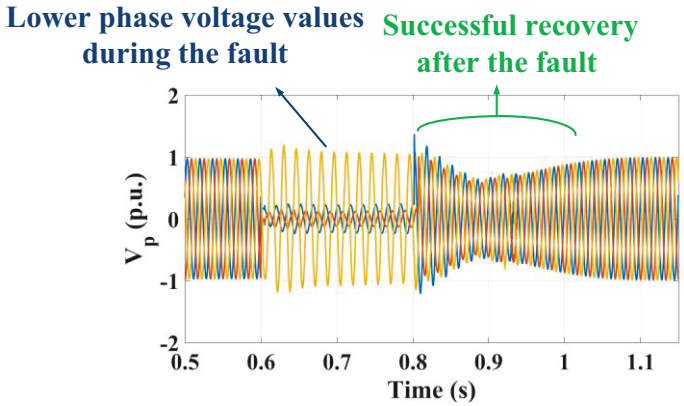

Figure 4.14 CI-DG unit performance employing FMS-RCI with $K^+ = K^- = 1$ when the connected grid is weak.

To study more details on the stability improvement in the system after fault clearance, the eigenvalues for the post-fault model are obtained for two different operating points: first, with the initial values of $K^+ = K^- = 2.5$ and second, with the suggested FMS-RCI parameters obtained in the small-signal stability analysis, as shown in Figure 4.15. There are two pairs of dominant poles, encircled in Figure 4.15, which moved towards left, representing higher damping in the post-fault stage. This result verifies what is observed in Figure 4.14 from the time-domain simulation study.

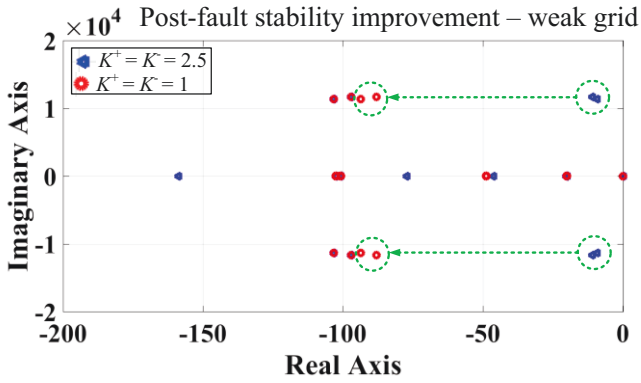

Figure 4.15 The dominant poles of the post-fault system model showing the effect of improved FMS-RCI parameters.

Calculating the damping ratio of the mentioned pole pairs based on the equation of (2.26) shows that selecting the proposed FMS-RCI parameters can considerably increase the damping ratio of these dominant modes which results in an improved transient response of the system. TABLE 4.2 shows the damping ratio values before and after using the proposed FMS-RCI parameters in this model.

TABLE 4.2 Damping ratio improvement in the dominant poles of the post-fault model

Pole pair 1	ξ_{old}=9.16e-4	ξ_{new}=74e-4	$\xi_{new}/\ \xi_{old}$ =8.08
Pole pair 2	ξ_{old}=7.98e-4	ξ_{new}=82e-4	$\xi_{new}/\ \xi_{old}$ =10.27

These results represent a significant improvement in satisfying the LVRT requirements while employing the FMS-RCI in a CI-DG unit connected to a weak grid. Due to the direct interconnection with power grids, CI-DG units are particularly sensitive to non-ideal grid conditions, e.g., grid impedance, background harmonics, and grid voltage sags or swells, which often occur in weak grids. Hence, the stability and power quality of the GCC will be significantly influenced. This could become worse as the penetration level becomes higher increasingly, which is common in the recent power grids. However, this study showed that reconfiguring the FMS-RCI controlling parameters provides a higher range of certainty for the system when encounters a grid fault to satisfy the new grid code requirements, during and after the fault.

The value of the SCR is inversely related to the ac network impedance at the fundamental frequency (Z_s). Therefore, since $\Delta V_p^+ \propto i_q^+ Z_s$, higher Z_s which means

lower SCR should be followed by lower i_q^+ to keep the PCC voltage balanced on 1 p.u.; which represents lower K^+. The same discussion applies to the negative sequence reactive current injection. This fact confirms the obtained results of this chapter.

Figure 4.16 illustrates the modified diagrams of Figure 4.3 based on the small-signal analysis and the time-domain simulation results obtained in this section. As presented, for connection to a weaker grid, lower FMS-RCI parameters can satisfy the LVRT requirements of the grid code and at the same time, keep the system stable during and after the fault.

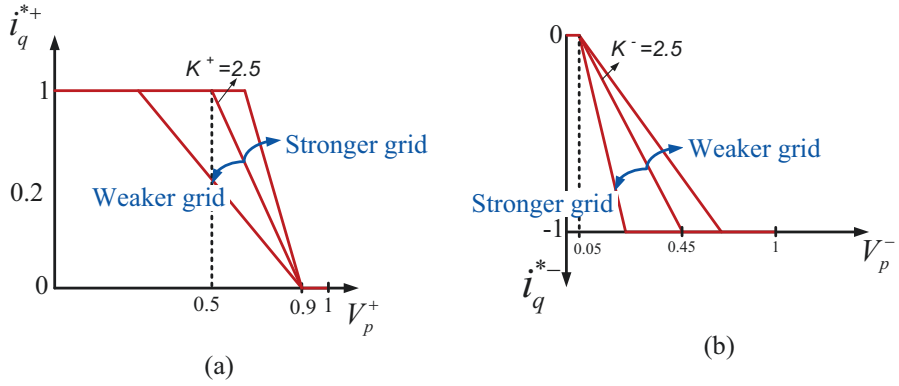

Figure 4.16 Modified selection of the FMS-RCI parameters based on the grid strength.

Besides, as demonstrated in Figure 4.2(a), for any voltage drop lower than 45% to zero which may last for 150 ms, the grid code requires the DG unit to stay connected and return to the normal condition up to 1500 ms after the fault. All of these constraints are considered and satisfied in the studied cases of this chapter.

As an overall summary, it is demonstrated that changing the values of K^+ and K^- affects the transient stability of the whole system. The results show that in the case of a weak grid condition, reducing the K^+ and K^- values guarantees a stable performance of the CI-DG unit under a grid fault. Besides, the proposed model-based compensator design method can also improve the large-signal stability of the system and enhance its post-fault stability performance.

4.4.2 Re-Designing Other Compensators with the Initial FMS-RCI Parameters Using Model-Based Design Method

Although selecting lower K^+ and K^- values could improve the small and large signal stability performance of the CI-DG unit under an unbalanced fault condition, it represents a lower injection of the positive and negative reactive current components to the system during the fault. Hence, the voltage support characteristic of the FMS-RCI strategy will not be as effective as before.

To keep the values of K^+ and K^- higher but still have a stable and balanced LVRT operation, another study is carried out to investigate the effect of other compensators parameters on the stability of the complete CI-DG unit system in weak grid condition. In this study, the eigenvalue analysis is employed again to investigate the effect of changing the proportional and integral gains (i.e., K_p and K_i, respectively) of the PLL and the current controller compensators. The initial design of these compensators is obtained based on the methods presented in [24]. For the PLL, the second-harmonic rejection along with an acceptable bandwidth and damping ratio are considered. For the current controller, the PI gains are designed to provide a DC reference tracking in *dq* frame by considering the pole-zero cancellation in the open-loop transfer function.

To employ the model-based parameters design for each compensator, its PI gains are changed, and the related eigenvalue locus is obtained. In the first step, the effect of changing the PLL control parameters is studied while the system is connected to a weak grid (SCR=1.5) and $K^+=K^-=2.5$. The results for the during-fault model are shown in Figure 4.17. It is observed that changing the PLL compensator gains from their initial design aggravates the stability criteria (Figure 4.17 (a)) or does not change it remarkably (Figure 4.17(b)). Therefore, since changing the PLL gains shows no improving effect on the small-signal stability of the system, in the next studies, the value of the PLL control parameters are kept on their initially designed values.

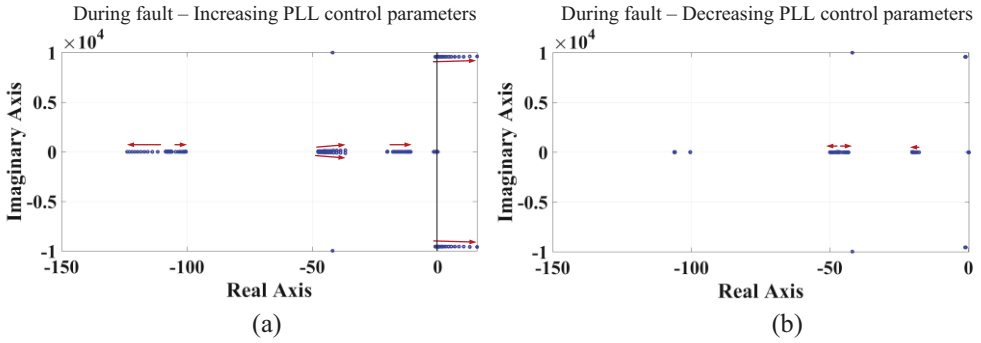

Figure 4.17 Eigenvalue locus showing the effect of changing the PLL controller PI gains with the initial FMS-RCI parameters when (a) increasing and, (b) decreasing the PLL gains.

In the next step, the PI gains of the current controller are changed in both during- and post-fault stages of the linear models. The eigenvalue locus is shown in Figure 4.18. As illustrated, by decreasing the integrator gain of the current controller, K_i, to 10% of its initial value, while the proportional gain, K_p, is kept constant, the most dominant poles in both stages move away from the imaginary axis towards left. It represents a higher damping ratio related to these modes and so, higher relative stability in the system. Changing K_p individually or at the same time with K_i, made some of the most dominant poles move towards the right; therefore, this value is kept unchanged. These results revealed that by reducing the value of K_i in the current controller from its initially designed value and keeping the FMS-RCI parameters high at 2, the relative stability of the CI-DG unit in connection to a weak grid is improved for both during- and after-fault stages.

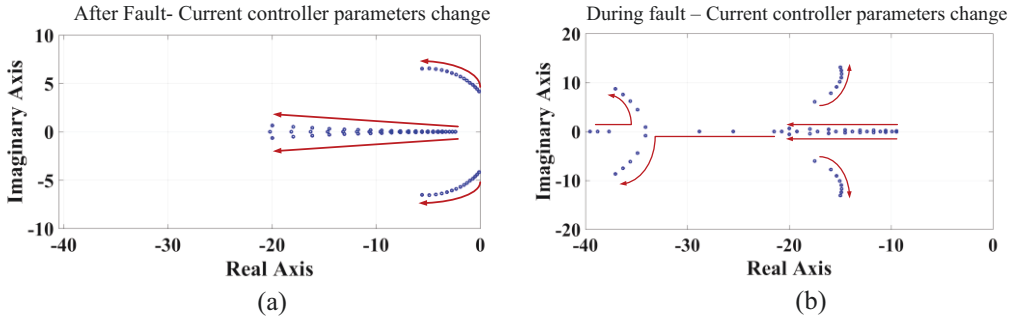

Figure 4.18 Eigenvalue locus showing the effect of changing the current controller PI gains with the initial FMS-RCI parameters in (a) post-fault stage and, (b) during-fault stage.

To verify the results above, the previous scenario is carried out in the detailed nonlinear model of the system. The DG unit is connected to a weak grid of SCR=1.5, and the same unbalanced fault occurs on bus2. K^+ and K^- are set to 2, the

current controller K_i is reduced by 10%. Figure 4.19 shows the results of the PCC voltage LVRT performance. Compared to Figure 4.11, it reveals that the transient stability characteristic of the system is improved and it could retrieve to the balanced and stable operation in less than 100 ms while the injection of the reactive current components is kept high during the fault. This fact is also evident by comparing Figure 4.19 and Figure 4.14 for the phase voltage values during the fault.

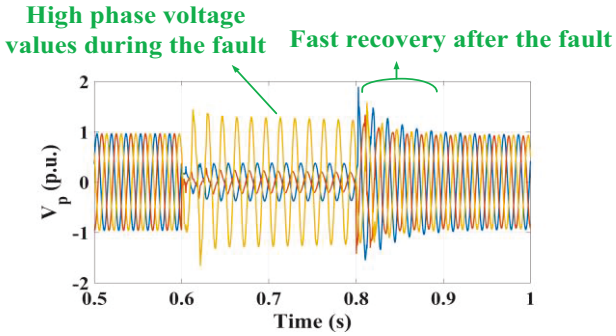

Figure 4.19 CI-DG unit performance employing FMS-RCI with $K^+ = K^- = 2$ and current controller K_i reduced by 10% when the connected grid is weak.

The results of this section are another verification of the capability of the proposed model-based design to be valid for both small-signal and transient stability improvement of the system considering LVRT requirements. The main advantage of the proposed method of this section is that by choosing higher FMS-RCI parameters and reducing the current controller PI parameters, the PCC voltage receives higher support during the unbalanced fault and, at the same time, the system satisfies the LVRT requirements and rides through the fault. It is worth mentioning again that, because the linearized models in all three stages are obtained considering all controllers and filters, the results of the eigenvalue analyses in all studies of this chapter include the interactions among all of these units. Therefore, unlike the conventional individual controllers design approach, the proposed augmented model-based design approach accounts for the interactions among different controllers, grid dynamics, and parameters, and optimizes the dynamic performance of the whole grid-connected converter system.

4.5 Multi-DG System

To study the application of the findings of the previous sections to different systems, a more complicated medium-voltage distribution system including some local loads and two CI-DG units, shown in Figure 3.1(a), is employed and used for nonlinear time-domain simulation studies. The loads are represented by parallel *R*–*L* elements. Both DG units are equipped with the FMS-RCI method to support the LVRT requirements.

To study the performance of this multi-DG system while employing the FMS-RCI method, two scenarios are considered in this chapter: (1) one-DG system expansion; (2) two-DG system planning. Each scenario is thoroughly studied in the next subsection.

4.5.1 Scenario 1: One-DG System Expansion

In the first scenario, an existing system with one CI-DG unit is supposed to be extended to the two-DG system of Figure 3.1(a). In this case, the rating of the first DG is already determined. As a case study, the second DG is selected to be with the same rating as the first DG, and the total connected load is 1.0 p.u. As a reasonable supposition, the line impedance between the DGs is around 20% of the grid impedance. Therefore, bus3 can still be considered as the PCC for both DGs, and so, the initial grid strength or the SCR of this system will be almost half of what it initially was in the one-DG unit system of Figure 4.1, i.e., SCR≈3. By referring to the results of Section 4.4.1, it seems reasonable to select the initial values of K^+ and K^- lower than 2.5 for both DGs in this scenario. Hence, during the unbalanced condition, each DG will support the PCC by injecting its ratio of the positive and negative reactive current components. This hypothesis is proved and shown in Figure 4.20 where changing K^+ and K^- values from 2.5 (Figure 4.20(a)) to 1 (Figure 4.20(b)) could improve the system performance during and after the fault, whereas the other controllers parameters are kept intact. In Figure 4.20(a), the settling time is almost 400 ms, and the maximum phase current during the fault is high which may activate the protection relays. For space saving, only the signals of DG2 are

shown in Figure 4.20; because the signals of DG1 also represent the similar characteristics.

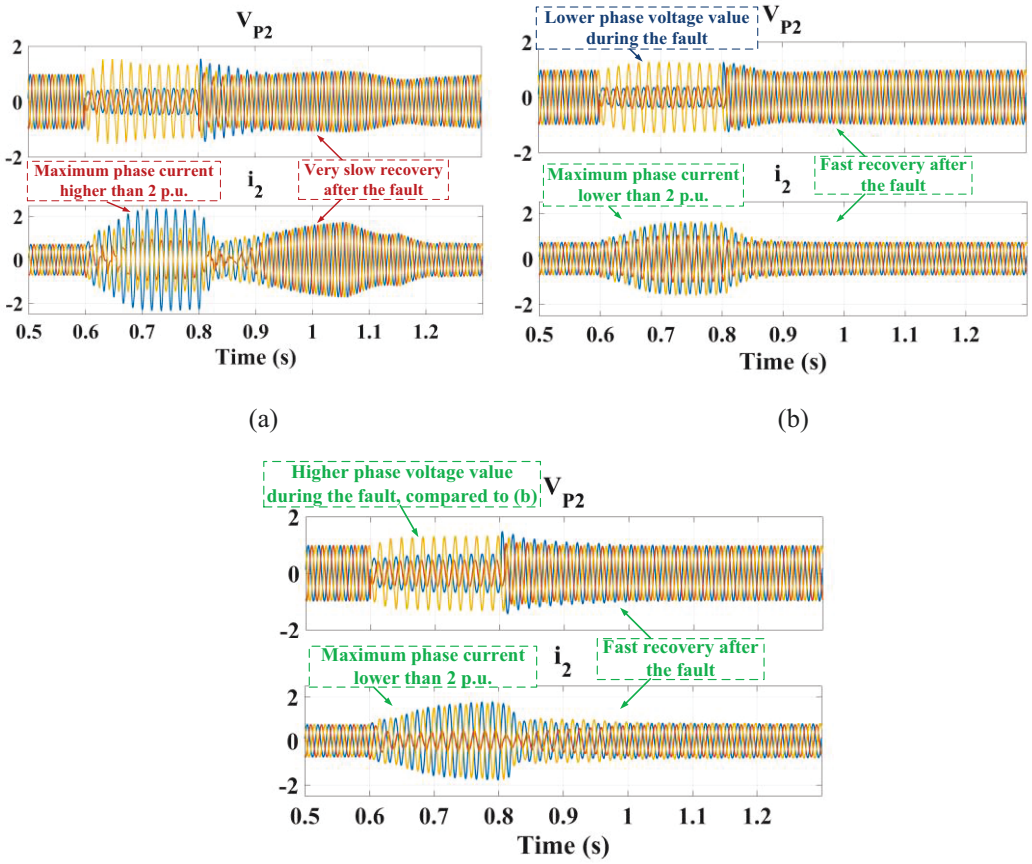

Figure 4.20 The effect of selecting improved controlling parameters in scenario #1 of two-DG system when connected to a weak grid: (a) with $K^+ = K^- = 2.5$ and initial compensators design; (b) with $K^+ = K^- = 1$ and initial compensators design; (c) with $K^+ = K^- = 2$ and current controllers K_i parameter reduced by 10%.

To show the effectiveness of the proposed method of Section 4.4.2, in the next test, the $K^{+,}$ and K^- values are set higher (to 2), but the value of the integrator gain of the current controller of both DGs is reduced to 10% of its initial value. The results are presented in Figure 4.20(c) where the performance improvement is clear compared to Figure 4.20(a).

4.5.2 Scenario 2: Two-DG System Planning

In the second scenario, a two-DG system should be designed, and the proper rating for both DGs can be defined. By having the same grid with the initially known short-circuit characteristic, an economical selection for the DG units with the same

1.0 p.u. load, is to have each DG unit with the rating as half of what it was in the first scenario, i.e., 2.5 MVA. Therefore, the grid strength will initially be high with SCR=5. In this case, with both DGs equipped with the FMS-RCI method, the initial selection of $K^+ = K^- = 2.5$ represents an acceptable LVRT performance for the two-DG system. However, when the connected grid is weak with SCR=2, both DGs will be unable to retrieve their balanced and stable operation after being subjected to the unbalanced fault. This event can be seen in Figure 4.21(a). As a remedy, the proposed methodology of Section 4.4.2 is applied to the system controllers. The results of Figure 4.21(b) illustrate the effectiveness of this method in improving the large signal stability of the tow-DG system in connection to the weak grid.

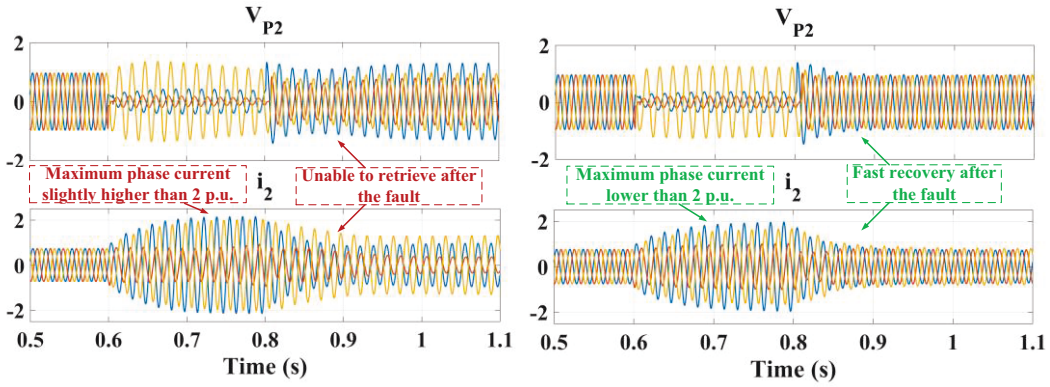

Figure 4.21 The effect of selecting improved controlling parameters in scenario #2 of the two-DG system when connected to a weak grid: (a) with $K^+ = K^- = 2.5$ and initial compensators design; (b) with $K^+ = K^- = 2$ and current controllers K_i parameter reduced by 10%.

4.6 Experimental Results

The results of the time-domain and the state-space stability analyses are also validated using a scaled-down 1.0 kVA laboratory prototype as shown in Figure 4.22. The key components for the laboratory setup are the same as already explained in Section 2.5. For the strong grid condition, the SCR is considered 6.6, and for the weak grid condition, the SCR is set to be 2.1. To study the effectiveness of the proposed methods in Sections 4.4.1 and 4.4.2, three fault scenarios are studied in the following subsections:

- Fault Scenario 1: the DG unit is connected to a strong grid with SCR=6.6, and it encountered a short-term unbalanced one-phase to ground fault.
- Fault Scenario 2: the DG unit is connected to a weak grid with SCR=2.1, and it encountered a short-term unbalanced one-phase to ground fault.
- Fault Scenario 3: the DG unit is connected to a weak grid with SCR=2.1, and it encountered a short-term unbalanced two-phase to ground fault.

Figure 4.22 A view of the experimental test setup.

4.6.2 Fault Scenario 1

In this test case, the DG unit is connected to the strong grid and the FMS-RCI is adopted with $K^+=K^-=2.5$. Figure 4.23(a) and (b) show the three-phase PCC voltage when the system is encountered an unbalanced one-phase to ground fault on the line between the DG unit and the grid. As shown in Figure 4.23(c), the DG unit could ride through the fault and remain connected to the grid which represents a successful LVRT based on the grid code requirements. The PCC voltage components are shown in Figure 4.23(e) illustrating that in this fault scenario the injection of the reactive current components will be obtained based on eq_2^+ and eq_2^- of (4.1) and (4.2). According to Figure 4.23(c), the value of the DG unit current stayed below the defined thermal limit (i.e., 1.0 p.u.) during the fault which means the injection of the active current can be obtained based on (1.2) during this time.

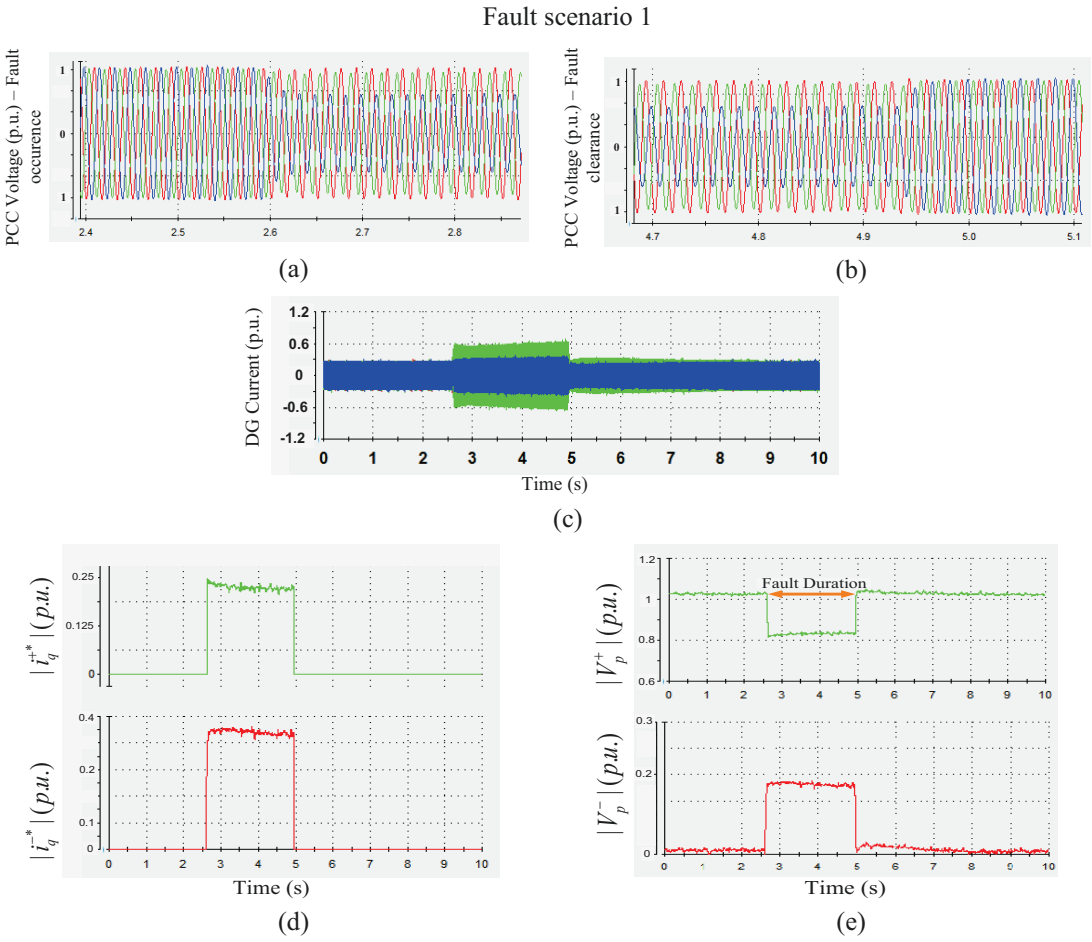

Figure 4.23 Experimental results for the fault scenario 1 when K^+=K^-=2.5: a) PCC three-phase voltage on fault occurrence; b) PCC three-phase voltage on fault clearance; c) DG current (i_1); d) injected reactive reference current values; e) PCC voltage in positive/negative *dq* frames.

4.6.3 Fault Scenario 2

In this test case, the CI-DG unit is connected to the weak grid with SCR=2.1, and the system is encountered an unbalanced one-phase to ground fault on the line between the DG unit and the grid. The effectiveness of the proposed model-based methods of Sections 4.4.1 and 4.4.2 are studied in three subsections as follows.

4.6.3.1 FMS-RCI Gains Effect

In the first step, the FMS-RCI parameters are set on K^+ =K^-=2.5. Figure 4.24(a) shows that the value of the converter current has remained below the thermal limit (i.e., 1.0 p.u.) during the fault which allows the injection of the reactive current components based on eq_2^+ and eq_2^- of (4.1) and (4.2), and injection of the active

current based on (1.2). However, after the fault clearance, the converter cannot retrieve to its previous stable operation, and the value of its current exceeds the determined thermal limit which causes the disconnection of the DG unit and failure of the LVRT.

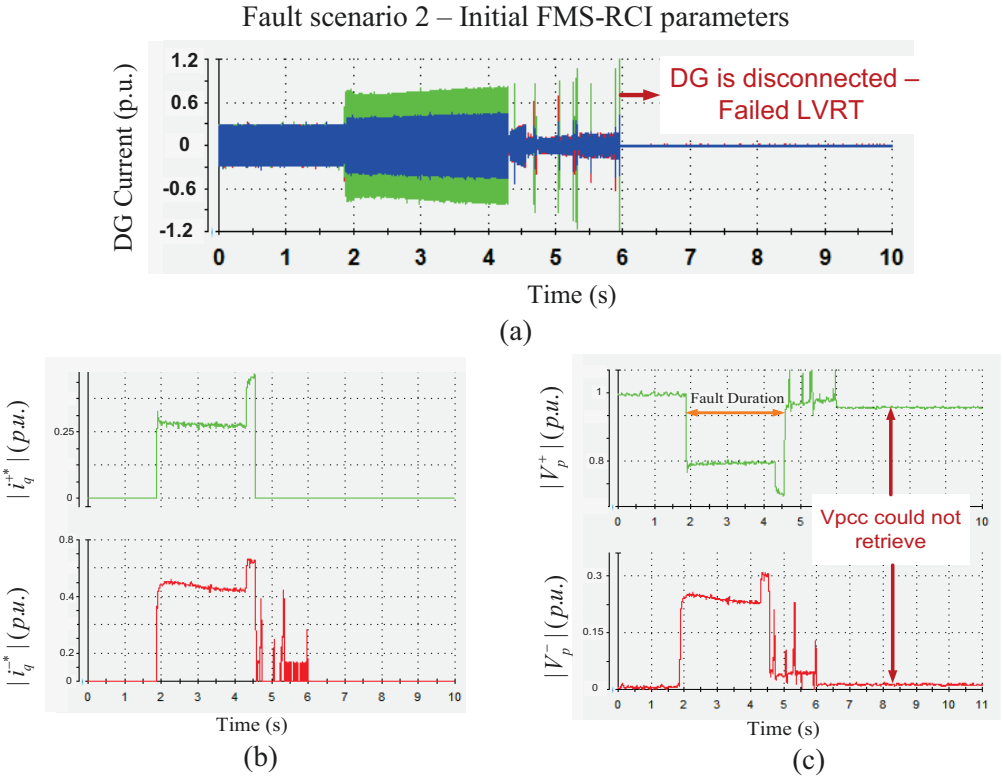

Figure 4.24 Experimental results for the fault scenario 2 when K^+=K^-=2.5: a) DG current (i_1); b) injected reactive reference current values; c) PCC voltage in positive/negative *dq* frames.

Therefore, to prevent the DG unit disconnection and based on the results of Section 4.4.1, the values of K^+ and K^- are reduced to 1, and the same fault scenario of Figure 4.24 is studied. As demonstrated in Figure 4.25, the system represented a successful LVRT performance and could successfully retrieve stable operation after the unbalance fault. These results verify the findings of Figure 4.13 andFigure 4.14. Considering the value of the converter current, shown in Figure 4.25(a), the determined thermal limit of the DG unit is respected during the fault, and the DG unit remained connected to the grid which represents a successful LVRT.

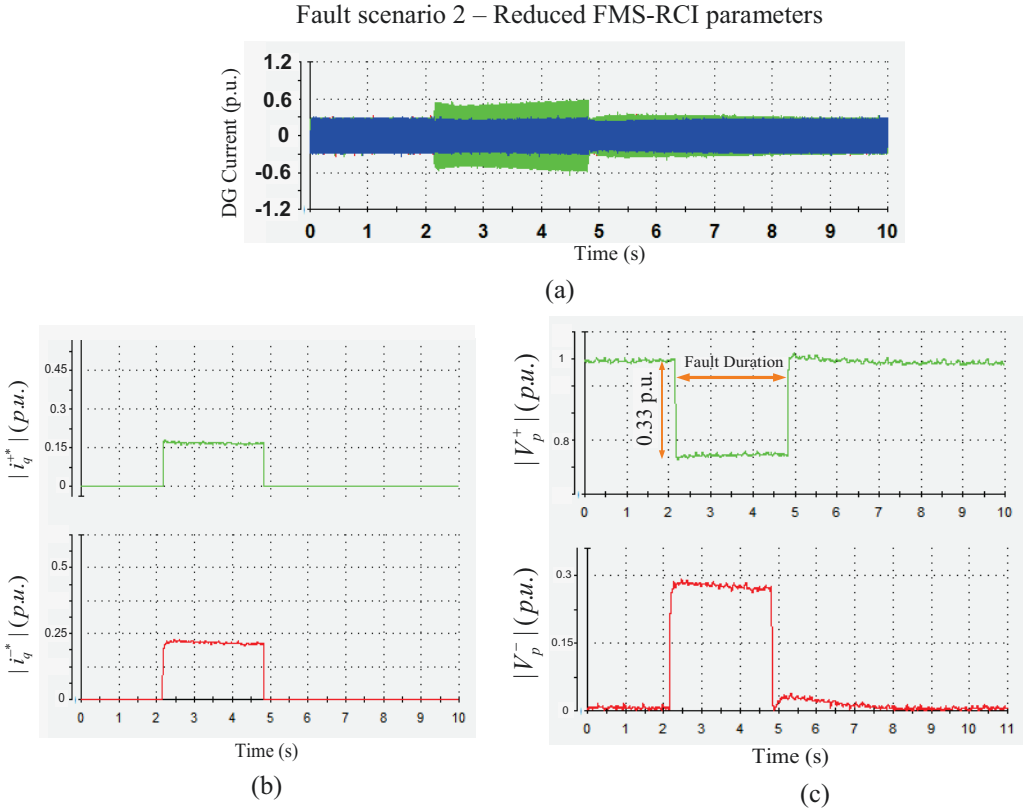

Figure 4.25 Experimental results for the fault scenario 2 when K^+=K^-=1: a) DG current (i_1); b) injected reference current values; c) PCC voltage in positive/negative *dq* frames.

4.6.3.2 PLL Gains Effect

To investigate the results of Section 4.4.2, first, the effect of changing the PLL gains in the experimental test setup is studied while setting the FMS-RCI gains back to their original values (i.e., K^+=K^-=2.5). The initial designed value for K_{p_PLL} is 5 and K_{i_PLL} is assumed to be 5× K_{p_PLL} [41]. In the first test, the value of K_{p_PLL} is increased, and the same fault scenario is studied. Figure 4.26 shows the result for the case of K_{p_PLL}=80. The next test case is performed when the K_{p_PLL} is reduced to 0.25 under the same fault condition. The results are presented in Figure 4.27. Both cases demonstrate the failure of the DG unit in satisfying the LVRT requirements which verify the eigenvalue analysis results of Figure 4.17.

Fault scenario 2 – Increased PLL gains

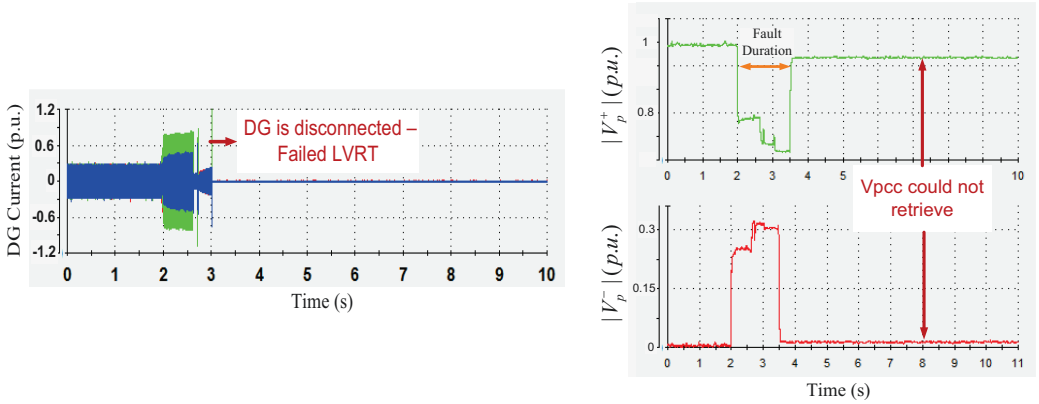

Figure 4.26 Experimental results for fault scenario 2 when K^+=K^-=2.5 and the PLL gains are increased.

Fault scenario 2 – Decreased PLL gains

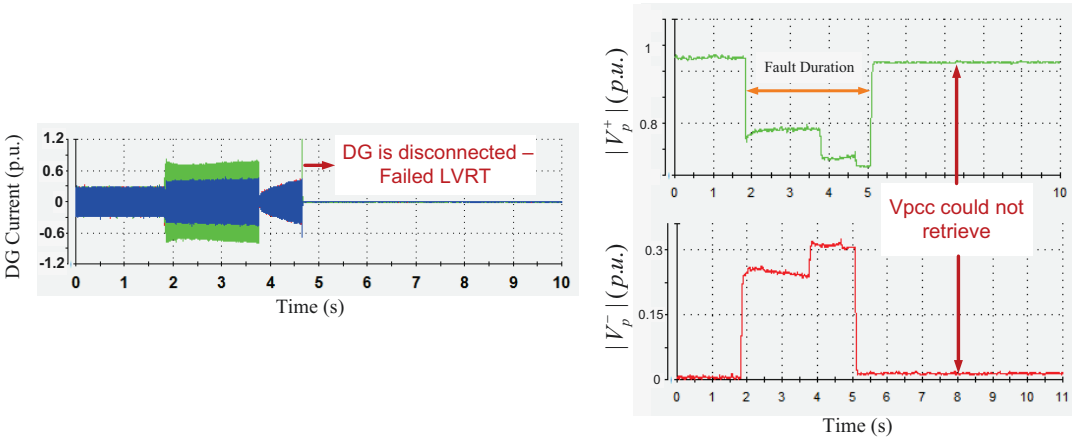

Figure 4.27 Experimental results for fault scenario 2 when K^+=K^-=2.5 and the PLL gains are decreased.

4.6.3.3 Current Controller Gains Effect with Higher Voltage Support

To validate the findings of Section 4.4.2, in the next test case, the FMS-RCI parameters value are increased to 2 to provide higher voltage support in the case of the weak grid condition, compared to the test case of Section 4.6.3.1 above. Besides, to prevent the protection system from disconnecting the CI-DG unit and based on the findings of Figure 4.18, the value of the initially designed current controller integrator gain, K_i, is reduced by 10%. The system experienced Fault Scenario 2, and the results are shown in Figure 4.28. The DG unit remained connected to the grid and represented a successful LVRT operation. Compared to Figure 4.25(b), the

DG unit is generating higher reactive current values during the fault while still respecting the thermal limit (see Figure 4.28(a) and (b)) which results in an improved PCC voltage support.

Fault scenario 2- Improved current controller parameters

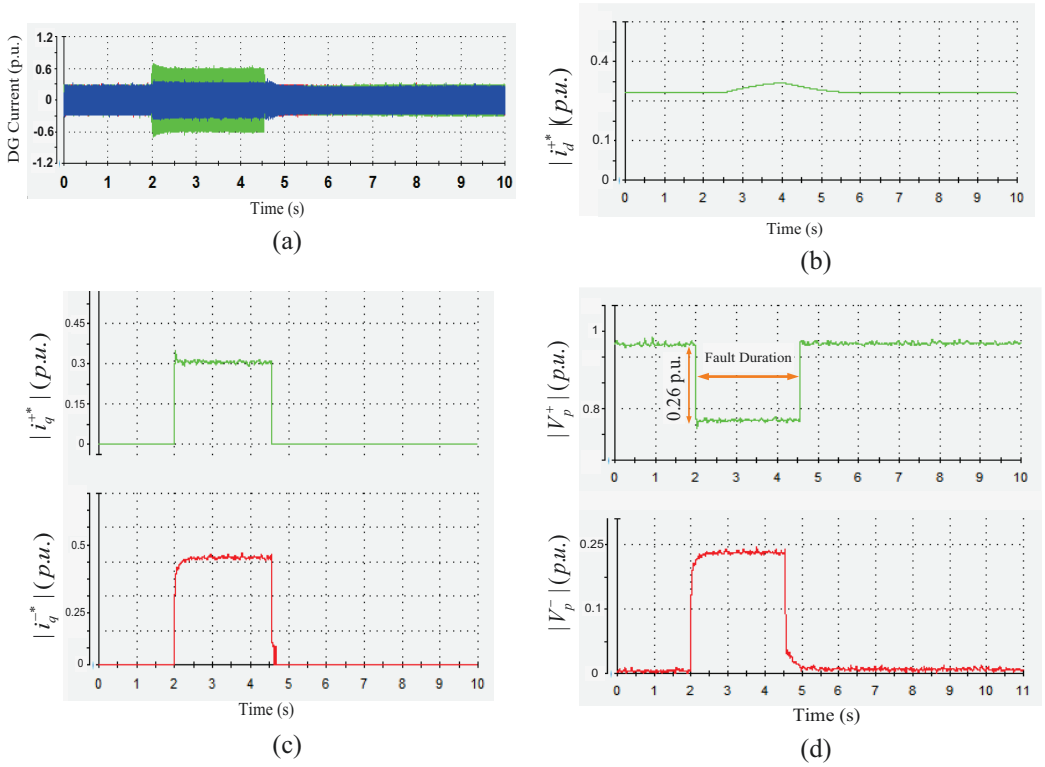

Figure 4.28 Experimental results for the fault scenario 2 with improved current controller gains design when K^+=K^-=2: a) DG current (i_1); b) the injected active current; c) injected reference reactive current values; d) PCC voltage in positive/negative *dq* frames.

4.6.4 Fault Scenario 3

To investigate the effectiveness of the proposed methods under a different voltage unbalance ratio, a two-phase to ground fault is studied in this section. The PCC voltage components are shown in Figure 4.29(d). By comparing these results with Figure 4.28(d), a deeper voltage drop on the positive sequence and lower voltage unbalance with lower negative sequence value can be observed. The same controlling method of Section 4.6.3.3 with the improved current controller parameters and K^+=K^-=2 is used in this study. The results of Figure 4.29 reveal the effectiveness of the proposed methods in delivering a successful LVRT performance.

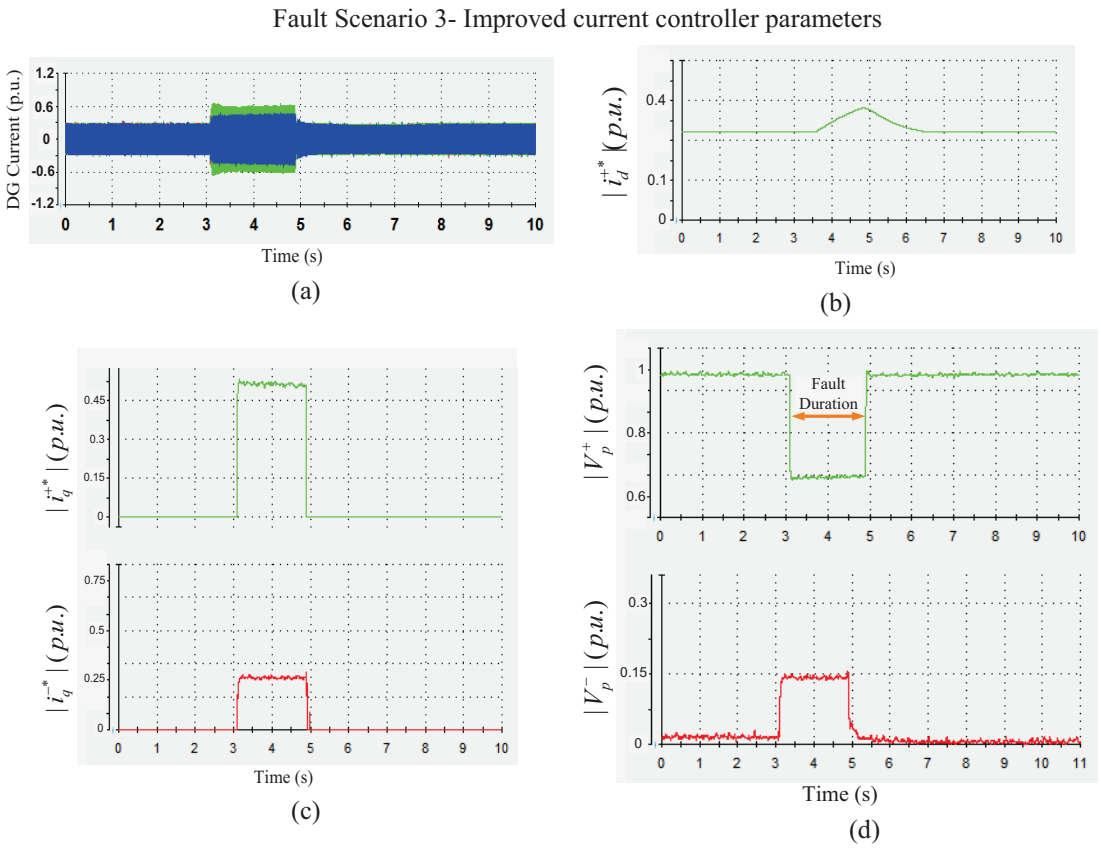

Figure 4.29 Experimental results for the fault scenario 3 with improved current controller gains design when $K^+ = K^- = 2$: a) DG current (i_1); b) the injected active current; c) injected reference reactive current values; d) PCC voltage in positive/negative *dq* frames.

4.7 Summary

Supporting the host grid during voltage dips has become a major connection requirement for large distributed generation units. Because most of the grid faults are unsymmetrical, the recently developed grid-codes suggest the injection of a flexible positive- and negative-sequence reactive current components proportional to the magnitude of the voltage dip at the point of common coupling. However, detailed dynamic analysis of the augmented grid-connected converter with the flexible positive- and negative-sequence current injection function and the characterization of the impact of the grid strength, converter control parameters, and proportionality constants used in the reference currents generation block are not reported in the literature. To fill in this gap, first, a multi-stage linear model of

the augmented nonlinear system dynamics is developed, and the small-signal stability analysis is performed on the system dynamic behavior before, during, and after the fault. The effects of different system and control parameters are studied and characterized. Second, a new and effective model-based controller design method is proposed to maintain the system stability during and after the fault with the consideration of the mutual interaction among different system controllers. Finally, the time-domain simulations and laboratory experiments validate the accuracy and effectiveness of the proposed control method.

Chapter 5

LVRT Performance Improvement in GCC-Based DG Units with Dynamic Loads

Distributed generation (DG) units have gained high momentum as an enabling structure to integrate renewable energy resources in power networks [82]-[84]. Most of DG units are interfaced to the network by voltage source converters, known as grid-connected converter (GCC)-based DG units. With the expected high penetration level of DG units in future power systems and recent progress in power converter topologies and ratings, medium voltage DG units will be subjected to a wide range of both static and dynamic loads. Electromechanical rotor oscillation phenomenon occurs in motors with large megawatt ratings [42], which are directly connected to medium voltage systems (1.0 kV to 30 kV). Typically, motors consume 60% to 70% of the total energy provided by a power system [26]. Ignoring this type of loads in stability analysis of GCC-based DG units results in a large stability operating region, which is unrealistic due to the highly nonlinear load dynamics. These dynamics couple the active power, reactive power, voltage, and supply frequency responses in the system. Therefore, severe stability problems may arise because of neglecting the load dynamics in systems with a high penetration level of MV-DG units.

Several studies are reported in conventional power system analysis to study the impact of large induction machine (IM) loads on power system dynamics [85]-[86]. In small-signal studies of power systems with IMs, since the use of soft-starters only limits motor starting inrush current, it does not change the final steady-state

operating conditions of the motor. Therefore, the small-signal stability analysis will not be affected, and the motor performance will be mainly determined by the motor dynamics [87]. The linearized state-space model of the IM is obtained in [26], [42], [43], [87], where a system eigenvalue spectrum is derived for stability analysis. In the context of microgrids, the impact of IMs on load margins is studied in [87]. An integrated modeling and stabilization method for MV droop-controlled microgrids with IM load is studied in [43] where a small-signal model of a typical MV microgrid system with dynamic loads is presented, and a wide range of droop parameters is studied to keep the system stable and yield the expected control performance. However, a literature survey indicates that detailed analysis and, more importantly, improved stabilization of MV GCC-based DG unit with IM loads, are not reported yet and need special attention. Therefore, this chapter develops comprehensive integrated modeling, stability analysis, and LVRT performance improvement methods for GCC-based DG systems in the presence of dynamic loads.

The static load modeling method is addressed in [26] and [88]-[90] which is suitable for low-voltage applications with small IMs. For small IMs, the rotor-circuit time-constant is small, which represents the fast decay of rotor electrical dynamics as compared with rotor mechanical dynamics [29]. Therefore, the electromechanical rotor dynamics are decoupled, and small IM loads can be modeled by their equivalent steady-state RL circuit or active and reactive power demand. This justifies the use of static load models in the existing low-voltage low-power grid stability studies. However, with the increasing penetration level of DG units in future power networks, it is not reasonable anymore to model larger IM loads with static load equivalents. In fact, electromechanical rotor oscillations in large IMs couple the rotor speed oscillations, which are directly coupled to the rotor flux dynamics and the supply frequency. The time-constant of the rotor-circuit is large, and both electrical and mechanical dynamics of the rotor are coupled. Because rotor oscillations cause the mechanical and electrical power oscillations, the output power of DG units feeding an IM contains the frequency modes of these oscillations [43].

Another missing but essentially important point is the study of the low-voltage ride-through (LVRT) capability of the GCC-based DG units with large IM loads. The LVRT requirement has been recently an important mandate for DG units [6], [19], [78]. This is particularly important when considering the effect of the grid strength on the system performance considering the dynamic loads. In fact, the interactions of GCC-based DG units and the power system are highly dependent on the strength of the ac system. Therefore, it is essential to consider this phenomenon in the LVRT studies. Furthermore, the system operators have imposed new grid codes requiring large DG units to remain connected and improve the voltage profile by reactive current injection (RCI) during short-term grid faults [19] ,[91] . Very recently, the multi-sequence RCI has also been mandated in the German code of VDE-AR-N [38], [40]. Reference [40] further offers to include two controlling parameters in the future standards of GCC-based DG units to support the connection voltage with a combination of boosting the positive-sequence voltage and reducing the unbalance factor. However, the literature still lacks a study on the LVRT capability of GCC-based DG units with the IM loads considering both the stiffness of the host grid and the new multi-sequence RCI requirements.

Motivated by the above shortcomings in the literature, this chapter presents integrated modeling, analysis, and stabilization approach of GCC-based DG units in connection with an IM load. A detailed multi-stage small-signal model of an MV GCC-based DG unit with both dynamic and static loads is developed in the decoupled double synchronous reference frame (DDSRF). The DDSRF is used to enable the implementation of the aforementioned newly imposed grid codes. The model includes the exact 10^{th} order model of the IM load and the 25^{th} order model of GCC-based DG unit along with the network dynamics. The comprehensive multi-stage small-signal model is used to provide the possibility of the grid fault studies for three different operating states of the system: before-fault (BF), during-fault (DF), and after-fault (AF) stages. This model is then used to assess the impact of the IM dynamics on the overall system stability as compared with the static load model and under different grid strength conditions. The Participation factor analysis (PFA) is also conducted to identify the contribution of different states to the

dominant eigenvalues of the GCC-based DG system with dynamic load model. The augmented model-based controllers design method is proposed in this chapter based on the small-signal stability analysis to improve the LVRT performance of the DG system in the presence of the IM dynamics under the strong and weak grid condition. In the proposed design method, the newly imposed multi-sequence RCI requirement has also been considered. The proposed method can identify the optimum value for the control parameters of the system to improve its LVRT performance under different grid conditions and, at the same time, maintain its ability to retrieve the stable condition considering its relative stability margins. Finally, a sensitivity analysis is conducted to characterize the effect of the length of the power line between the IM and DG unit. Theoretical analysis, time-domain simulation results, and experimental results are used to validate the effectiveness of the proposed methods.

5.1 GCC-Based DG Unit with Dynamic Load: Characteristics and Modeling

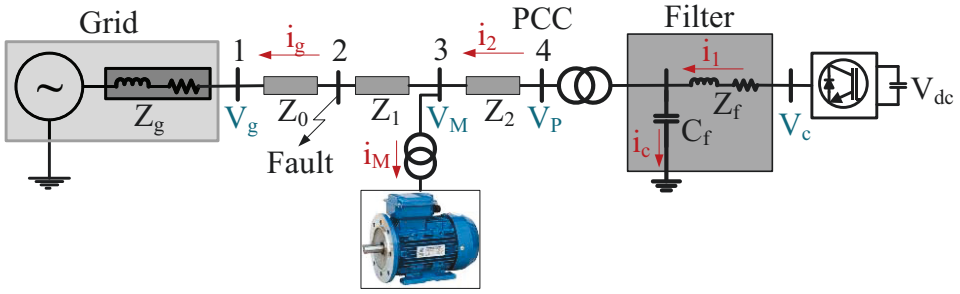

Figure 5.1 GCC-based DG unit with IM load

Figure 5.1 represents a 27.6 kV radial distribution system connected to a dispatchable three-wire DG unit and a typical MV 2240 hP 2.4 kV IM connected to the middle feeder. The DG unit is connected to the MV feeder via a step-up Y/Δ transformer. The term PCC on bus4 stands for the point of common coupling. The system parameters are given in TABLE 5.1. The grid frequency synchronization and active/reactive current control functions are performed at the low-voltage side of the GCC. The DG current controller is designed in the DDSRF on the *dq* coordinates, with the rotating frequencies in the positive and the negative directions

with respect to the fundamental grid frequency; hence, it controls the positive- and negative- sequence current components.

There are three strategies used in this chapter to implement the RCG unit in the GCC control system. The first one is the traditional RCG, with the equations presented in (1.2). This method is still being used in GCC implementations in the distribution system [49], [92]-[93]. The second one is known as the balanced positive-sequence control (BPSC) strategy which is a well-known RCG method in the study of LVRT performance of the GCCs [6], [41], [84]. The related equations are presented in (1.4) to (1.7). Finally, the recently introduced RCG method known as the flexible multi-sequence reactive current injection (FMS-RCI) [49] to satisfy the newly imposed grid codes on the LVRT requirements to inject the reactive current in both positive and negative sequences to support the PCC voltage during an unbalanced grid fault [19], [91], [96]. The equations for the reactive reference current generation in the FMS-RCI method in the DDSRF are presented in (4.1) and (4.2). The active reference current value in this method is obtained based on the traditional equation of (1.2).

TABLE 5.1 System and load parameters

DG unit		Line Parameters (p.u.)	IM Parameters	
Rating	5.0 MVA, 0.44 kV	Z_0=0.0058 + 0.0745i	*Rating*: 2.4 kV, 2240 hp	L_{lr}=0.6 mH/ph
V_{dc}	1000 V	Z_1=0.0058 + 0.0745i	Rs=0.029 Ω/ph	L_m= 34.6 mH/ph
C_{dc}	12 mF	Z_2=0.0029 + 0.0372i	L_{ls}=0.6 mH/ph	J_M=20 kg.m^2
R_f,L_f	0.4 mΩ, 50 μH		R_r=0.022 Ω/ph	Pole pairs = 3

Without loss of generality, the system presented in Figure 5.1 is used to investigate the effect of the dynamic load on the GCC-based DG unit small-signal stability. A small-signal state-space model of the overall system components is developed and presented in the following subsections. The modeling approach can be easily extended to include additional DG units and load models.

5.2 State-Space Model of GCC-Based DG Unit

The control system of a typical GCC-based DG unit consists of 1) phase-locked loop (PLL) system which performs the grid frequency synchronization and provides

the frequency signal to the *dq* transformation blocks implemented in the DDSRF; and 2) the inner current control loop to regulate the filter inductor current (i_1), and damp the resonance peak of the output *LC* filter.

The PLL and current control loop equations including the conventional proportional and integral (PI) compensators and the feedforward PCC voltage signal are listed in (2.22) to (2.25), where the positive and negative *dq* reference frames are assumed to be rotating at the positive and negative directions of the angular frequency (ω), respectively, provided by the PLL. K_p and K_i are the current controller PI compensator gains and, K_{p2} and K_{i2} stand for the same gains in PLL. The current and voltage dynamics for the PCC are given in Sections 2.2.2. and 2.2.3.

5.2.1 State-Space Model of IM

The relation between the IM's stator and rotor voltages and currents in the common synchronous rotating reference frame can be stated by (5.1)–(5.6). Because IM fluxes and currents are not independent, the IM equations can be written using either of them as state variables. However, for the integration of IM state equations into the GCC-based DG unit state-space model, the voltage equations with currents as state variables seems more suitable [43]. Therefore, the relation between the voltage and currents of the stator and rotor can be given in the DDSRF frame as follows:

$$\begin{aligned} V_{Md}^{+} &= -\omega L_{ls} i_{Mq}^{+} + R_s i_{Md}^{+} + L_{ls}\frac{di_{Md}^{+}}{dt} - \omega L_m i_{rq}^{+} + L_m \frac{di_{rd}^{+}}{dt}, \\ V_{Md}^{-} &= \omega L_{ls} i_{Mq}^{-} + R_s i_{Md}^{-} + L_{ls}\frac{di_{Md}^{-}}{dt} + \omega L_m i_{rq}^{-} + L_m \frac{di_{rd}^{-}}{dt} \end{aligned} \tag{5.1}$$

$$\begin{aligned} V_{Mq}^{+} &= \omega L_{ls} i_{Md}^{+} + R_s i_{Mq}^{+} + L_{ls}\frac{di_{Mq}^{+}}{dt} + \omega L_m i_{rd}^{+} + L_m \frac{di_{rq}^{+}}{dt}, \\ V_{Mq}^{-} &= -\omega L_{ls} i_{Md}^{-} + R_s i_{Mq}^{-} + L_{ls}\frac{di_{Mq}^{-}}{dt} - \omega L_m i_{rd}^{-} + L_m \frac{di_{rq}^{-}}{dt} \end{aligned} \tag{5.2}$$

$$V_{rd}^{+} = -s^{+}\omega L_{lr} i_{rq}^{+} + R_r i_{rd}^{+} + L_{lr}\frac{di_{rd}^{+}}{dt} - s^{+}\omega L_m i_{Mq}^{+} + L_m \frac{di_{Md}^{+}}{dt}, \tag{5.3}$$

$$
\begin{aligned}
V_{rd}^{-} &= s^{-}\omega L_{lr} i_{rq}^{-} + R_r i_{rd}^{-} + L_{lr}\frac{di_{rd}^{-}}{dt} + s^{-}\omega L_m i_{Mq}^{-} + L_m\frac{di_{Md}^{-}}{dt} \\
V_{rq}^{+} &= s^{+}\omega L_{lr} i_{rd}^{+} + R_r i_{rq}^{+} + L_{lr}\frac{di_{rq}^{+}}{dt} + s^{+}\omega L_m i_{Md}^{+} + L_m\frac{di_{Mq}^{+}}{dt}, \\
V_{rq}^{-} &= -s^{-}\omega L_{lr} i_{rd}^{-} + R_r i_{rq}^{-} + L_{lr}\frac{di_{rq}^{-}}{dt} - s^{-}\omega L_m i_{Md}^{-} + L_m\frac{di_{Mq}^{-}}{dt}
\end{aligned}
\tag{5.4}
$$

where L_{ls} and R_s are the stator inductance and resistance; L_{lr} and R_r are the corresponding rotor parameters; L_m, s, and ω are the linkage inductance, rotor slip, and the angular frequency of the stator supply, respectively. i_M stands for the stator current and i_r is the rotor current. The electromagnetic torque in terms of stator and rotor currents can be expressed as

$$
Te^{+} = \frac{3}{2}\frac{\rho}{2}L_m(\mathrm{i}^{+}{}_{Mq}\mathrm{i}^{+}{}_{rd} - \mathrm{i}^{+}{}_{Md}\mathrm{i}^{+}{}_{rq}),\ Te^{-} = \frac{3}{2}\frac{\rho}{2}L_m(\mathrm{i}^{-}{}_{Mq}\mathrm{i}^{-}{}_{rd} - \mathrm{i}^{-}{}_{Md}\mathrm{i}^{-}{}_{rq}) \tag{5.5}
$$

The relation between torque and the mechanical speed can be obtained in terms of the motor slip and stator angular speed as

$$
Te^{+} - T_L{}^{+} = J\frac{d}{dt}((1-\mathrm{s}^{+})\omega),\ Te^{-} - T_L{}^{-} = J\frac{d}{dt}((\mathrm{s}^{-}-1)\omega) \tag{5.6}
$$

In (5.5) to (5.6), ρ, J, and T_L are the number of poles, combined motor and load inertia, and the load torque, respectively. Note that since the rotor circuit of the IM is shorted, the V_r values are set to zero. The machine parameters are given in TABLE 5.1.

By linearizing the dynamic equations of the DG unit, power network, IM and the RCG equations, the state and input variables for the complete system can be derived as

$$
\begin{aligned}
X_{35\times1} &= \begin{bmatrix} [X_{25\times1(DG-Network)}\ ] \\ [X_{10\times1(IM)}] \end{bmatrix} = \\
&\begin{bmatrix} [i_{gd}^{+}, i_{gq}^{+}, i_{gd}^{-}, i_{gq}^{-}, i_{1d}^{+}, i_{1q}^{+}, i_{1d}^{-}, i_{1q}^{-}, \int e_d^{+}dt, \int e_q^{+}dt, \int e_d^{-}dt, \int e_q^{-}dt, \\ \omega, v_{pd}^{+}, v_{pq}^{+}, v_{pd}^{-}, v_{pq}^{-}, v_{f\,d}^{+}, v_{f\,q}^{+}, v_{f\,d}^{-}, v_{f\,q}^{-}, i_{2d}^{+}, i_{2q}^{+}, i_{2d}^{-}, i_{2q}^{-}]^T \\ [i_{rd}^{+}, i_{rq}^{+}, i_{rd}^{-}, i_{rq}^{-}, i_{Md}^{+}, i_{Mq}^{+}, i_{Md}^{-}, i_{Mq}^{-}, s^{+}, s^{-}]^T \end{bmatrix}
\end{aligned}
\tag{5.7}
$$

$$
u_{12\times1} = \begin{bmatrix} u_{6\times1(DG-Network)} \\ u_{6\times1(IM)} \end{bmatrix} = \begin{bmatrix} [v_{gd}^{+}, v_{gq}^{+}, v_{gd}^{-}, v_{gq}^{-}, P^{*}, Q^{*}]^T \\ [v_{Md}^{+}, v_{Mq}^{+}, v_{Md}^{-}, v_{Mq}^{-}, T_L{}^{+}, T_L{}^{-}]^T \end{bmatrix} \tag{5.8}
$$

where (5.7) and (5.8) demonstrates the related 25 states and six input variables of the GCC-based DG unit and the connected power system and ten states and six input variables related to the IM dynamics. The obtained state matrix of the system considering the BPSC RCG method is presented in the Appendix D. Further modeling details for the GCC-based DG unit can be found in Chapter 2 and [48].

In addition, since the DG unit will be subjected to different operating states under the low voltage conditions, the three-stage modeling method, presented in 3.2.2, is adopted in this chapter to overcome this limitation.

5.3 Stability Analysis

To demonstrate the importance of using the complete dynamic model of the IM and not to simplify it with a static load model (i.e., the ZIP model [26]), the complete small-signal model of the GCC-based DG unit is obtained with the consideration of the mentioned two load modeling approaches: static and dynamic. The IM load model adds six more states to the complete state-space model of the system, comparing to the static load model. The eigenvalue spectrum for both models are obtained and shown in Figure 5.2 where the frequency-scale separation of the system modes are also indicated (the static load model has four additional non-dominant modes with real values of around -3.6× 10^5, which are not shown in Figure 5.2).

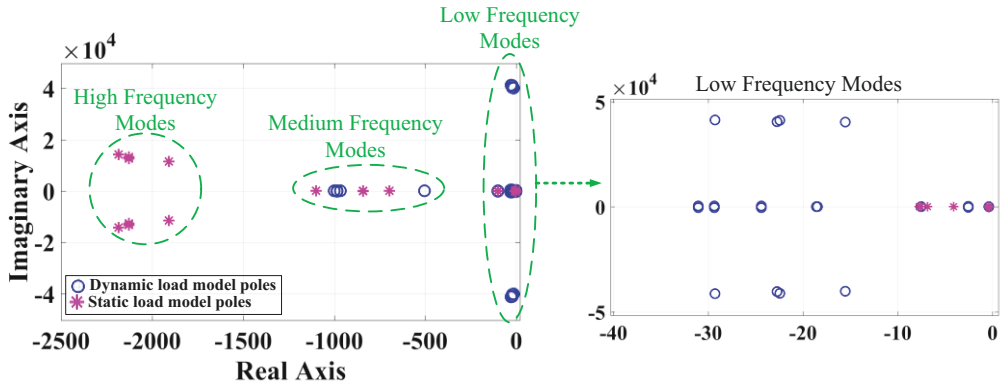

Figure 5.2 Eigenvalues of the GCC-based DG unit system with static and dynamic load models.

The low-frequency modes are the most dominant and, therefore, the most fundamental modes for system stability analysis. As illustrated, for the static load model, the 29 system modes are distributed in high, medium and low-frequency ranges, with only seven modes located in the range of low-frequency (i.e., 0 to 50 Hz), shown in Figure 5.2(b). However, for the IM load modeling, all 35 modes are distributed in the range of the medium and low frequency, which represents an overall shift in the system modes towards lower frequencies and so, lower relative stability. Besides, as shown in Figure 5.2(b), there are 26 modes of the IM load modeling located in the low-frequency range which denotes 19 more dominant modes compared to the static load model. Therefore, considering the transient stability of the system, the system with IM load modeling demonstrates considerably higher sensitivity and lower relative stability compared to the static load model.

It should be noted that rotor oscillations are characterized by their low-frequencies, and they cannot be effectively filtered by the average low-pass filters in the DG units control system [94]. Due to the lightly-damped nature of rotor oscillations in large IMs, the feedback system can be subjected to power oscillations and even system instability, especially in the case of a fault occurrence. Therefore, as revealed by Figure 5.2, although equations (5.1)-(5.6) add more complexity to the dynamic model of the system, considering them is essential for accurate stability analysis of the GCC-based DG unit system.

Another study based on the PFA [26] demonstrated the relative participation of each state variable to the mentioned 26 low-frequency modes of the IM dynamic model, shown in Figure 5.2(b). The normalized participation factors greater than zero are obtained for all 26 modes. Amongst them, there are nine modes which are highly related to the IM dynamics state variables (i.e., has non-zero participation in the IM related dynamics). The PFA results for these nine modes are listed in TABLE 5.2. Note that the stator flux is composed of both the stator and rotor current components, and therefore, they highly participate to the demonstrated eigenvalues when using the dynamic load modeling. It is observed that these nine modes are related to the IM dynamics state variables, and their participation factor in all other

variables are zero. Therefore, the system stability can be remarkably affected in the presence of such a load.

TABLE 5.2 PFA results for the nine modes related to the IM dynamic state variables

State Variables	Eigenvalues (modes)				
	Set1 (13,14)	Set2 (20,21)	Set3 (22,23)	Set4 (29)	Set5 (30,31)
Δi_{rd}^{+}	0.23	0.23	0	0.24	0
Δi_{rq}^{+}	0.23	0.26	0	0.27	0
Δi_{rd}^{-}	0	0	0.25	0	0.25
Δi_{rq}^{-}	0	0	0.25	0	0.25
Δi_{Md}^{+}	0.24	0.24	0	0.23	0
Δi_{Mq}^{+}	0.23	0.26	0	0.26	0
Δi_{Md}^{-}	0	0	0.25	0	0.25
Δi_{Mq}^{-}	0	0	0.25	0	0.25
ΔS^{+}	0.03	0	0	0	0
ΔS^{-}	0.03	0	0	0	0
Other state variables	0	0	0	0	0

The eigenvalue and PFA analyses results demonstrate that there are nine dominant poles in total which are associated with the IM state variables and according to their location (i.e., less-damped modes resulting in more oscillatory system responses), they have a high impact on the overall GCC-based DG unit system stability. In fact, these modes can be regarded as the source of added oscillatory response to the system, and therefore, they should be considered in stability studies.

Furthermore, the participation factors obtained in TABLE 5.2 imply that all the dominant eigenvalue pairs shown in Figure 5.2(b) are very sensitive to the stator and rotor current components. This leads to the fact that the dominant system modes are mainly influenced by the active power component drawn by the motor. This is in agreement with the familiar fact that controlling the stator currents is an effective

way to reshape the open-loop IM dynamics, which is the case in IM drive systems [95]. However, in the system under study with the direct connection of the IM, the motor currents may not be available for stabilization. In this case, the motor power is shared among the DG unit and the grid. Therefore, some methods are proposed in this chapter to improve the during-fault voltage support by the DG unit. In this way, the injected active and reactive current components of the DG unit result in an improved power supply to the IM and boost its functionality to ride through the fault condition.

5.4 Proposed Stability and LVRT Improvement Methods

Before 2003, no requirements were imposed from utility grids for LVRT performance of wind turbine generator systems (WTGSs). However, in that year, E.ON-Netz of Germany was the first to implement those requisites into their grid code [94]. According to the guideline of the grid code, WTGS needs to stay connected and provide reactive power into the grid. Only when the grid voltage drops below the guideline of the grid code, a WTGS is allowed for disconnection from the grid [19]. Also, LVRT for photovoltaic (PV) plants was mentioned in the German grid code from January 2011 to provide uninterrupted service in the case of grid disturbances. However, to the best of authors' knowledge, the LVRT performance of a GCC-based DG unit in the presence of an IM load is not reported in the literature yet. On the other hand, based on [26] the IMs typically consume 60% to 70% of the total energy provided by a power system. Therefore, the dynamics related to motors are usually the most important aspects in dynamic analysis of system loads and, therefore, in the analysis of modern power systems it is also crucial to consider the IM dynamics with respect to the mandated LVRT requirements in the grid codes [19], [38], [91]. As mentioned in Section 2.3, SCR is a standard definition to quantify the strength of an ac system as compared to the rating of the connected DG unit. Therefore, this quantity will be used in this chapter as an indication of the grid strength.

The LVRT performance of the presented system of Figure 5.1 under a short-term unbalanced grid fault is investigated in this section. For the time-domain simulation studies, the system above is implemented in MATLAB/Simulink environment. Three different RCG methods, described in Section 4.1, are implemented, and the system performance is monitored for a satisfactory LVRT. The location of the fault is also shown in Figure 5.1. It is an unbalanced two-phase to ground grid fault happened at t= 1.8s and lasted for 200 ms.

5.4.1 LVRT under Strong Grid Condition

To investigate the LVRT performance of the system under study when connected to a strong grid, the above-mentioned unbalance fault scenario is studied when the DG unit is connected to a grid with SCR≅ 10. The mentioned three RCG methods are implemented and tested under the same condition. The results revealed that all three strategies are able to maintain the DG unit connected during and after the fault when the connected grid is strong.

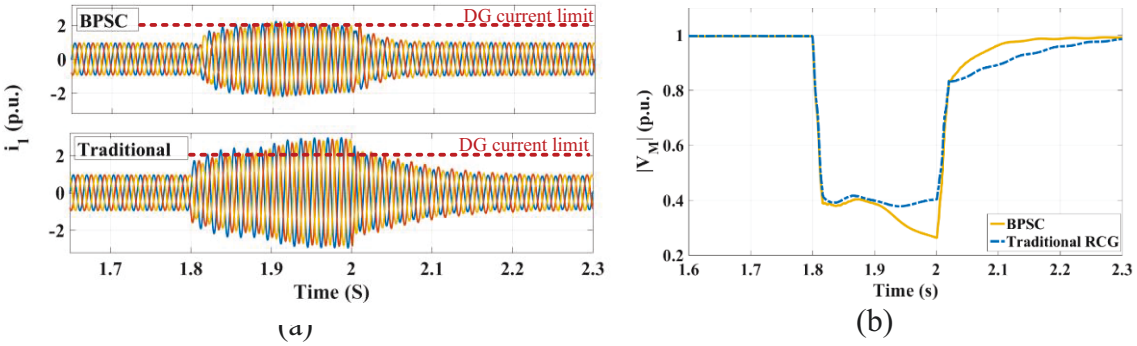

Figure 5.3 Time-domain simulation results of employing the traditional and the BPSC RCG methods during an unbalanced fault when the connected grid is strong.

Figure 5.3 compares the results of employing the traditional and the BPSC RCG strategies. These two methods perform almost the same without any negative-sequence reactive-current compensation. Between them, the BPSC delivers the balanced current with lower maximum-phase value during the fault, and shorter settling-time after the fault. Besides, assuming a protection limit for the three-phase DG unit current value at 2.0 p.u., Figure 5.3(a) shows that employing the traditional RCG may trigger the protection devices. In fact, if the fault duration passes the

adjusted time of the over-current protection system, it can result in DG unit disconnection and LVRT failure.

Because the BPSC and the traditional RCG methods have no specific rule on the reactive-current injection according to the voltage drop value, during the fault, they cannot be chosen to provide the LVRT requirements considering the grid codes [19], [38], [91]. However, the FMS-RCI method improves the voltage profile during the fault by injecting the reactive current in both positive and negative sequences. Therefore, in the next test, the LVRT performance of the system is studied while employing the FMS-RCI strategy with the K^+ and K^- parameters set to 2. This value is chosen to be compatible with the regulated value of the reactive-current injection under the balanced fault condition presented in [19]. Figure 5.4 shows the FMS-RCI strategy results compared to the BPSC method to demonstrate their difference in supporting the IM bus voltage and improving the active and reactive power profiles of the DG unit and the IM.

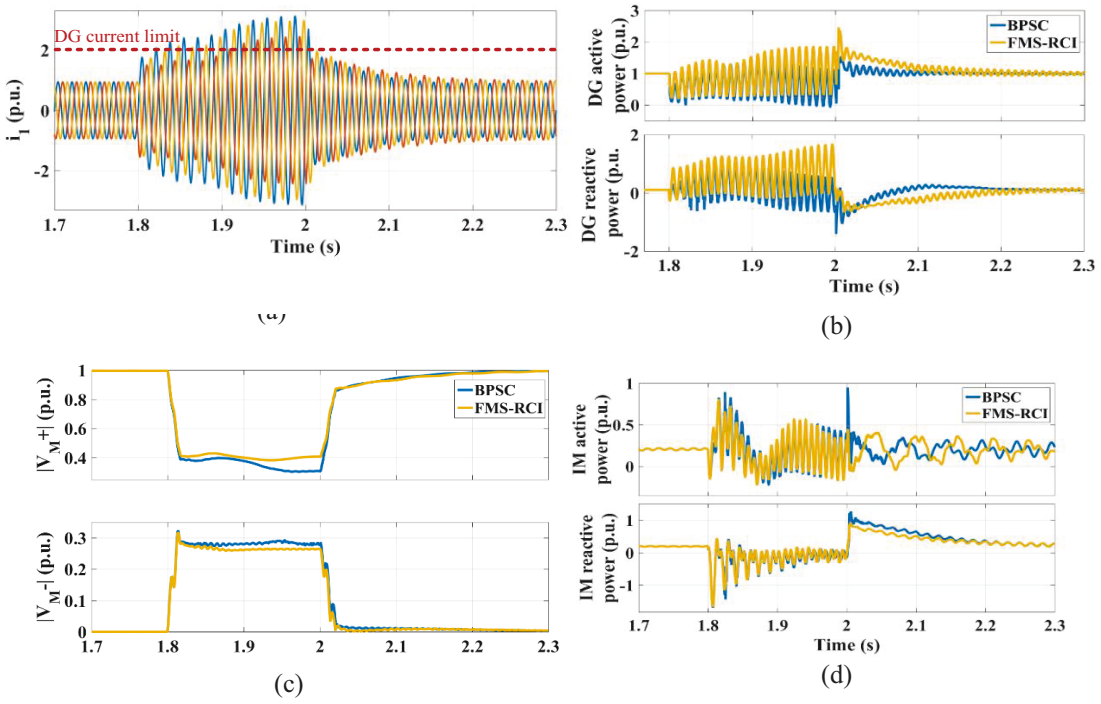

Figure 5.4 Employing the FMS-RCI and the BPSC strategies during an unbalanced fault when the grid is strong.

Figure 5.4(b) reveals that the FMS-RCI generates a higher average power in the DG unit during the fault. With the IM, the FMS-RCI strategy provides a

smoother recovery on the active/reactive power after the fault. The only possible problem in the application of the FMS-RCI with the injection of the flexible reactive-current during the fault is that the maximum phase value of i_1 stays over the reasonably assumed 2 p.u. limit (Figure 5.4(a)). Therefore, to find a remedy, a model-based current controller design method is utilized in the next section using the small-signal stability analysis of the system for the before-fault (BF) and during-fault (DF) stages.

5.4.1.2 LVRT Performance Improvement using Model-Based Controller Design

In this method, the initially designed current controller parameters, i.e., K_p and K_i of the PI compensator are changed, and the eigenvalue locus of the complete system is obtained. The initial design of these parameters is obtained based on the pole-zero cancellation method described in [24].

In the mentioned model-based controller design, the controller parameters are being changed, and the eigenvalue locus of the system is monitored for the best relative stability condition. Figure 5.5 shows the eigenvalue locus of the system when the K_p and K_i parameters are increasing for the DF and BF stages. As demonstrated, for the DF stage, there are three pole-pairs moving farther from the imaginary axis to a specific point, from which, they return their path towards the imaginary axis. This point is when the value of the K_p and K_i parameters are increased to 17 times their initial value. Therefore, there is a limitation in increasing the K_p and K_i parameters to improve the relative stability of the system. However, considering the BF stage, which has the same RCG method as the AF stage, it is observed that by increasing the K_p and K_i parameters, two dominant poles move towards the imaginary axis. Therefore, there is another limitation on increasing the current controller parameters to keep the system stability for the normal operation of the DG unit, before and after the fault. Further investigation revealed that by increasing the K_p and K_i parameters more than four times, the system would show unstable poles for the BF stage. From now on, this method is called the current controller improved design or the CCID method.

Also, it is worth mentioning that by comparing the results of Figure 5.5 with those of Figure 5.2(b), it is inferred that these affected poles by the CCID are amongst those which are added to the low-frequency area by considering the dynamic load. Again, it demonstrates the importance of using the detailed dynamic load model instead of simplifying it with the static load model.

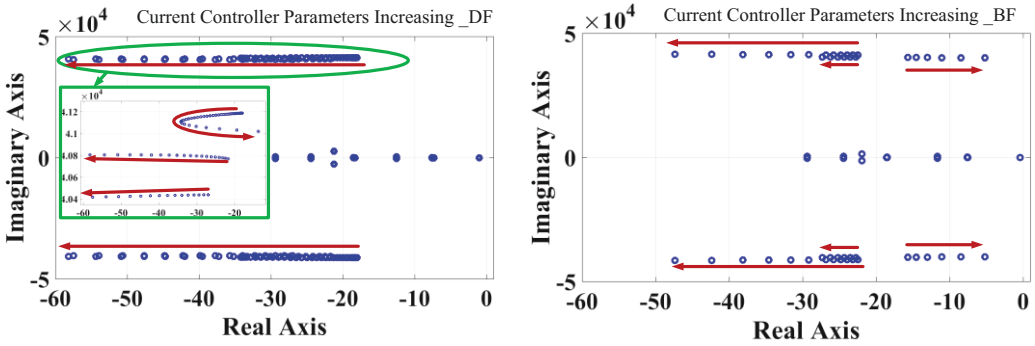

Figure 5.5 Eigenvalue locus of the most dominant poles when the current controller parameters are increasing when employing the FMS-RCI strategy in: a) DF-stage, b) BF-stage.

To investigate the effectiveness of this improved model-based CCID method in preventing the DG unit over-current problem, while keeping the same control parameters value (K^+ and K^-) for the FMS-RCI strategy, the time-domain simulation results of the system are obtained. Figure 5.6 shows the results for the case of K_p and K_i parameters increased to 2.5 times their initially designed values. Figure 5.6(a) shows that the maximum phase value of i_1 is considerably reduced, compared to Figure 5.4(a). However, the system is acting slower in returning to its steady-state after the fault clearance which was predictable by considering the results of Figure 5.5(b). In fact, the speed of decay of the transient response depends on the value of the time constant of the most dominant poles [97]. By representing a complex pole by $-\sigma \pm \omega$, the time constant is defined by $1/\sigma$ which justifies the slower transient response or higher settling for the system after the fault. The IM bus voltage, active and reactive power have not experienced any remarkable change. Therefore, the CCID could effectively reduce the possibility of the LVRT failure due to the potential DG unit over-current.

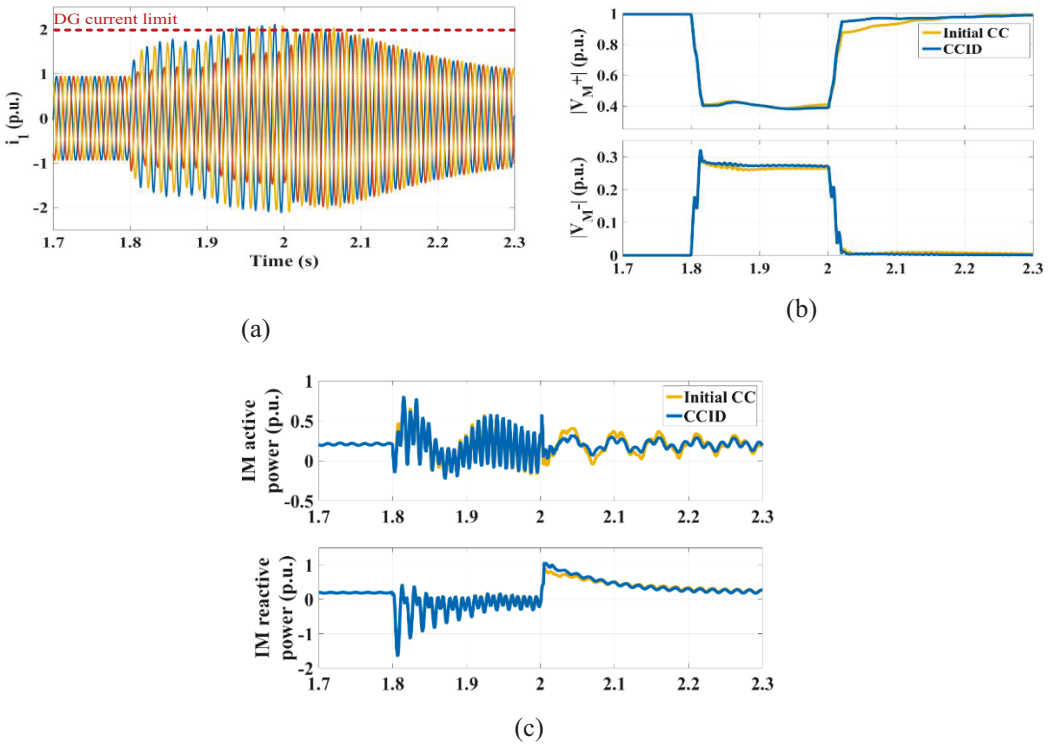

Figure 5.6 The effect of improving the current controller parameters design based on the small-signal stability analysis.

5.4.2 LVRT under Weak Grid Condition

As mentioned above, the strength of the ac system plays an important role in the interactions between the DG unit and the power system. Considering the LVRT requirements, because a weak grid has a lower ability to support the load during the fault, it is more probable to get a DG unit disconnection and failure of the LVRT. In this subsection, the results are presented for the case of a system with SCR≅ 2 (weak grid) and the same fault scenario of Section 5.4.1, considering three RCG methods.

Figure 5.7 shows the system performance with the traditional RCG method. As demonstrated, after the fault clearance, the DG current value has elevated and passed the DG current limit. In fact, the PCC voltage cannot return to its normal value after the fault clearance. Therefore, the DG current is increased to deliver the required power. It ultimately results in the DG unit disconnection, due to the protection system function, and the LVRT failure. The motor torque and speed are also dropped down.

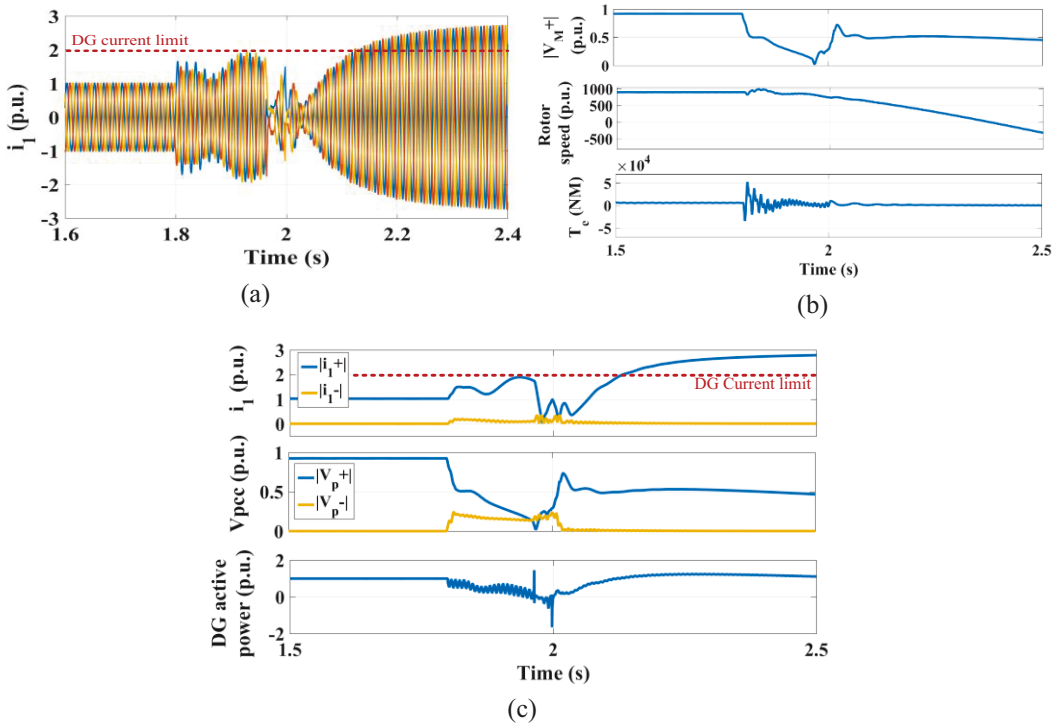

Figure 5.7 LVRT performance of the system under a weak grid condition using the traditional RCG method

To find the best RCG method to satisfy the LVRT requirements, the other two RCG methods, i.e., the BPSC and FMS-RCI, are used and evaluated. These strategies are also advised and studied in many LVRT-related studies [40]-[41], [84]. The same fault scenario occurred and the results are obtained and presented in Figure 5.8. In this test, the initial design of the FMS-RCI controlling parameters, K^+ and K^-, are based on what is imposed in the German grid code of [19] for the symmetrical faults and what is presented in [40] for the application of the FMS-RCI. Therefore, the initial values of K^+ and K^- are set to 2.

As shown in Figure 5.8, the BPSC method has wholly failed in retrieving to its normal condition after the fault clearance when the connected grid is weak. The positive-sequence of the PCC voltage profile has remained low, and the DG unit has not been able to generate the expected amount of the active and reactive power after the fault. However, because the FMS-RCI method can better support the PCC voltage by injecting the reactive current during the fault in both positive and negative sequences, it has been able to boost up the PCC voltage faster than the BPSC after the fault clearance. Besides, Figure 5.8(c) and (d) show that the FMS-

RCI has clearly improved the system transient performance during and after the fault. Therefore, in the case of a weak grid condition, choosing the FMS-RCI method seems the only reasonable choice for the LVRT studies on a GCC-based DG unit system connected to an IM load. However, because the connected grid is weak and the DG unit is mainly providing the required power for the IM load, the results show that the existing system is not fast enough in recovering after the fault clearance. As illustrated in Figure 5.8(a), the DG unit current stays high for a long period after the fault which can result in the DG unit disconnection. Also, the PCC voltage finally fails in getting back to its normal value. Therefore, the obtained results imply that it is necessary to improve the system response to let the DG satisfy the LVRT requirements and remain connected during and after the fault occurrence.

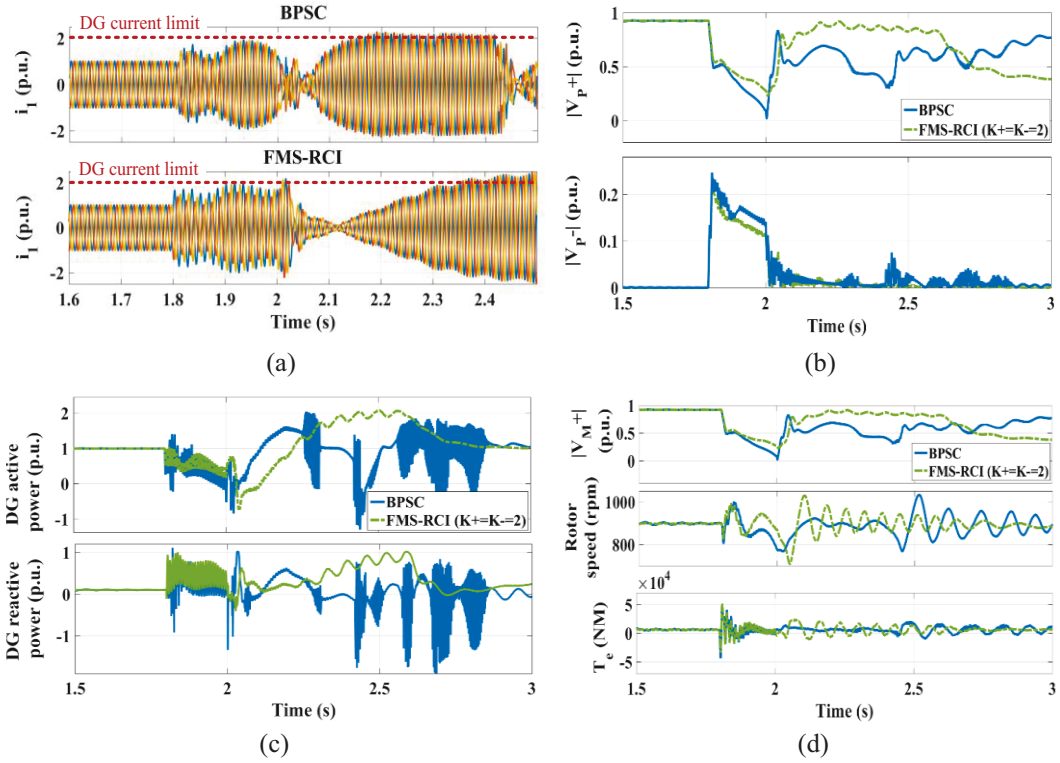

Figure 5.8 LVRT performance of the system under weak grid condition using the BPSC and the FMS-RCI RCG methods with the initial proposed controlling parameters.

5.4.3 Proposed Model-based LVRT Performance Improvement Methods

As the first step, the proposed CCID method presented in Section 5.4.1 is studied for the weak grid condition in both DF and BF stages. The eigenvalue locus of the

system is obtained when the K^+ and K^- are set to 2, and the current controller parameters are increasing. The trend is completely similar to what is presented in Figure 5.5 for the strong grid condition. Therefore, due to the space limitation, it is not shown here again. According to the mentioned small-signal stability analysis, the current controller parameters, i.e., K_p and K_i, are increased to 2.5 times their initial values.

One other possible and reasonable solution to improve the LVRT performance of the DG unit in the presence of the IM load and under a weak grid condition can be increasing the PCC voltage support during the fault in the FMS-RCI strategy. This can be obtained by choosing higher RCG controlling parameters, i.e., higher K^+ and K^- values. In this way, the PCC and therefore, the IM bus voltages will experience lower voltage drop (due to the injection of more positive-sequence reactive current) and lower unbalance (due to the injection of more negative-sequence reactive current) during the fault. Therefore, although the value of K^+ and K^- parameters is different from what is suggested in [40], based on the above-presented results, it seems mandatory in the case of a weak grid condition to keep the DG unit connected to the grid and satisfy the LVRT requirements. However, to the date, there is no study presented in the literature to investigate the limitation on selecting the value of the K^+ and K^- parameters considering the grid strength, the depth of the voltage dip, and the DG unit constraints.

To find this threshold, first, the small-signal stability analysis is carried out on the complete linear model of the system using the DF-stage modeling. In fact, changing the value of the K^+ and K^- parameters is only valid when the DF-stage modeling is being used. The result is shown in Figure 5.9 when increasing the K^+ and K^- values from 2 to 5. There are four dominant pole pairs affected by changing the value of K^+ and K^-, amongst them two pairs start moving towards the right-half plane (RHP), denoting lower transient stability in the system. The interesting point is that these two pairs are the same which were moving towards left by using the CCID method for the DF stage (refer to Figure 5.5(a)). Therefore, although increasing the K^+ and K^- parameters move these poles towards lower relative

stability, the combination of this tuning method with the CCID method can compensate for this undesirable effect to some extent.

Therefore, the limitation on increasing the value of K^+ and K^- parameters is applied by the consideration of maintaining the relative stability of the system. This lower stability threshold can be effective on the fault clearance where the system will experience a significant transient in the voltage and current values and therefore, in the system states. Further investigation demonstrated that increasing the K^+ and K^- parameters up to 13 will still keep the system stable with all poles on the left-half plane (LHP). After that point, the system will experience unstable poles. However, even for setting K^+ and K^- close to 13, the system will have a high sensitivity to the sudden changes such as an unexpected fault. Consequently, by conservatively choosing the value of K^+ and K^- parameters as five, the system is supposed to represent a faster response, higher voltage support and ultimately a successful LVRT performance while keeping a reasonable stability margin on the transients.

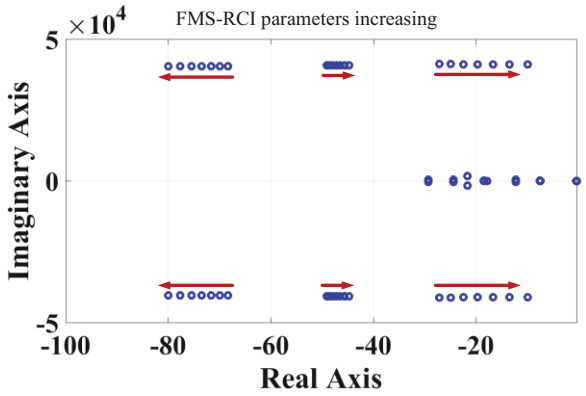

Figure 5.9 Eigenvalue locus of the most dominant poles when the FMS-RCI controlling parameters are increasing in DF-stage model.

To verify the effectiveness of the proposed methods, the time-domain simulation results of the system are obtained under the same fault scenario and connection to the same weak grid with SCR≅ 2. The results are shown in Figure 5.10. It represents a successful LVRT performance in which the value of the DG unit current, i_1, is remained below the limit, during and after the fault. Compared to Figure 5.8, an apparent improvement in the voltage profile of the PCC and the IM bus is observed in Figure 5.10(b) and (d). Besides, all presented system values

illustrate the faster recovery on the fault clearance. It should be noted that, because the DG unit is mostly in charge of providing the IM power demand, the quality of the provided active and reactive power (P and Q) by the DG unit is remarkable from the IM point of view. As demonstrated, the injected P and Q during and after the fault is improved, compared to Figure 5.8(c). This enhancement is also observable on the IM rotor speed and electromagnetic torque profiles of Figure 5.10(d).

Further analysis shows that the DG unit will ride through the fault successfully, even if the IM load gets disconnected while the DG unit control parameters are still set on the proposed enhanced values.

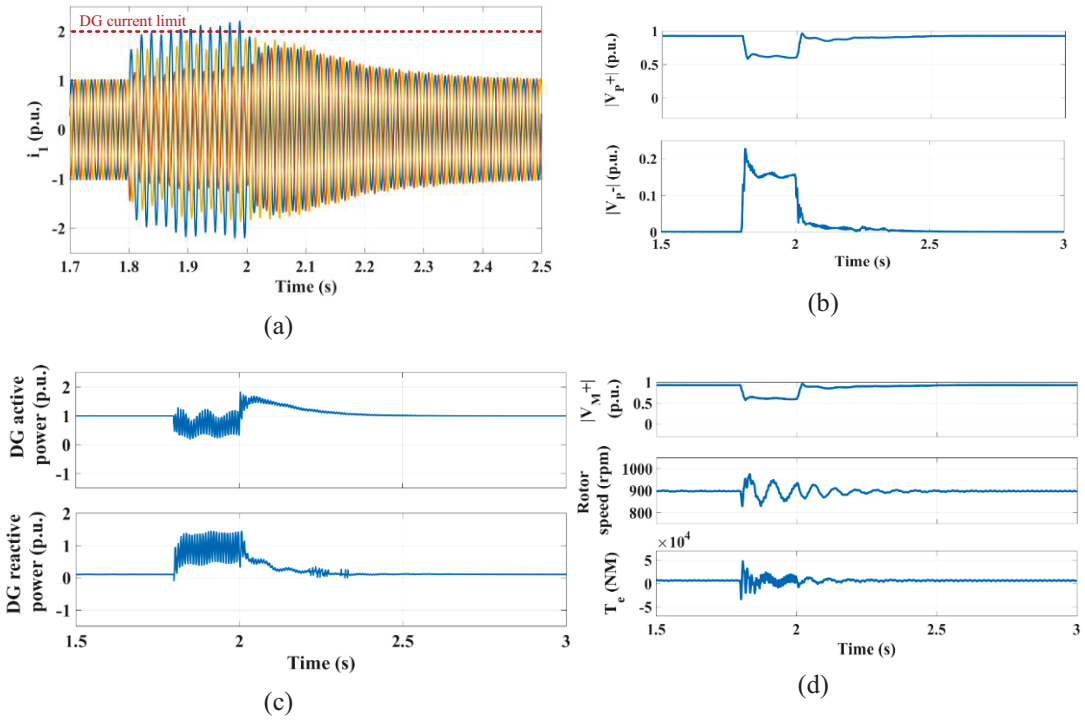

Figure 5.10 Successful LVRT performance of the system under weak grid condition using improved FMS-RCI strategy with the proposed increased controlling parameters (K^+=K^-=5).

To investigate the effectiveness of the inferred conclusion of the eigenvalue analyses presented in Figure 5.9 about the limitation on increasing the FMS-RCI controlling parameters, another test case is studied while the values of K^+ and K^- parameters are set to 7 under the same fault and grid condition. The results are presented in Figure 5.11. Although the profile of the voltage support during the fault is improved, the system is not able to retrieve to its balanced condition after the fault. It should be noted that neither the positive- nor the negative-sequence

values of the PCC voltage has not passed the defined boundaries of (4.1) and (4.2) for the FMS-RCI strategy from where the reference reactive currents should be set to 1.0 p.u. However, due to the reduced stability margin of the whole system, as observed in the small-signal stability analysis of Figure 5.8, the RCG system is unable to rapidly follow the sudden change in $|V_p^-|$ on the fault clearance. Therefore, the injection of the negative-sequence reactive current is continued even after the fault is cleared, and the system is failed in satisfying the LVRT requirements.

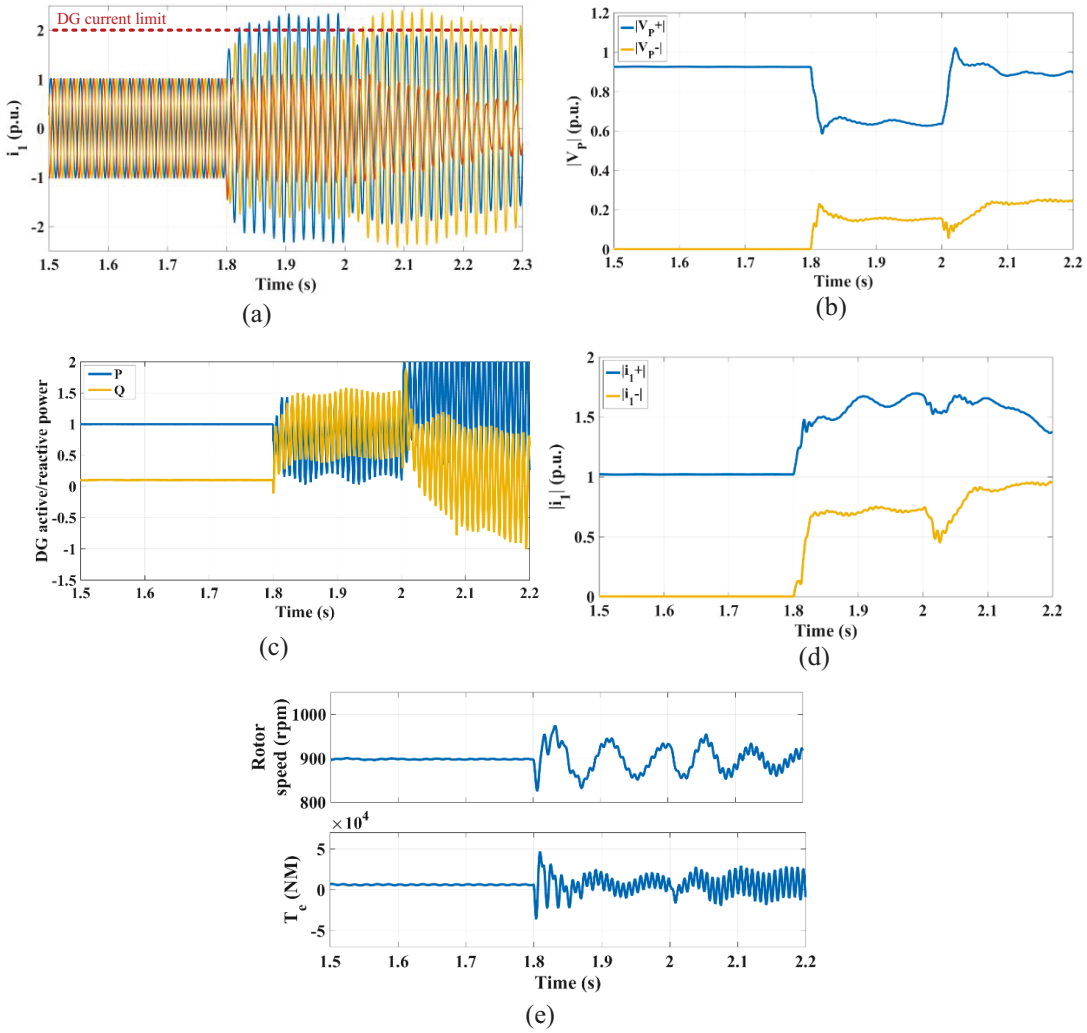

Figure 5.11 LVRT performance of the system under weak grid condition using the FMS-RCI strategy with higher controlling parameters (K^+=K^-=7).

To illustrate the eigenvalue spectrum of each test case considering the related DF-stage values, Figure 5.12 is presented for the most dominant system poles. It is

observed that for the case of K^+=K^- =7, two system modes have moved to the unstable condition for the DF state values. These results confirm the illustrated time-domain simulation results and validate the developed analytical model.

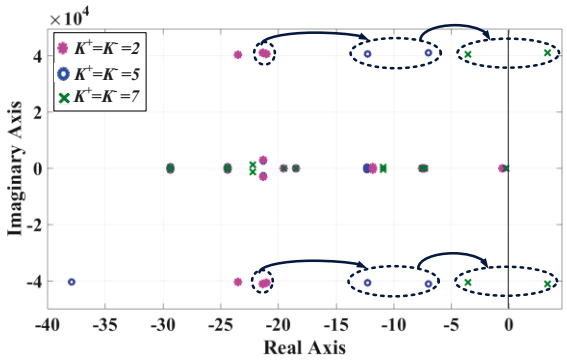

Figure 5.12 The effect of increasing the FMS-RCI parameters on the most dominant poles of the system during the fault.

5.5 Sensitivity Analysis on The IM Location Relative to The DG Unit

Another missing but significant study on the stability performance of a GCC-based DG unit in the presence of the IM load is an investigation on the effect of the distance between the DG unit and the IM load and, how it can affect the relative stability of the entire system. To perform this study, in the obtained linear state-space model of the system, the length of the power line between the DG unit and the IM, presented by Z_2 (refer to Figure 5.1), is increased by increasing its magnitude (starting from 0.01 p.u.) while its angle, presented by the X/R ratio, is kept constant at 12. Figure 5.13 shows the obtained eigenvalue locus for both strong and weak grid conditions. For both cases, although the most dominant pole of the system is slowly moving towards left, there are two other poles quickly moving to the right. More investigations revealed that by increasing the magnitude of Z_2 more than 0.4 p.u. for the strong grid and more than 0.1 p.u. for the weak grid condition, the system represents unstable poles in the RHP. Therefore, it should be considered that there is a limitation on the length of the power line when installing a DG unit close to an IM load. Although longer distance decreases the interactions of the

machine dynamics and the DG unit, it presents higher voltage drop which reduces the capability of the DG unit in providing active and reactive power to the IM load.

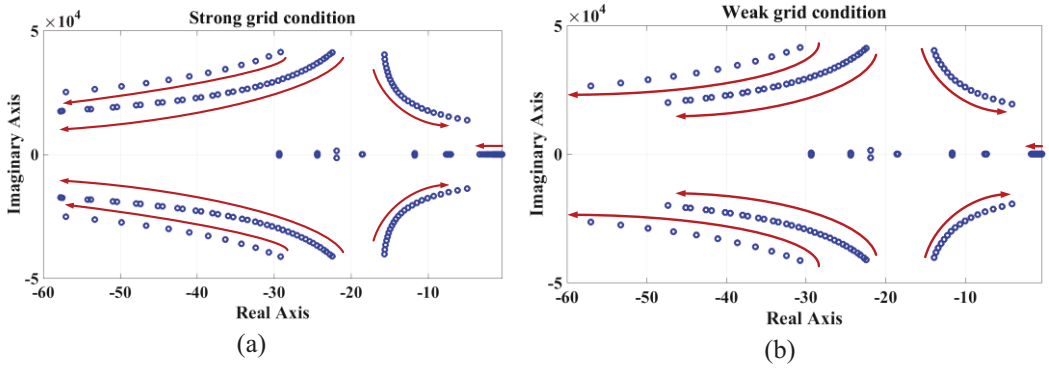

Figure 5.13 Eigenvalue locus of the system modes demonstrating the effect of increasing the length of the line between DG unit and the IM.

This outcome is also investigated in the time-domain simulation model of the system. Results are shown in Figure 5.14 where the DG active power is presented for the case of the initial length of Z_2 (i.e., 0.01 p.u.) and when it is increased to 0.1 p.u., which still represents stable system modes. The implemented RCG strategy is the FMS-RCI with K^+=K^- =5. The same fault scenario is studied at t=1.8 s. It is observed that, although the system is experiencing a stable performance before the fault, the power system including the IM load cannot retrieve its stable mode after fault clearance. The IM rotor lost its speed and the electromagnetic torque. The maximum value of i_1 on all phases stays high which finally leads to the DG unit disconnection and the LVRT failure. This result verifies what is realized in Figure 5.13. Therefore, in the case of installing a DG unit to support an IM load, an efficient length of the power line between them should be considered to prevent future system collapse.

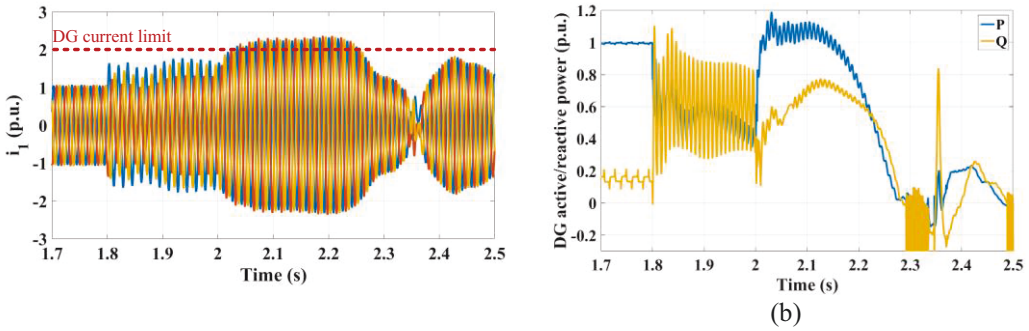

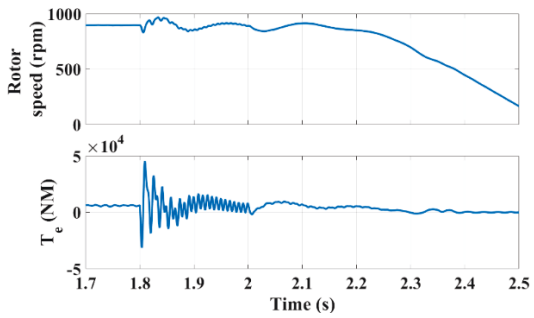

(c)

Figure 5.14 Time-domain simulation results illustrating the effect of the length of Z_2 on the LVRT performance of the system (FMS-RCI method, weak grid condition)

5.6 Experimental Results

The results of the time-domain and the state-space stability analyses are validated using a scaled down 1.0 kVA laboratory prototype as shown inFigure 5.15. The key components for the laboratory setup are the same as detailed in Section 2.5. An induction machine is also connected between the grid and the VSC unit, as demonstrated in Figure 5.15. The machine has four poles, with the output power of 0.25 hp and the nominal voltage value of 208-230 V. The grid stiffness is changed by connecting series inductors to the ac grid so that, the SCR of the studied system can be varied. For the strong grid condition, the SCR is considered 6.6, and for the weak grid condition, the SCR is set to be 2.1. In all test cases, an unbalanced fault is occurred at the same location as the simulation tests cases, i.e., on the line between the grid and the IM

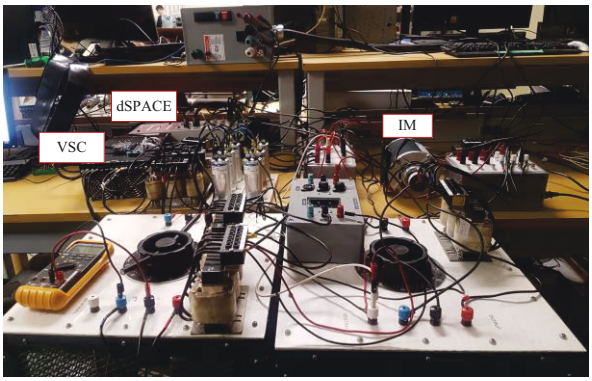

Figure 5.15 Experimental test setup.

5.7 Strong Grid Condition

First, the DG unit is connected to the strong grid, and the LVRT performance of the system is monitored using the traditional and the FMS-RCI strategies. The results are shown in Figure 5.16 representing a successful LVRT performance when employing the traditional RCG and the FMS-RCI with the initially selected parameters as $K^+ = K^- = 2$. However, the FMS-RCI strategy is clearly able to reduce the positive-sequence voltage drop and the negative-sequence voltage value during the same fault condition, compared to the traditional RCG (see Figure 5.16(a) and (b)). In addition, to show the system limitation in increasing the K^+ and K^- parameters, another test case is studied when $K^+ = K^- = 7$, shown in Figure 5.17. In this case, the injected current during the fault is greater than the protection setting (20A) and causes the DG unit trip. These results verify the small-signal and the time-domain simulation results of Section 5.4.1.

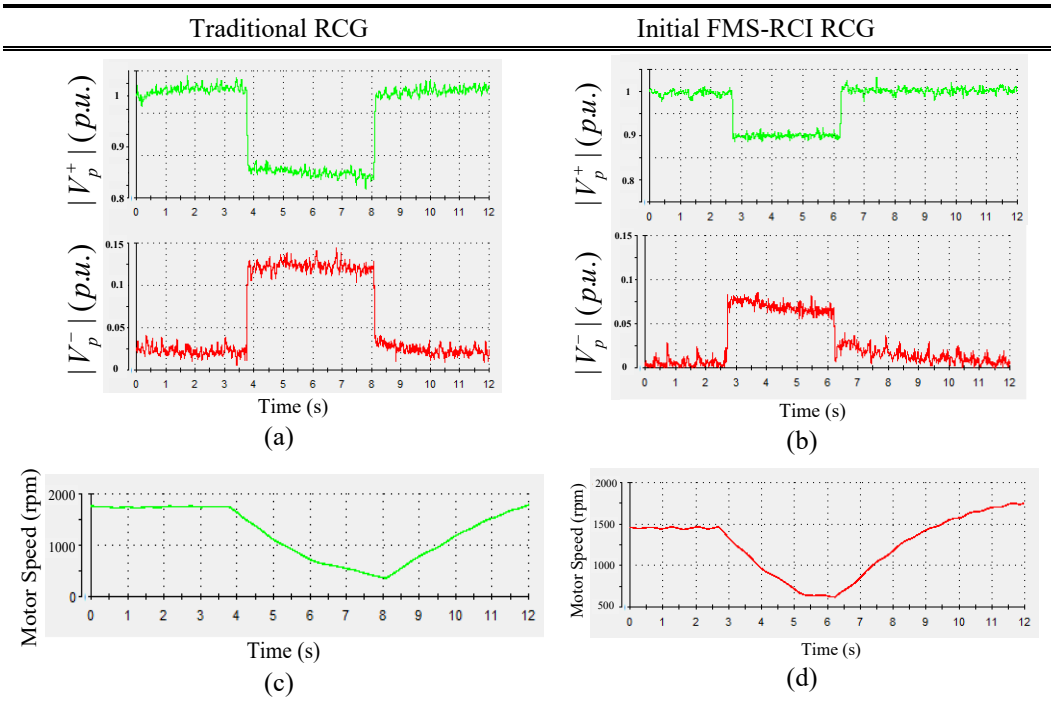

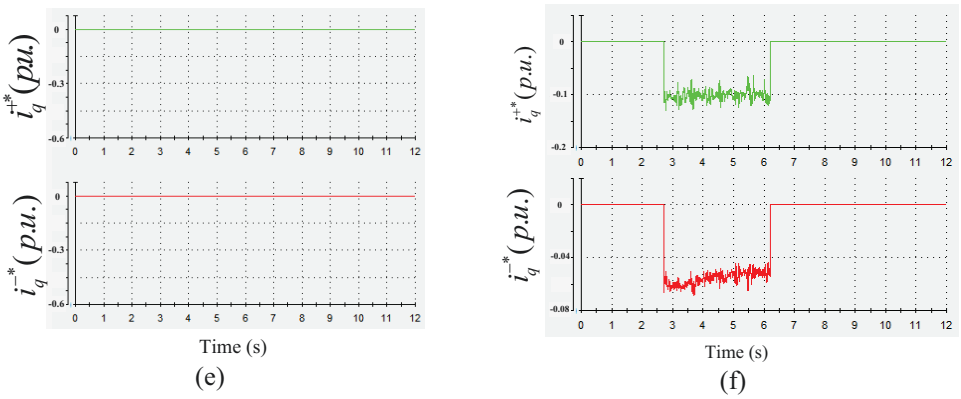

Figure 5.16 Experimental test results showing the LVRT performance of the system under unbalanced fault when the connected grid is strong using the traditional and the initial FMS-RCI (K^+=K^-=2) strategies.

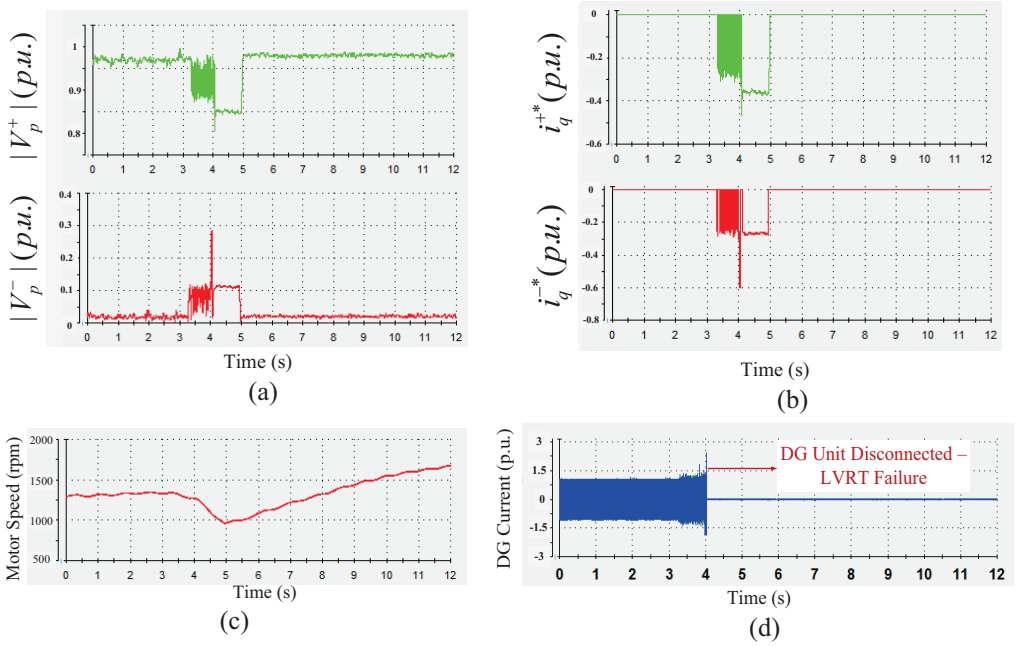

Figure 5.17 Experimental test results showing the LVRT performance of the system under unbalanced fault when the connected grid is strong using the FMS-RCI with K^+=K^-=7.

5.8 Weak Grid Condition

In the next step, the system is connected to the weak grid with SCR=2.1, and the same fault scenario is studied. The results revealed that by employing the traditional RCG and the same initial design of the FMS-RCI which was used in the strong grid case, the system fails in providing the LVRT requirements and the DG unit gets disconnected. Figure 5.18 illustrates the results of the initial FMS-RCI method.

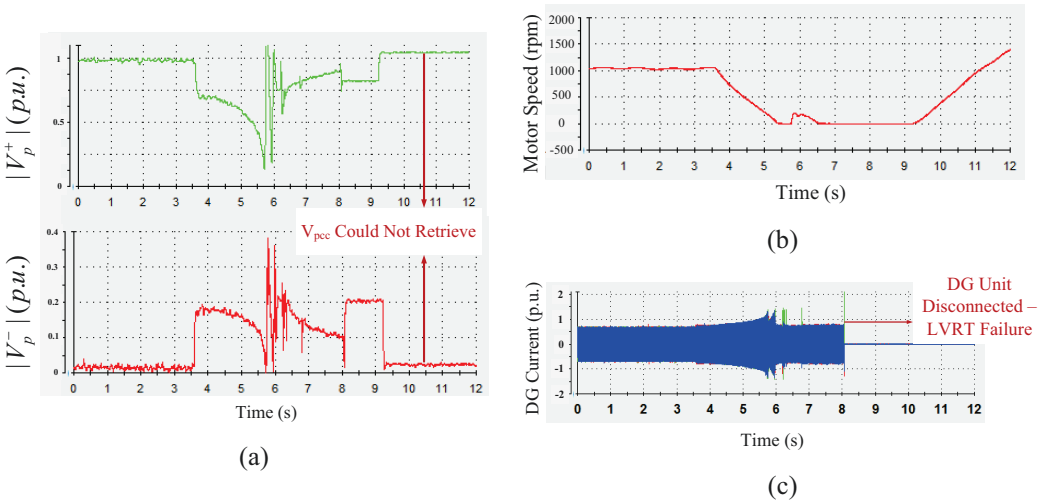

Figure 5.18 Experimental test results showing the LVRT performance of the system under unbalanced fault when the connected grid is weak using the traditional and the initial FMS-RCI ($K^+=K^-=2$) strategies.

Therefore, based on the obtained results of Section 5.4.2, the FMS-RCI parameters are increased to provide more voltage support on the PCC. The results are shown in Figure 5.19 which verify the aforementioned time-domain results. In addition, to find the maximum FMS-RCI parameters value for the case of weak grid condition, the value of K^+ and K^- increased and the same fault scenario is observed. The results revealed that in this case, the maximum value of these parameters is $K^+=K^-=5$ which is lower than what is observed for the strong grid condition. This result is also in agreement with the small-signal and the simulation results. The obtained waveforms are presented in Figure 5.20.

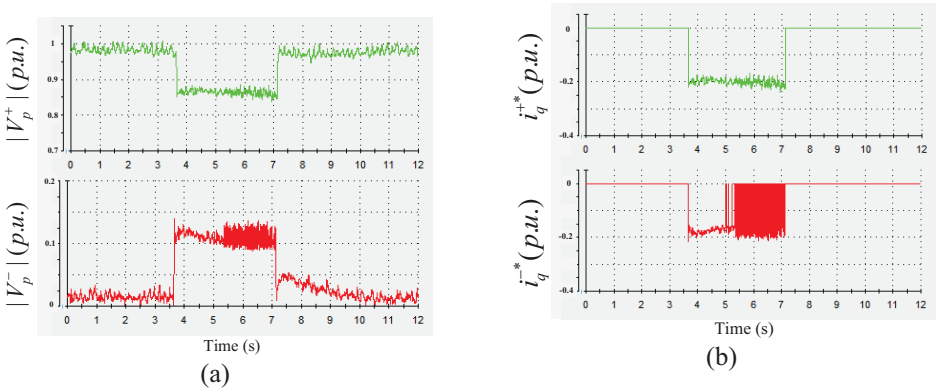

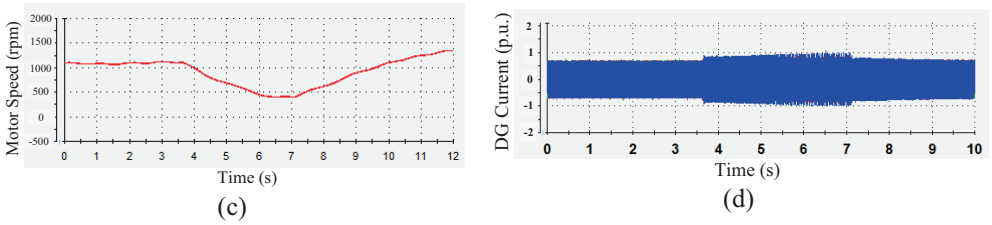

Figure 5.19 Experimental test results showing the LVRT performance of the system under unbalanced fault when the connected grid is weak using FMS-RCI with $K^+ = K^- = 3.5$.

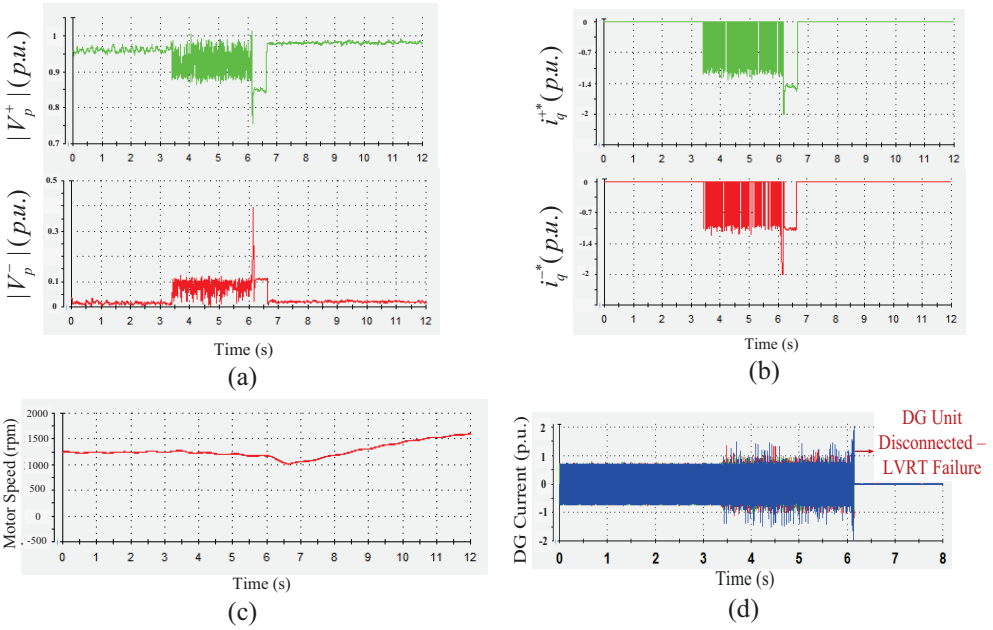

Figure 5.20 Experimental test results showing the LVRT performance of the system under unbalanced fault when the connected grid is weak using FMS-RCI with $K^+ = K^- = 5$.

5.9 Summary

Medium-voltage distributed generation (DG) units can be subjected to a high penetration level of dynamic loads, such as induction motor (IM) loads. The highly nonlinear IM dynamics that couple active power, reactive power, voltage, and supply frequency dynamics can affect the stability of MV grid-connected converter (GCC)-based DG units. However, detailed dynamic analysis and, more importantly, stabilization approaches of GCC-based DG units with IM loads when subjected to the grid faults, are not reported in the literature. In addition, the literature lacks a thorough study on the effect of the grid strength on the low-voltage ride through (LVRT) performance of such a practical system. To fill in this gap, this chapter presents comprehensive integrated modeling, stability analysis, and

LVRT performance improvement methods for GCC-based DG units in the presence of an IM load considering different grid strengths. A detailed multi-stage small-signal model of the complete system is obtained, and the eigenvalue analysis is conducted considering both static and dynamic load modeling. Furthermore, a sensitivity analysis is performed to investigate the effect of the length of the power line between the DG unit and the IM on the stability and LVRT performance of the entire system. Finally, the LVRT performance of the DG unit under an unbalanced grid fault is investigated using three different reference current generation strategies to determine the best strategy to provide a stable and efficient LVRT performance under strong and weak grid conditions. The time-domain simulation and experimental results are also presented to validate the effectiveness of the proposed methods.

Chapter 6

Conclusion and Future Work

In this chapter, the main findings of the thesis are summarized, and future work suggestions are presented.

6.1 Thesis Conclusions

In Chapter 2, a detailed small-signal model and analysis of the dynamics of a grid-connected VSC equipped with the recently developed balanced positive-sequence control and positive–negative-sequence control methods to support the grid under unbalanced conditions have been presented in this chapter. The impacts of the short-circuit ratio, angle of the ac system impedance, and phase-locked-loop parameters on the transient behavior of the VSC have been thoroughly studied and characterized. Furthermore, to improve the dynamic performance of grid-connected VSCs, a simple yet effective current-control-based compensator has been developed to mitigate possible instabilities associated with low-voltage operation. Comparative simulation and experimental results have been used to validate the theoretical analysis and the effectiveness of the proposed compensation scheme. The study has revealed the following:

1. For strong grids (SCR>3), the BPSC is the best choice because it has balanced and sinusoidal current during the fault. Also, it exhibits the lowest I_{max} value.
2. In case of weak grids (2<SCR<3), the PNSC is the best choice in comparison to the conventional controllers; because, it has lower reactive power oscillations and almost zero oscillations on active power. Nevertheless, it should be noted that the PNSC strategy becomes unstable for high PLL parameters (K_{p2} and K_{i2}) when the converter is connected to weak grids.
3. In a weak grid with low X/R ratio, the PNSC strategy is superior choice as compared to the BPSC because its damping ratio reveals minor changes and

stays above zero.

4. In systems with more sensitive protection devices, the BPSC strategy should be adopted because of its considerably lower I_{max} value.

In Chapter 3, a detailed small-signal modeling framework for typical medium-voltage multi-bus distribution power systems with multiple DG units is developed in this chapter. This model includes the positive and negative sequences of the current and voltage components in the decoupled double synchronous reference frame. The proposed models are developed for three different stages of the system (i.e., before-, during- and after-fault) to cover a wide range of system operating points. Furthermore, to precisely study the interactions among DG units, four different control modes in DG units are considered to obtain the linear models and study the system under low-voltage conditions and at different grid strengths. Using the proposed comprehensive models and based on the small-signal stability analyses, different control parameters are re-designed. In addition, the sensitivity analyses are performed to study the effects of different system parameters. Simulation and experimental test cases validated the accuracy and effectiveness of the theoretical analyses.

In Chapter 4, a three-stage modeling approach of a CI-DG unit system equipped with a flexible multi-sequence reactive current injection method is presented in this chapter. The small-signal stability analysis is performed on the system dynamic behavior before, during, and after the unbalanced fault and under the weak grid condition. A new and effective model-based controller parameters design method is proposed to maintain the system stability during and after the fault with the consideration of the mutual interaction among different system controllers. The proposed control system design improved the relative stability of the system under the weak grid condition when subjected to an unbalanced fault; at the same time, the amount of the positive and negative components of the injected reactive current during the unbalanced fault follows the grid code requirements. Then, by applying the proposed design of the controller parameters in the nonlinear time-domain model of the system, the large-signal LVRT performance improvement is observed in the CI-DG in connection to a weak grid. Finally, the laboratory

experiments validated the accuracy of the developed model and the effectiveness of the proposed strategies.

In Chapter 5, the dynamic analysis and performance improvement methods for the GCC-based DG unit system are presented in the presence of an IM load. To assess the impact of utilizing the dynamic load on the integrated system stability, a detailed multi-stage small-signal model of the complete system was obtained, and the eigenvalue analysis was conducted considering both static and dynamic load modeling. The results showed that the dynamic load modeling adds 19 low-frequency less-damped modes to the studied DG unit system which result in lower relative stability margin and could effectively change the shaping of the system eigenvalues. Furthermore, considering the critical effect of the grid stiffness on the LVRT performance of the DG unit system connected to the IM load, the performance of the system was investigated under an unbalanced grid fault using three different reference current generation strategies to indicate the best strategy to provide a stable and efficient LVRT performance in the GCC-based DG unit system under strong and weak grid conditions. The model-based control system improvement method was used in both strong and weak grid conditions using the small-signal stability analysis to implement a stable and efficient system to ride through the grid fault considering the LVRT requirements. Besides, in the case of the weak grid condition, a maximum boundary for selecting the control parameters of the FMS-RCI strategy was obtained to satisfy the LVRT requirement and also maintain the system stability margins. Finally, the sensitivity analysis was also performed to investigate the effect of the length of the power line between the DG unit and the IM on the stability and LVRT performance of the whole system. The time-domain simulation and experimental lab results were also presented to validate the effectiveness of the proposed methods.

6.2 Future Work Suggestions

In continuation of this work, the following topics are suggested for future studies:

- Extending the proposed models and control methods to voltage-source converter-based high-voltage dc transmission systems.
- Addressing the islanded operation mode of the single and multiple converter systems.
- Extending and applying the proposed control methods to parallel converters interfacing large DG units.

References

[1] M. H. J. Bollen – *Understanding Power Quality Problems. Voltage sags and interruptions*, IEEE Press Series on Power Engineering, 2000, ISBN 0-7803- 4713-7.

[2] DS/EN 50160 – *Voltage characteristics of electricity supplied by public distribution systems*, 2nd edition, June 2000.

[3] IEEE Std. 1159/1995 – *IEEE Recommended Practice for Monitoring Electric Power Quality*, June 1995.

[4] IEEE Std. 1250-1995 – *IEEE Guide for service to equipment sensitive to momentary voltage disturbances*, March 1995.

[5] Myo Thu Aung, J. V. Milanovic, "The influence of transformer winding connections on the propagation of voltage sags," *IEEE Transactions on Power Delivery*, vol. 21, no. 1, pp. 262-269, Jan. 2006.

[6] R. Teodorescu, M. Liserre, P. Rodriguez, *Grid Converters for Photovoltaic and Wind Power Systems*, Wiley-IEEE Press, 2011.

[7] A. Oraee, E. Abdi and R. A. McMahon, "Converter rating optimisation for a brushless doubly fed induction generator," *IET Renewable Power Generation*, vol. 9, no. 4, pp. 360-367, 5 2015.

[8] C. Y. Tang, Y. T. Chen, Y. M. Chen, "PV Power System With Multi-Mode Operation and Low-Voltage Ride-Through Capability," *IEEE Transactions on Industrial Electronics*, vol. 62, no. 12, pp. 7524-7533, Dec. 2015.

[9] G. Wen, Y. Chen, Z. Zhong, Y. Kang, "Dynamic Voltage and Current Assignment Strategies of Nine-Switch-Converter-Based DFIG Wind Power System for Low-Voltage Ride-Through (LVRT) Under Symmetrical Grid Voltage Dip," *IEEE Transactions on Industry Applications*, vol. 52, no. 4, pp. 3422-3434, July-Aug. 2016.

[10] H. M. Hasanien, "An Adaptive Control Strategy for Low Voltage Ride Through Capability Enhancement of Grid-Connected Photovoltaic Power Plants," *IEEE Transactions on Power Systems*, vol. 31, no. 4, pp. 3230-3237, July 2016.

[11] G. Rashid, M. H. Ali, "Nonlinear Control-Based Modified BFCL for LVRT Capacity Enhancement of DFIG-Based Wind Farm," *IEEE Transactions on Energy Conversion*, vol. 32, no. 1, pp. 284-295, March 2017.

[12] M. Nasiri , R. Mohammadi, "Peak Current Limitation for Grid Side Inverter by Limited Active Power in PMSG-Based Wind Turbines During Different Grid Faults," *IEEE Transactions on Sustainable Energy*, vol. 8, no. 1, pp. 3-12, Jan. 2017.

[13] N. Jelani, M. Molinas, "Asymmetrical Fault Ride Through as Ancillary Service by Constant Power Loads in Grid-Connected Wind Farm," *IEEE Transactions on Power Electronics*, vol. 30, no. 3, pp. 1704-1713, March 2015.

[14] H. C. Chen, C. T. Lee, P. T. Cheng, R. Teodorescu , F. Blaabjerg, "A Low-Voltage Ride-Through Technique for Grid-Connected Converters With Reduced Power Transistors Stress," *IEEE Transactions on Power Electronics,* vol. 31, no. 12, pp. 8562-8571, Dec. 2016.

[15] K. Ma, F. Blaabjerg , M. Liserre, "Thermal Analysis of Multilevel Grid-Side Converters for 10-MW Wind Turbines Under Low-Voltage Ride Through," *IEEE Transactions on Industry Applications,* vol. 49, no. 2, pp. 909-921, March-April 2013.

[16] A. Calle-Prado, S. Alepuz, J. Bordonau, J. Nicolas-Apruzzese, P. Cortés, J. Rodriguez, "Model Predictive Current Control of Grid-Connected Neutral-Point-Clamped Converters to Meet Low-Voltage Ride-Through Requirements," *IEEE Transactions on Industrial Electronics*, vol. 62, no. 3, pp. 1503-1514, March 2015.

[17] S. Alepuz, A. Calle, S. Busquets-Monge, S. Kouro, B. Wu, "Use of Stored Energy in PMSG Rotor Inertia for Low-Voltage Ride-Through in Back-to-Back NPC Converter-Based Wind Power Systems," *IEEE Transactions on Industrial Electronics*, vol. 60, no. 5, pp. 1787-1796, May 2013.

[18] M. Tsili, S. Papathanassiou, "A review of grid code technical requirements for wind farms," *IET Renewable Power Generation*, vol. 3, no. 3, pp. 308-332, Sept. 2009.

[19] 'Grid code–high and extra high voltage' (E.ON Netz GmbH, Bayreuth, Germany, April 2006).

[20] 'Requirements for offshore grid connections in the E.ON Netz Network' (E.ON Netz GmbH, Bayreuth, Germany, April 2008)

[21] S. Alepuz et al., "Control Strategies Based on Symmetrical Components for Grid-Connected Converters Under Voltage Dips," *IEEE Transactions on Industrial Electronics*, vol. 56, no. 6, pp. 2162-2173, June 2009.

[22] J. Miret, A. Camacho, M. Castilla, L. G. de Vicuña , J. Matas, "Control Scheme With Voltage Support Capability for Distributed Generation Inverters Under Voltage Sags," *IEEE Transactions on Power Electronics*, vol. 28, no. 11, pp. 5252-5262, Nov. 2013.

[23] M. M. Shabestary, Y. A. R. I. Mohamed, "An Analytical Method to Obtain Maximum Allowable Grid Support by Using Grid-Connected Converters," *IEEE Transactions on Sustainable Energy*, vol. 7, no. 4, pp. 1558-1571, Oct. 2016.

[24] A. Yazdani, R. Iravani, “Voltage-Sourced Converters in Power Systems: Modeling, Control, and Applications”, Wiley-IEEE Press, ISBN : 9780470551578, 2010.

[25] Ö. Göksu, R. Teodorescu, C. L. Bak, F. Iov, P. C. Kjær, "Instability of Wind Turbine Converters During Current Injection to Low Voltage Grid Faults and PLL Frequency Based Stability Solution," *IEEE Transactions on Power Systems*, vol. 29, no. 4, pp. 1683-1691, July 2014..

[26] P. Kundur, *Power System Stability and Control*, New York: McGraw- Hill, 1994.

[27] C.W. Taylor, *Power System Voltage Stabilit*y. New York:McGraw-Hill, 1994.

[28] M. Ilic, J. Zaborszky, *Dynamics and Control of Large Electric Power Systems*, New York: Wiley, 2000.

[29] P. C. Krause, O. Wasynczuk, S. D. Sudhoff, *Analysis of Electric Machinery and Drive Systems. Piscataway*, NJ/New York: IEEE Press/Wiley Interscience, 2002.

[30] Hengchun Mao, D. Boroyevich, F. C. Y. Lee, "Novel reduced-order small-signal model of a three-phase PWM rectifier and its application in control design and system analysis," *IEEE Transactions on Power Electronics*, vol. 13, no. 3, pp. 511-521, May 1998.

[31] J. Sun, "Small-Signal Methods for AC Distributed Power Systems–A Review," *IEEE Transactions on Power Electronics*, vol. 24, no. 11, pp. 2545-2554, Nov. 2009.

[32] S. Lissandron, L. Dalla Santa, P. Mattavelli , B. Wen, "Experimental Validation for Impedance-Based Small-Signal Stability Analysis of Single-Phase Interconnected Power Systems With Grid-Feeding Inverters," *IEEE Journal of Emerging and Selected Topics in Power Electronics*, vol. 4, no. 1, pp. 103-115, March 2016.

[33] J. Z. Zhou, H. Ding, S. Fan, Y. Zhang , A. M. Gole, "Impact of Short-Circuit Ratio and Phase-Locked-Loop Parameters on the Small-Signal Behavior of a VSC-HVDC Converter," *IEEE Transactions on Power Delivery*, vol. 29, no. 5, pp. 2287-2296, Oct. 2014.

[34] X. Wang, "Investigation of positive feedback anti-islanding control for multiple inverter-based distributed generators," *2009 IEEE Power & Energy Society General Meeting*, Calgary, AB, 2009, pp. 1-1.

[35] A. Cardenas, K. Agbossou, "Experimental Evaluation of Voltage Positive Feedback Based Anti-Islanding Algorithm: Multi-Inverter Case," *IEEE Transactions on Energy Conversion*, vol. 27, no. 2, pp. 498-506, June 2012.

[36] M. Al Hosani, Z. Qu ,H. H. Zeineldin, "A Transient Stiffness Measure for Islanding Detection of Multi-DG Systems," *IEEE Transactions on Power Delivery*, vol. 30, no. 2, pp. 986-995, April 2015.

[37] VDE-AR-N 4120, *Technical requirements for the connection and operation of customer installations to the high voltage network (TAB high voltage)*, Jan. 2015.

[38] 'European Network for Transmission System Operators for Electricity', *ENTSO-E network code for requirements for grid connection applicable to all generators*, Jun. 2012.

[39] M. M. Shabestary, "A Comparative Analytical Study On Low-Voltage Ride-Through Reference-Current-Generation (LVRT-RCG) Strategies In Converter-Interfaced Der Units," M.S. thesis, ECE. Dept., U of A, Edmonton, AB, 2014.

[40] Kamran Sharifabadi, Lennart Harnefors, Hans-Peter Nee, Staffan Norrga, Remus Teodorescu. *Design, Control, and Application of Modular Multilevel Converters for HVDC Transmission Systems*, First Edition, John Wiley & Sons, Ltd., 2016.

[41] S. Mortazavian, M. M. Shabestary , Y. A. R. I. Mohamed, "Analysis and Dynamic Performance Improvement of Grid-Connected Voltage–Source Converters Under Unbalanced Network Conditions," *IEEE Transactions on Power Electronics,* vol. 32, no. 10, pp. 8134-8149, Oct. 2017.

[42] B. M. Nomikos, C. D. Vournas, "Investigation of induction machine contribution to power system oscillations," *IEEE Transactions on Power Systems,* vol. 20, no. 2, pp. 916–925, May 2005.

[43] A. Kahrobaeian, Y. A. R. I. Mohamed, "Analysis and Mitigation of Low-Frequency Instabilities in Autonomous Medium-Voltage Converter-Based Microgrids With Dynamic Loads," *IEEE Transactions on Industrial Electronics*, vol. 61, no. 4, pp. 1643-1658, April 2014.

[44] A. H. Kasem Alaboudy, H. H. Zeineldin, J. Kirtley, "Simple control strategy for inverter-based distributed generator to enhance microgrid stability in the presence of induction motor loads," *IET Generation, Transmission & Distribution*, vol. 7, no. 10, pp. 1155-1162, October 2013.

[45] A. A. A. Radwan,Y. A. R. I. Mohamed, "Stabilization of Medium-Frequency Modes in Isolated Microgrids Supplying Direct Online Induction Motor Loads," *IEEE Transactions on Smart Grid*, vol. 5, no. 1, pp. 358-370, Jan. 2014.

[46] M. Shahabi, M. R. Haghifam, M. Mohamadian, S. A. Nabavi-Niaki, "Dynamic behavior improvement in a microgrid with multiple DG units using a power sharing approach," *PowerTech, 2009 IEEE Bucharest*, Bucharest, 2009, pp. 1-8.

[47] X. Tang, W. Deng, Z. Qi, "Investigation of the Dynamic Stability of Microgrid," *IEEE Transactions on Power Systems*, vol. 29, no. 2, pp. 698-706, March 2014.

[48] R. Razzaghi, M. Davarpanah, M. Sanaye-Pasand, "A Novel Protective Scheme to Protect Small-Scale Synchronous Generators Against Transient Instability," *IEEE Transactions on Industrial Electronics*, vol. 60, no. 4, pp. 1659-1667, April 2013.

[49] D. Shin, K. J. Lee, J. P. Lee, D. W. Yoo ,H. J. Kim, "Implementation of Fault Ride-Through Techniques of Grid-Connected Inverter for Distributed Energy Resources With Adaptive Low-Pass Notch PLL," *IEEE Transactions on Power Electronics*, vol. 30, no. 5, pp. 2859-2871, May 2015.

[50] R. H. Salim, R. A. Ramos, "Analyzing the effect of the type of terminal voltage feedback on the small signal dynamic performance of synchronous generators," *Proc. 2010 IREP Symp.—Bulk Power System Dynamics and Control—VIII*, Aug. 2–6, 2010.

[51] R. H. Salim, R. A. Ramos, N. G. Bretas, "Analysis of the small signal dynamic performance of synchronous generators under unbalanced operating conditions," *Proc. IEEE Power and Energy Society General Meeting*, Jul. 25–29, 2010.

[52] P. Rodriguez, A. V. Timbus, R. Teodorescu, M. Liserre ,F. Blaabjerg, "Flexible Active Power Control of Distributed Power Generation Systems During Grid Faults," *IEEE Transactions on Industrial Electronics*, vol. 54, no. 5, pp. 2583-2592, Oct. 2007.

[53] S. Golestan, J. M. Guerrero, A. Vidal, A. G. Yepes, J. Doval-Gandoy ,F. D. Freijedo, "Small-Signal Modeling, Stability Analysis and Design Optimization of Single-Phase Delay-Based PLLs," *IEEE Transactions on Power Electronics*, vol. 31, no. 5, pp. 3517-3527, May 2016.

[54] R. H. Salim ,R. A. Ramos, "A Model-Based Approach for Small-Signal Stability Assessment of Unbalanced Power Systems," *IEEE Transactions on Power Systems*, vol. 27, no. 4, pp. 2006-2014, Nov. 2012.

[55] N. Bottrell, M. Prodanovic, T.C. Green, "Dynamic Stability of a Microgrid With an Active Load," *IEEE Transactions on Power Electronics*., vol.28, no.11, pp.5107-5119, Nov. 2013.

[56] Wen Bo, D. Boroyevich, R. Burgos, P. Mattavelli, Z. Shen, "Small-Signal Stability Analysis of Three-Phase AC Systems in the Presence of Constant Power Loads Based on Measured d-q Frame Impedances," *IEEE Transactions on Power Electronics*., vol.30, no.10, pp.5952-5963, Oct. 2015.

[57] P. W. Sauer, M. A. Pai, *Power System Dynamics and Stability*. Englewood Cliffs, NJ: Prentice Hall, 1998.

[58] C.N. Rowe, T.J. Summers, R.E. Betz, D.J. Cornforth, T.G. Moore, "Arctan Power–Frequency Droop for Improved Microgrid Stability," *IEEE Transactions on Power Electronics*, vol.28, no.8, pp.3747-3759, Aug. 2013.

[59] Sh.-F. Chou, Ch.-T. Lee, H-Ch. Ko,P-T. Cheng, "A Low-Voltage Ride-Through Method With Transformer Flux Compensation Capability of Renewable Power Grid-Side Converters", *IEEE Transactions on Power Electronics* , vol. 29, ni. 4, April 2014.

[60] M. Ebrahimi, S. A. Khajehoddin, M. Karimi-Ghartemani, "Fast and Robust Single-PhaseDQCurrent Controller for Smart Inverter Applications," *IEEE Transactions on Power Electronics*, vol. 31, no. 5, pp. 3968-3976, May 2016.

[61] T. Yi, Q. Zian, F. Blaabjerg, L. P. Chiang, "A Dual Voltage Control Strategy for Single-Phase PWM Converters With Power Decoupling Function," *IEEE Transactions on Power Electronics*, vol.30, no.12, pp.7060-7071, Dec. 2015.

[62] L. Xu, Y. Wang, "Dynamic Modeling and Control of DFIG-Based Wind Turbines Under unbalanced Network Conditions", *IEEE Transactions on Power Systems*., vol. 22, no. 1, Feb. 2007.

[63] A. Golieva, "Low Short Circuit Ratio Connection of Wind Power Plants", MSc Thesis, Norwegian University of Science and Technology, Aug. 2015.

[64] "IEEE Guide for Planning DC Links Terminating at AC Locations Having Low Short-Circuit Capacities", IEEE Std 1204-1997, 1997.

[65] L. Harnefors, M. Bongiorno and S. Lundberg, "Input-Admittance Calculation and Shaping for Controlled Voltage-Source Converters," *IEEE Transactions on Industrial Electronics*, vol. 54, no. 6, pp. 3323-3334, Dec. 2007.

[66] M. M. Shabestary, Y. A. R. I. Mohamed, "Analytical Expressions for Multi objective Optimization of Converter-Based DG Operation Under Unbalanced Grid Conditions," *IEEE Transactions on Power Electronics*, vol. 32, no. 9, pp. 7284-7296, Sept. 2017.

[67] S. Ghosh, S. Kamalasadan, "An Integrated Dynamic Modeling and Adaptive Controller Approach for Flywheel Augmented DFIG Based Wind System," *IEEE Transactions on Power Systems*, vol. 32, no. 3, pp. 2161-2171, May 2017.

[68] M. Hamzeh, H. Karimi, H. Mokhtari, "A New Control Strategy for a Multi-Bus MV Microgrid Under Unbalanced Conditions," *IEEE Transactions on Power Systems*, vol. 27, no. 4, pp. 2225-2232, Nov. 2012.

[69] K. M. Muttaqi, A. D. T. Le, M. Negnevitsky, G. Ledwich, "A Novel Tuning Method for Advanced Line Drop Compensator and Its Application to Response Coordination of Distributed Generation With Voltage Regulating Devices," *IEEE Transactions on Industry Applications*, vol. 52, no. 2, pp. 1842-1854, March-April 2016.

[70] A. A. A. Radwan, Y. A. R. I. Mohamed, "Power Synchronization Control for Grid-Connected Current-Source Inverter-Based Photovoltaic Systems," *IEEE Transactions on Energy Conversion,* vol. 31, no. 3, pp. 1023-1036, Sept. 2016.

[71] N. Soni, S. Doolla, M. C. Chandorkar, "Inertia Design Methods for Islanded Microgrids Having Static and Rotating Energy Sources," *IEEE Transactions on Industry Applications*., vol. 52, no. 6, pp. 5165-5174, Nov.-Dec. 2016.

[72] Y. Li, et al., "Power Compensation Control for Interconnection of Weak Power Systems by VSC-HVDC," *IEEE Transactions on Power Delivery*, vol. 32, no. 4, pp. 1964-1974, Aug. 2017.

[73] A. M. Khalil, R. Iravani, "Enhanced Generic Nonlinear and Linearized Models of Wind Power Plants," *IEEE Transactions on Power Systems*, vol. 32, no. 5, pp. 3968-3980, Sept. 2017..

[74] M. Hamzeh, H. Karimi, H. Mokhtari, "Harmonic and Negative-Sequence Current Control in an Islanded Multi-Bus MV Microgrid," *IEEE Transactions on Smart Grid*, vol. 5, no. 1, pp. 167-176, Jan. 2014.

[75] S. S. Al Kaabi, H. H. Zeineldin, V. Khadkikar, "Planning Active Distribution Networks Considering Multi-DG Configurations," *IEEE Transactions on Power Systems*, vol. 29, no. 2, pp. 785-793, March 2014.

[76] M. F. M. Arani, Y. A. R. I. Mohamed, "Assessment and Enhancement of a Full-Scale PMSG-Based Wind Power Generator Performance Under Faults," *IEEE Transactions on Energy Conversion,* vol. 31, no. 2, pp. 728-739, June 2016.

[77] M. A. Kashem, G. Ledwich, "Distributed generation as Voltage support for single wire Earth return systems," *IEEE Transactions on Power Delivery*, vol. 19, no. 3, pp. 1002-1011, July 2004.

[78] M. M. Shabestary, Y. A. R. I. Mohamed, "Analytical Expressions for Multiobjective Optimization of Converter-Based DG Operation Under Unbalanced Grid Conditions," *IEEE Transactions on Power Electronics*, vol. 32, no. 9, pp. 7284-7296, Sept. 2017.

[79] N. Espinoza, M. Bongiorno, O. Carlson, "Novel LVRT Testing Method for Wind Turbines Using Flexible VSC Technology," *IEEE Transactions on Sustainable Energy*, vol. 6, no. 3, pp. 1140-1149, July 2015.

[80] X. Guo, X. Zhang, B. Wang, W. Wu, J. M. Guerrero, “Asymmetrical grid fault ride-through strategy of three-phase grid-connected inverter considering network impedance impact in low-voltage grid,” *IEEE Transactions on Power Electronics*, vol. 29, no. 3, pp. 1064–1068, Mar. 2014.

[81] T. Neumann, T. Wijnhoven, G. Deconinck, I. Erlich, "Enhanced Dynamic Voltage Control of Type 4 Wind Turbines During Unbalanced Grid Faults," *IEEE Transactions on Energy Conversion*, vol. 30, no. 4, pp. 1650-1659, Dec. 2015.

[82] N. M. Dehkordi, N. Sadati ,M. Hamzeh, "A Robust Backstepping High-Order Sliding Mode Control Strategy for Grid-Connected DG Units With Harmonic/Interharmonic Current

Compensation Capability," *IEEE Transactions on Sustainable Energy*, vol. 8, no. 2, pp. 561-572, April 2017.

[83] M. M. Shabestary, Y. A. R. I. Mohamed, "Advanced Voltage Support and Active Power Flow Control in Grid-Connected Converters Under Unbalanced Conditions," *IEEE Transactions on Power Electronics*, vol. 33, no. 2, pp. 1855-1864, Feb. 2018.

[84] S. Mortazavian, Y. A. I. Mohamed, "Dynamic Analysis and Improved LVRT Performance of Multiple DG Units Equipped With Grid-Support Functions Under Unbalanced Faults and Weak Grid Conditions," *IEEE Transactions on Power Electronics*, vol. 33, no. 10, pp. 9017-9032, Oct. 2018.

[85] M. Taleb, M. Akbaba ,E. A. Abdullah, "Aggregation of induction machines for power system dynamic studies," *IEEE Transactions on Power Systems*, vol. 9, no. 4, pp. 2042-2048, Nov 1994.

[86] R. G. de Almeida, J. A. P. Lopes, J. A. L. Barreiros, "Improving power system dynamic behavior through doubly fed induction machines controlled by static converter using fuzzy control," *IEEE Transactions on Power Systems*, vol. 19, no. 4, pp. 1942-1950, Nov. 2004.

[87] G. Diaz, C. Gonzalez-Moran, J. Gomez-Aleixandre,A. Diez, "Composite loads in stand-alone inverter-based microgrids—Modeling procedure and effects on load margin," *IEEE Transactions on Power Systems*, vol. 25, no. 2, pp. 894–905, May 2010.

[88] B. Dağ, A. R. Boynueğri, Y. Ateş, A. Karakaş, A. Nadar , M. Uzunoğlu, "Static Modeling of Microgrids for Load Flow and Fault Analysis," *IEEE Transactions on Power Systems*, vol. 32, no. 3, pp. 1990-2000, May 2017.

[89] G. McLorn, J. Morrow, D. Laverty, R. Best, X. Liu and S. McLoone, "Enhanced ZIP load modelling for the analysis of harmonic distortion under Conservation Voltage Reduction," *CIRED - Open Access Proceedings Journal*, vol. 2017, no. 1, pp. 1094-1097, 10 2017.

[90] J. W. Simpson-Porco, F. Dörfler, F. Bullo, "Voltage Stabilization in Microgrids via Quadratic Droop Control," *IEEE Transactions on Automatic Control,* vol. 62, no. 3, pp. 1239-1253, March 2017.

[91] VDN-e.v. beim VDEW: Transmission Code 2007. *Networks and System Rules of the German Transmission System Operators*, Aug. 2007.

[92] Y. Gui, C. Kim, C. C. Chung, J. M. Guerrero, Y. Guan an, J. C. Vasquez, "Improved Direct Power Control for Grid-Connected Voltage Source Converters," *IEEE Transactions on Industrial Electronics*, vol. 65, no. 10, pp. 8041-8051, Oct. 2018.

[93] J. He, L. Du, S. Yuan, C. Zhang, C. Wang, "Supply Voltage and Grid Current Harmonics Compensation Using Multi-port Interfacing Converter Integrated into Two-AC-Bus Grid," in IEEE Transactions on Smart Grid, 2018 (Early Access).

[94] A. Kahrobaeian, “Modeling, Analysis and Control of Single and Multiple Micro-grid-Based Active Distribution Grids”, PhD Thesis, ECE. Dept., U of A, Edmonton, AB, 2014.

[95] M. Bertoluzzo, G. Buja, “Direct torque control of an induction motor using a single current sensor,” *IEEE Transactions on Industrial Electronics*, vol. 53, no. 3, pp. 778–784, Jun. 2006.

[96] P. M. Shabestari, S. Ziaeinejad and A. Mehrizi-Sani, "Reachability analysis for a grid-connected voltage-sourced converter (VSC)," *2018 IEEE Applied Power Electronics Conference and Exposition (APEC),* San Antonio, TX, 2018, pp. 2349-2354.

[97] K. Ogata, *Modern Control engineering*, fifth edition, NJ, USA: Prentice Hall, 2010.

Appendix A

A.1 Derivation of the BPSC Strategy Small-Signal Equations

Using (1.4) to (1.7), the equations of the BPSC reference-currents are

$$i_d^{*+} = \frac{\frac{2}{3}P_{ref}V_{pd}^{+}}{(V_{pd}^{+2}+V_{pq}^{+2})} + \frac{\frac{2}{3}Q_{ref}V_{pq}^{+}}{(V_{pd}^{+2}+V_{pq}^{+2})} \tag{A.1}$$

$$i_q^{*+} = \frac{\frac{2}{3}P_{ref}V_{pq}^{+}}{(V_{pd}^{+2}+V_{pq}^{+2})} + \frac{\frac{-2}{3}Q_{ref}V_{pd}^{+}}{(V_{pd}^{+2}+V_{pq}^{+2})} \tag{A.2}$$

The linearized BPSC reference currents, i.e., Δi_d^{*+} and Δi_q^{*+} are obtained as follows:

$$\Delta i_d^{*+} = \frac{2}{3}P_{ref}\left[\frac{-m_2}{den}\Delta V_{pd}^{+} + \frac{m_1}{den}\Delta V_{pq}^{+}\right] + \frac{2}{3}Q_{ref}\left[\frac{m_1}{den}\Delta V_{pd}^{+} + \frac{m_2}{den}\Delta V_{pq}^{+}\right] \tag{A.3}$$

$$\Delta i_q^{*+} = \frac{2}{3}P^{*}\left[\frac{m_1}{den}\Delta V_{d}^{+} + \frac{m_2}{den}\Delta V_{q}^{+}\right] - \frac{2}{3}Q^{*}\left[\frac{-m_2}{den}\Delta V_{d}^{+} + \frac{m_1}{den}\Delta V_{q}^{+}\right] \tag{A.4}$$

In which

$$m_1 = -2\,V_{pd-ss}^{+}\,V_{pq-ss}^{+}, \quad m_2 = {V_{pd^-ss}^{+}}^2 - {V_{pq-ss}^{+}}^2, \; den = \left({V_{pd-ss}^{+}}^2 + {V_{pq-ss}^{+}}^2\right)^2 \tag{A.5}$$

Subscripts *ss* denote the steady-state value.

A.2 Derivation of the PNSC Strategy Small-Signal Equations

Using (1.8) to (1.10), the equations of the PNSC reference-currents are

$$i_d^{*+}=\frac{\frac{2}{3}P_{ref}V_{pd}^{+}}{\left|V_p^{+}\right|^2-\left|V_p^{-}\right|^2}-\frac{\frac{2}{3}Q_{ref}V_{pq}^{+}}{\left|V_p^{+}\right|^2-\left|V_p^{-}\right|^2}\qquad i_d^{*-}=\frac{-\frac{2}{3}P_{ref}V_{pd}^{-}}{\left|V_p^{+}\right|^2-\left|V_p^{-}\right|^2}-\frac{\frac{2}{3}Q_{ref}V_{pq}^{-}}{\left|V_p^{+}\right|^2-\left|V_p^{-}\right|^2} \tag{A.6}$$

$$i_q^{*+}=\frac{-\frac{2}{3}P_{ref}V_{pq}^{+}}{\left|V_p^{+}\right|^2-\left|V_p^{-}\right|^2}+\frac{\frac{2}{3}Q_{ref}V_{pd}^{+}}{\left|V_p^{+}\right|^2-\left|V_p^{-}\right|^2}\qquad i_q^{*-}=\frac{-\frac{2}{3}P_{ref}V_{pq}^{-}}{\left|V_p^{+}\right|^2-\left|V_p^{-}\right|^2}+\frac{\frac{2}{3}Q_{ref}V_{pd}^{-}}{\left|V_p^{+}\right|^2-\left|V_p^{-}\right|^2} \tag{A.6}$$

The linearized PNSC reference currents, i.e., Δi_d^{*+}, Δi_q^{*+}, Δi_d^{*-} and Δi_q^{*-} are obtained as follows:

$$\begin{aligned}\Delta i_d^{*+}=&\frac{2}{3}\mathrm{P}_{ref}(f_{1\_v_{pd}^{+}}.\Delta v_{pd}^{+}+f_{1\_v_{pq}^{+}}.\Delta v_{pq}^{+}+f_{1\_v_{pd}^{-}}.\Delta v_{pd}^{-}+f_{1\_v_{pq}^{-}}.\Delta v_{pq}^{-})-\\&\frac{2}{3}Q_{ref}(f_{2\_v_{pd}^{+}}.\Delta v_{pd}^{+}+f_{2\_v_{pq}^{+}}.\Delta v_{pq}^{+}+f_{2\_v_{pd}^{-}}.\Delta v_{pd}^{-}+f_{2\_v_{pq}^{-}}.\Delta v_{pq}^{-})\end{aligned} \tag{A.7}$$

$$\begin{aligned}\Delta i_d^{*+}=&\frac{2}{3}\mathrm{P}_{ref}(f_{1\_v_{pd}^{+}}.\Delta v_{pd}^{+}+f_{1\_v_{pq}^{+}}.\Delta v_{pq}^{+}+f_{1\_v_{pd}^{-}}.\Delta v_{pd}^{-}+f_{1\_v_{pq}^{-}}.\Delta v_{pq}^{-})-\\&\frac{2}{3}Q_{ref}(f_{2\_v_{pd}^{+}}.\Delta v_{pd}^{+}+f_{2\_v_{pq}^{+}}.\Delta v_{pq}^{+}+f_{2\_v_{pd}^{-}}.\Delta v_{pd}^{-}+f_{2\_v_{pq}^{-}}.\Delta v_{pq}^{-})\end{aligned} \tag{A.8}$$

$$\begin{aligned}\Delta i_d^{*-}=&-\frac{2}{3}\mathrm{P}_{ref}(f_{5\_v_{pd}^{+}}.\Delta v_{pd}^{+}+f_{5\_v_{pq}^{+}}.\Delta v_{pq}^{+}+f_{5\_v_{pd}^{-}}.\Delta v_{pd}^{-}+f_{5\_v_{pq}^{-}}.\Delta v_{pq}^{-})-\\&\frac{2}{3}Q_{ref}(f_{6\_v_{pd}^{+}}.\Delta v_{pd}^{+}+f_{6\_v_{pq}^{+}}.\Delta v_{pq}^{+}+f_{6\_v_{pd}^{-}}.\Delta v_{pd}^{-}+f_{6\_v_{pq}^{-}}.\Delta v_{pq}^{-})\end{aligned} \tag{A.9}$$

$$\begin{aligned}\Delta i_q^{*-}=&-\frac{2}{3}\mathrm{P}_{ref}(f_{6\_v_{pd}^{+}}.\Delta v_{pd}^{+}+f_{6\_v_{pq}^{+}}.\Delta v_{pq}^{+}+f_{6\_v_{pd}^{-}}.\Delta v_{pd}^{-}+f_{6\_v_{pq}^{-}}.\Delta v_{pq}^{-})+\\&\frac{2}{3}Q_{ref}(f_{5\_v_{pd}^{+}}.\Delta v_{pd}^{+}+f_{5\_v_{pq}^{+}}.\Delta v_{pq}^{+}+f_{5\_v_{pd}^{-}}.\Delta v_{pd}^{-}+f_{5\_v_{pq}^{-}}.\Delta v_{pq}^{-})\end{aligned} \tag{A.10}$$

In which subscripts *ss* denote the steady-state value, and f_x coefficients are presented in TABLE A.1.

TABLE A.1 f_x coefficients for the representation of the PNSC linearized equations

$$den = \left(V^{+}_{pd-ss}{}^{2} + V^{+}_{pq-ss}{}^{2}\right) + \left(V^{-}_{pd-ss}{}^{2} + V^{-}_{pq-ss}{}^{2}\right)$$

$$f_{1\_v^{+}_{pd}} = \frac{den - 2.V^{+}_{pd-ss}{}^{2}}{den^{2}}, \quad f_{1\_v^{+}_{pq}} = \frac{-2.V^{+}_{pq-ss}.V^{+}_{pd-ss}}{den^{2}}$$

$$f_{1\_v^{-}_{pd}} = \frac{2.V^{-}_{pd-ss}.V^{+}_{pd-ss}}{den^{2}}, \quad f_{1\_v^{-}_{pq}} = \frac{2.V^{-}_{pq-ss}.V^{+}_{pd-ss}}{den^{2}}$$

$$f_{2\_v^{+}_{pd}} = \frac{-2.V^{+}_{pd-ss}.V^{+}_{pq-ss}}{den^{2}}, \quad f_{2\_v^{+}_{pq}} = \frac{den - 2.V^{+}_{pq-ss}{}^{2}}{den^{2}}$$

$$f_{2\_v^{-}_{pd}} = \frac{2.V^{-}_{pd-ss}.V^{+}_{pq-ss}}{den^{2}}, \quad f_{2\_v^{-}_{pq}} = \frac{2.V^{-}_{pq-ss}.V^{+}_{pq-ss}}{den^{2}}$$

$$f_{5\_v^{+}_{pd}} = \frac{-2.V^{+}_{pd-ss}.V^{-}_{pd-ss}}{den^{2}}, \quad f_{5\_v^{+}_{pq}} = \frac{-2.V^{+}_{pq-ss}.V^{-}_{pd-ss}}{den^{2}}$$

$$f_{5\_v^{-}_{pd}} = \frac{den + 2.V^{-}_{pd-ss}{}^{2}}{den^{2}}, \quad f_{5\_v^{-}_{pq}} = \frac{2.V^{-}_{pq-ss}.V^{-}_{pd-ss}}{den^{2}}$$

$$f_{6\_v^{+}_{pd}} = \frac{-2.V^{+}_{pd-ss}.V^{-}_{pq-ss}}{den^{2}}, \quad f_{6\_v^{+}_{pq}} = \frac{-2.V^{+}_{pq-ss}.V^{-}_{pq-ss}}{den^{2}}$$

$$f_{6\_v^{-}_{pd}} = \frac{2.V^{-}_{pd-ss}.V^{-}_{pq-ss}}{den^{2}}, \quad f_{6\_v^{-}_{pq}} = \frac{den + 2.V^{-}_{pq-ss}{}^{2}}{den^{2}}$$

Appendix B

B.1 State Matrix for the Multi-DG Case Study

The linearized equations of the BPSC RCGs in the DDSRF for each DG unit can be obtained using the methods shown in (A.1) to (A.5). To obtain the state matrix for the two-DG system, the following variables are defined:

$$
\begin{aligned}
&m_{11} = -2\,V^{+}_{p_1,d-ss}\,V^{+}_{p_1,q-ss}, \quad m_{21} = {V^{+}_{p_1,d-ss}}^{2} - {V^{+}_{p_1,q-ss}}^{2},\\
&den_1 = \left({V^{+}_{p_1,d-ss}}^{2} + {V^{+}_{p_1,q-ss}}^{2}\right)^2\\
&m_{12} = -2\,V^{+}_{p_2,d-ss}\,V^{+}_{p_2,q-ss}, \quad m_{22} = {V^{+}_{p_2,d-ss}}^{2} - {V^{+}_{p_2,q-ss}}^{2},\\
&den_2 = \left({V^{+}_{p_2,d-ss}}^{2} + {V^{+}_{p_2,q-ss}}^{2}\right)^2\\
&m_{32} = V^{+}_{p_2,q-ss}\,({V^{+}_{p_2,d-ss}}^{2} + {V^{+}_{p_2,q-ss}}^{2}),\\
&m_{42} = V^{+}_{p_2,d-ss}\,({V^{+}_{p_2,d-ss}}^{2} + {V^{+}_{p_2,q-ss}}^{2})
\end{aligned}
\tag{B.1}
$$

where subscripts *ss* denote the steady-state value. The state and input variable matrices for the first CM are shown in (3.2) and (3.3), respectively. To simplify the way of presenting the state-space matrices, some variables are defined in TABLE B.1. t_{ff} stands for the time-constant of the feed-forward filter on the PCC voltage [24].

TABLE B.1 Auxiliary variables for the linearization process

$h_1 = \frac{-R_1 - R_0}{L_1 + L_0}$, $h_2 = \frac{-R_f}{L_f}$ $h_3 = \frac{K_i}{L_f}$, $h_4 = \frac{1}{L_f}$	$h_5 = \frac{2}{3}P_1^*(\frac{-m_{21}}{den_1}) + \frac{2}{3}Q_1^*(\frac{m_{11}}{den_1})$	$h_6 = \frac{2}{3}P_1^*(\frac{m_{11}}{den_1}) + \frac{2}{3}Q_1^*(\frac{m_{21}}{den_1})$
$h_7 = \frac{2}{3}P_1^*(\frac{m_{11}}{den_1}) - \frac{2}{3}Q_1^*(\frac{-m_{21}}{den_1})$	$h_8 = \frac{2}{3}P_1^*(\frac{m_{21}}{den_1}) - \frac{2}{3}Q_1^*(\frac{m_{11}}{den_1})$	$h_9 = \frac{2}{3}P_2^*(\frac{-m_{22}}{den_2}) + \frac{2}{3}Q_2^*(\frac{m_{12}}{den_2})$

$h_{10}=\frac{2}{3}P_2^*(\frac{m_{12}}{den_2})+\frac{2}{3}Q_2^*(\frac{m_{22}}{den_2})$	$h_{11}=\frac{2}{3}(\frac{m_{32}}{den_2})k_{i-v_2}$	$h_{12}=$ $\frac{2}{3}P_2^*(\frac{m_{12}}{den_2})+\frac{2}{3}Q_2^*(\frac{m_{22}}{den_2})$
$h_{13}=$ $\frac{2}{3}P_2^*(\frac{m_{22}}{den_2})-\frac{2}{3}Q_2^*(\frac{m_{12}}{den_2})$	$h_{14}=\frac{-2}{3}(\frac{m_{42}}{den_2})k_{i-v_2}$	$h_{15}=\frac{1}{C_f}$, $h_{16}=\frac{1}{t_{ff}}$
$h_{17}=\frac{-2V_{p_2,d}^+}{\sqrt{(V_{p_2,d}^+)^2}+(V_{p_2,\mathrm{q}}^+)^2}$	$h_{18}=\frac{-2V_{p_2,\mathrm{q}}^+}{\sqrt{(V_{p_2,d}^+)^2}+(V_{p_2,\mathrm{q}}^+)^2}$	$h_{19}=\frac{-R_2}{L_2}$, $h_{20}=\frac{1}{L_2}$ $h_{21}=\frac{-(R_3+R_l)}{L_3}$, $h_{22}=\frac{1}{L_3}$

Therefore, the $A_{1_{(47\times47)}}$ matrix of (3.1) is obtained as follows:

$$A_{1_{(47\times47)}}=\begin{bmatrix} A_{1a_{(24\times24)}} & A_{1b_{(24\times23)}} \\ A_{1c_{(23\times24)}} & A_{1d_{(23\times23)}} \end{bmatrix} \tag{B.2}$$

$A_{1a_{(24\times24)}} =$

	1	2	3	4	5	6	7	8	9	10	11	12	13	14	15	16	17	18	19	20	21	22	23	24
1	h_1	ω_0																			i_{gq}^+			
2	$-\omega_0$	h_1																			$-i_{gd}^+$	-1		
3			h_1	$-\omega_0$																	$-i_{gq}^-$			
4			ω_0	h_1																	i_{gd}^-			
5					h_2								h_3								i_{1q}^+			
6						h_2								h_3							$-i_{1d}^+$	-h4		
7							h_2								h_3						$-i_{1q}^-$			
8								h_2								h_3					i_{1d}^-			
9									h_2								h_3						i_{2q}^+	
10										h_2								h_3					$-i_{2d}^+$	-h4
11											h_2								h_3				$-i_{2q}^-$	
12												h_2								h_3			i_{1d}^-	
13					-1																	h_6		
14						-1																h_8		
15							-1																	
16								-1																
17									-1															h_{10}
18										-1														h_{13}
19											-1													
20												-1												
21																						K_{i_PLL}		
22		h_{15}				h_{15}																		
23																								K_{i_PLL}
24										h_{15}														

(B.3)

$$A_{1b_{(24\times23)}} =$$

	25	26	27	28	29	30	31	32	33	34	35	36	37	38	39	40	41	42	43	44	45	46	47
1																		-1					
2																							
3																			-1				
4																				-1			
5	h_4																	$-h_4$					
6		h_4																					
7			h_4																$-h_4$				
8				h_4																$-h_4$			
9					h_4																$-h_4$		
10						h_4																	
11							h_4															$-h_4$	
12								h_4															$-h_4$
13																		h_5					
14																		h_7					
15																							
16																							
17									h_{11}												h_9		
18									h_{14}												h_{12}		
19																							
20																							
21																							
22											$-h_{15}$												
23																							
24											h_{15}				$-h_{15}$								

(B.4)

$$A_{1c_{(23\times24)}} =$$

	1	2	3	4	5	6	7	8	9	10	11	12	13	14	15	16	17	18	19	20	21	22	23	24
25																								
26																						h_{16}		
27																								
28																								
29																								
30																								h_{16}
31																								
32																								
33																								h_{18}
34																								
35																						h_{20}		$-h_{20}$
36																								
37																								
38																								
39																								h_{22}
40																								
41																								
42	h_{15}				h_{15}																			
43			h_{15}				h_{15}																	
44				h_{15}				h_{15}																
45									h_{15}															
46											h_{15}													
47												h_{15}												

(B.5)

$A_{1d_{(23\times23)}} =$

	25	26	27	28	29	30	31	32	33	34	35	36	37	38	39	40	41	42	43	44	45	46	47
25	$-h_{16}$																	h_{16}					
26		$-h_{16}$																					
27			$-h_{16}$															h_{16}					
28				$-h_{16}$															h_{16}				
29					$-h_{16}$															h_{16}			
30						$-h_{16}$																	
31							$-h_{16}$														h_{16}		
32								$-h_{16}$														h_{16}	
33																				h_{17}			
34										h_{19}	ω_0							h_{20}		$-h_{20}$			
35										$-\omega_0$	h_{19}												
36												h_{19}	$-\omega_0$					h_{20}			$-h_{20}$		
37												ω_0	h_{19}						h_{20}			$-h_{20}$	
38														h_{21}	ω_0					h_{22}			
39														$-\omega_0$	h_{21}								
40																h_{21}	$-\omega_0$				h_{22}		
41																ω_0	h_{21}					h_{22}	
42										$-h_{15}$													
43											$-h_{15}$												
44												$-h_{15}$											
45										h_{15}			$-h_{15}$										
46											h_{15}				$-h_{15}$								
47												h_{15}					$-h_{15}$						

(B.6)

Also, for $A_{2_{(47\times47)}}$ and $B_{1_{(47\times5)}}$ matrices, the non-zero elements are obtained as

$$A_2(5,13) = A_2(6,14) = A_2(7,15) = A_2(8,16) =$$
$$A_2(9,17) = A_2(10,18) = A_2(11,19) = A_2(12,20) = \frac{K_p}{L_f} \qquad \text{(B.7)}$$
$$A_2(21,22) = A_2(23,24) = K_{p,PLL}$$

$$B_1(1,1) = B_1(2,2) = B_1(3,3) = B_1(4,4) = \frac{1}{(L_1 + L_0)} \qquad \text{(B.8)}$$
$$B_1(35,5) = 1$$

Using the obtained A_1, A_2 and B_1 matrices, the complete standard form of the state-space model can be easily obtained based on (3.1).

Appendix C

C.1 State Matrix for the DG Unit with Flexible Grid Support

Using equations (4.4) to (4.6), A_1 is defined as follows:

$$A_{1_{(23\times23)}} = \begin{bmatrix} A_{1a_{(12\times12)}} & A_{1b_{(12\times11)}} \\ A_{1c_{(11\times12)}} & A_{1d_{(11\times11)}} \end{bmatrix} \tag{C.1}$$

where:

$$A_{1a_{(12\times12)}} = \begin{array}{c|cccccccccccc} & 1 & 2 & 3 & 4 & 5 & 6 & 7 & 8 & 9 & 10 & 11 & 12 \\ \hline 1 & \frac{-R_1-R_0}{L_1+L_0} & \omega_0 & & & & & & & & & & \\ 2 & -\omega_0 & \frac{-R_1-R_0}{L_1+L_0} & & & & & & & & & & \\ 3 & & & \frac{-R_1-R_0}{L_1+L_0} & -\omega_0 & & & & & & & & \\ 4 & & & \omega_0 & \frac{-R_1-R_0}{L_1+L_0} & & & & & & & & \\ 5 & & & & & \frac{-R_f}{L_f} & & & & \frac{K_i}{L_f} & & & \\ 6 & & & & & & \frac{-R_f}{L_f} & & & & \frac{K_i}{L_f} & & \\ 7 & & & & & & & \frac{-R_f}{L_f} & & & & \frac{K_i}{L_f} & \\ 8 & & & & & & & & \frac{-R_f}{L_f} & & & & \frac{K_i}{L_f} \\ 9 & & & & & -1 & & & & & & & \\ 10 & & & & & & -1 & & & & & & \\ 11 & & & & & & & -1 & & & & & \\ 12 & & & & & & & & -1 & & & & \end{array} \tag{C.2}$$

$$A_{1b_{(12\times11)}} =$$

	1	2	3	4	5	6	7	8	9	10	11
1	i_{gq}^{+}	$\frac{1}{(L_1+L_0)}$									
2	$-i_{gd}^{+}$		$\frac{1}{(L_1+L_0)}$								
3	$-i_{gq}^{-}$			$\frac{1}{(L_1+L_0)}$							
4	i_{gd}^{-}				$\frac{1}{(L_1+L_0)}$						
5	i_{1q}^{+}	$\frac{-1}{L_f}$				$\frac{1}{L_f}$					
6	$-i_{1d}^{+}$		$\frac{-1}{L_f}$				$\frac{1}{L_f}$				
7	$-i_{1q}^{-}$			$\frac{-1}{L_f}$				$\frac{1}{L_f}$			
8	i_{1d}^{-}				$\frac{-1}{L_f}$				$\frac{1}{L_f}$		
9										$(\frac{2}{3})P_0^*(\frac{-1}{v_{pd,f}^{+\,2}})$	
10										$(\frac{-2}{3})Q_0^*(\frac{-1}{v_{pd,f}^{+\,2}})$	
11											
12											

(C.3)

For $A_{1c_{(11\times12)}}$ and $A_{1d_{(11\times11)}}$ matrices, the non-zero elements are as follows:

$$A_{1c}(2,1) = A_{1c}(3,2) = A_{1c}(4,3) = A_{1c}(5,4) = \frac{-1}{C_f}$$
$$A_{1c}(2,5) = A_{1c}(3,6) = A_{1c}(4,7) = A_{1c}(5,8) = \frac{1}{C_f} \qquad \text{(C.4)}$$

$$
\begin{aligned}
&A_{1d}(1,11) = K_{i,PLL} \\
&A_{1d}(6,2) = A_{1d}(7,3) = A_{1d}(8,4) = A_{1d}(9,5) = \frac{1}{\tau_{\text{ff}}} \\
&A_{1d}(6,6) = A_{1d}(7,7) = A_{1d}(8,8) = A_{1d}(9,9) = \frac{\text{-1}}{\tau_{\text{ff}}} \\
&A_{1d}(10,2) = \frac{1}{\tau_1}, A_{1d}(10,10) = \frac{\text{-1}}{\tau_1}, A_{1d}(11,3) = \frac{1}{\tau_2}, A_{1d}(11,11) = \frac{\text{-1}}{\tau_2},
\end{aligned}
\tag{C.5}
$$

For $A_{2_{(23\times23)}}$ and $B_{1_{(23\times6)}}$ matrices, the non-zero elements are as follows:

$$
\begin{aligned}
&A_2(5,9) = \frac{\mathrm{K}_p}{\mathrm{L}_\mathrm{f}},\ A_2(6,10) = \frac{\mathrm{K}_p}{\mathrm{L}_\mathrm{f}},\ A_2(7,11) = \frac{\mathrm{K}_p}{\mathrm{L}_\mathrm{f}},\ A_2(8,12) = \frac{\mathrm{K}_p}{\mathrm{L}_\mathrm{f}}, \\
&A_2(13,23) = \mathrm{K}_{\mathrm{p},PLL}
\end{aligned}
\tag{C.6}
$$

$$
\begin{aligned}
&B_1(1,1) = \frac{-1}{(\mathrm{L}_1+\mathrm{L}_0)},\ B_1(2,2) = \frac{-1}{(\mathrm{L}_1+\mathrm{L}_0)},\ B_1(3,3) = \frac{-1}{(\mathrm{L}_1+\mathrm{L}_0)}, \\
&B_1(4,4) = \frac{-1}{(\mathrm{L}_1+\mathrm{L}_0)},\ B_1(9,5) = (\frac{2}{3})(\frac{1}{v^+_{pd,f,ss}}),\ B_1(10,6) = (\frac{-2}{3})(\frac{1}{v^+_{pd,f,ss}})
\end{aligned}
\tag{C.7}
$$

By using the above matrices, the final state and input matrices can be obtained based on (3.1) in which $A = (I - A_2)^{-1} A_1$ and $B = (I - A_2)^{-1} B_1$.

Appendix D

D.1 State Matrix for the DG Unit with IM Load

The BPSC strategy (with the related equations presented in Section 1.2.1) is selected as the RCG method in obtaining the following state-space matrices. Also, the following auxiliary variables are defined to facilitate the way of presentation:

$$m_1 = -2\, v^+_{pd,ss}\, v^+_{pq,ss}, \quad m_2 = (v^+_{pd,ss})^2 - (v^+_{pq,ss})^2$$

$$den_1 = [(v^+_{pd,ss})^2 + (v^+_{pq,ss})^2]^2, \quad den_2 = (v^+_{pd,ss})^2 + (v^+_{pq,ss})^2$$

where the subscript *ss* stands for the steady-state values. The A_1 matrix is divided into smaller sections as follows:

$$A_{1_{(35\times35)}} = \begin{bmatrix} A_{1a_{(12\times12)}} & A_{1b_{(12\times12)}} & A_{1c_{(12\times11)}} \\ A_{1d_{(12\times12)}} & A_{1e_{(12\times12)}} & A_{1f_{(12\times11)}} \\ A_{1g_{(11\times12)}} & A_{1h_{(11\times12)}} & A_{1i_{(11\times11)}} \end{bmatrix}$$

The non-zero elements of each sub-matrix are as follows:

$$A_{1a}(1,1) = A_{1a}(2,2) = A_{1a}(3,3) = A_{1a}(4,4) = \frac{-R_1 - R_0}{L_1 + L_0}$$

$$A_{1a}(2,1) = A_{1a}(3,4) = -\omega_0$$

$$A_{1a}(1,2) = A_{1a}(4,3) = \omega_0$$

$$A_{1a}(5,5) = A_{1a}(6,6) = A_{1a}(7,7) = A_{1a}(8,8) = \frac{-R_f}{L_f}$$

$$A_{1a}(5,9) = A_{1a}(6,10) = A_{1a}(7,11) = A_{1a}(8,12) = \frac{K_i}{L_f}$$

$$A_{1a}(9,5) = A_{1a}(10,6) = A_{1a}(11,7) = A_{1a}(12,8) = -1$$

$A_{1b}(1,1) = i_{gq}^{+}$, $A_{1b}(2,1) = -i_{gd}^{+}$, $A_{1b}(3,1) = -i_{gq}^{-}$, $A_{1b}(4,1) = i_{gd}^{-}$

$A_{1b}(5,1) = i_{1q}^{+}$, $A_{1b}(6,1) = -i_{1d}^{+}$, $A_{1b}(7,1) = -i_{1q}^{-}$, $A_{1b}(8,1) = i_{1d}^{-}$

$$A_{1b}(5,2) = A_{1b}(6,3) = A_{1b}(7,4) = A_{1b}(8,5) = \frac{-1}{L_f}$$

$$A_{1b}(5,6) = A_{1b}(6,7) = A_{1b}(7,8) = A_{1b}(8,9) = \frac{1}{L_f}$$

$A_{1b}(9,2) = e_1$, $A_{1b}(9,3) = e_2$, $A_{1b}(10,2) = e_3$, $A_{1b}(10,3) = e_4$

in which:

$$e_1 = (\frac{2}{3} P_0^{*} \frac{-m_2}{den_1}) + (\frac{2}{3} Q_0^{*} \frac{m_1}{den_1}), \quad e_2 = (\frac{2}{3} P_0^{*} \frac{m_1}{den_1}) + (\frac{2}{3} Q_0^{*} \frac{m_2}{den_1})$$

$$e_3 = (\frac{2}{3} P_0^{*} \frac{m_1}{den_1}) - (\frac{2}{3} Q_0^{*} \frac{-m_2}{den_1}), \quad e_4 = (\frac{2}{3} P_0^{*} \frac{m_2}{den_1}) - (\frac{2}{3} Q_0^{*} \frac{m_1}{den_1})$$

$$A_{1c_{(12\times10)}} = [0]_{12\times10}$$

$$A_{1d}(1,5) = A_{1d}(2,6) = A_{1d}(3,7) = A_{1d}(4,8) = \frac{1}{C_f}$$

$$A_{1e}(1,3) = K_{i,PLL}$$

$A_{1e}(2,1) = V_{pq,ss}^{+}$, $A_{1e}(3,1) = -V_{pd,ss}^{+}$, $A_{1e}(4,1) = -V_{pq,ss}^{-}$, $A_{1e}(5,1) = V_{pd,ss}^{-}$

$A_{1e}(2,3) = A_{1e}(5,4) = A_{1e}(10,11) = A_{1e}(12,12) = \omega_0$

$A_{1e}(3,2) = A_{1e}(4,5) = A_{1e}(11,10) = -\omega_0$

$$A_{1e}(2,10) = A_{1e}(3,11) = A_{1e}(4,12) = \frac{-1}{C_f}$$

$$A_{1e}(6,2) = A_{1e}(7,3) = A_{1e}(8,4) = A_{1e}(9,5) = \frac{1}{\tau_{ff}}$$

$$A_{1e}(6,6) = A_{1e}(7,7) = A_{1e}(8,8) = A_{1e}(9,9) = \frac{\text{-1}}{\tau_{ff}}$$

$$A_{1e}(10,1) = i_{2q}^{+}, A_{1e}(11,1) = -i_{2d}^{+}, A_{1e}(12,1) = -i_{2q}^{-}$$

$$A_{1e}(10,2) = A_{1e}(11,3) = A_{1e}(12,4) = \frac{1}{L_2}$$

$$A_{1e}(10,10) = A_{1e}(11,11) = A_{1e}(11,12) = \frac{\text{-}R_2}{L_2}$$

$$A_{1f}(4,1) = \frac{\text{-1}}{C_f}, A_{1f}(11,1) = -\omega_0$$

$$A_{1g_{(10\times12)}} = [0]_{10\times12}$$

$$A_{1h}(1,1) = i_{2d}^{-}, A_{1h}(1,5) = \frac{1}{L_2}$$

$$A_{1h}(2,1) = \frac{-L_m\, s\, i_{Mq}^{+} - L_{lr}\, s\, i_{rq}^{+}}{-L_{lr}}, A_{1h}(3,1) = \frac{L_m\, s\, i_{Md}^{+} + L_{lr}\, s\, i_{rd}^{+}}{-L_{lr}}$$

$$A_{1h}(4,1) = \frac{L_m\, s\, i_{Mq}^{-} + L_{lr}\, s\, i_{rq}^{-}}{-L_{lr}}, A_{1h}(5,1) = \frac{-L_m\, s\, i_{Md}^{-} - L_{lr}\, s\, i_{rd}^{-}}{-L_{lr}}$$

$$A_{1h}(6,1) = \frac{-L_{ls}\, i_{Mq}^{+} - L_m\, s\, i_{rq}^{+}}{-L_{ls}}, A_{1h}(7,1) = \frac{L_{ls}\, i_{Md}^{+} + L_m\, i_{rd}^{+}}{-L_{ls}}$$

$$A_{1h}(8,1) = \frac{L_{ls}\, i_{Mq}^{-} + L_m\, i_{rq}^{-}}{-L_{ls}}, A_{1h}(9,1) = \frac{-L_{ls}\, i_{Md}^{-} - L_m\, i_{rd}^{-}}{-L_{ls}}$$

$$A_{1i}(1,1) = \frac{\text{-}R_2}{L_2}$$

$$A_{1i}(2,2) = A_{1i}(3,3) = A_{1i}(4,4) = A_{1i}(5,5) = \frac{-R_r}{L_{lr}}$$

$$A_{1i}(6,6) = A_{1i}(7,7) = A_{1i}(8,8) = A_{1i}(9,9) = \frac{-R_s}{L_{ls}}$$

$$A_{1i}(3,2) = A_{1i}(4,5) = -s\omega_0,\ A_{1i}(2,3) = A_{1i}(5,4) = s\omega_0$$

$$A_{1i}(3,6) = A_{1i}(4,9) = \frac{-L_m\, s\, \omega_0}{L_{lr}},\ A_{1i}(2,7) = A_{1i}(5,8) = \frac{L_m\, s\, \omega_0}{L_{lr}}$$

$$A_{1i}(7,2) = A_{1i}(8,5) = \frac{-L_m\, \omega_0}{L_{ls}},\ A_{1i}(6,3) = A_{1i}(9,4) = \frac{L_m\, \omega_0}{L_{ls}}$$

$$A_{1i}(7,6) = A_{1i}(8,9) = -\omega_0,\ A_{1i}(6,7) = A_{1i}(9,8) = \omega_0$$

$$A_{1i}(10,2) = \frac{(\frac{3}{4}\rho\frac{L_m}{J})i^+_{Mq}}{-\omega_0},\ A_{1i}(10,3) = \frac{(\frac{3}{4}\rho\frac{L_m}{J})(-i^+_{Md})}{-\omega_0}$$

$$A_{1i}(10,6) = \frac{(\frac{3}{4}\rho\frac{L_m}{J})(-i^+_{rq})}{-\omega_0},\ A_{1i}(10,7) = \frac{(\frac{3}{4}\rho\frac{L_m}{J})i^+_{rd}}{-\omega_0}$$

$$A_{1i}(2,10) = A_{1i}(6,11) = \mathrm{e}_5,\ A_{1i}(3,10) = A_{1i}(7,11) = \mathrm{e}_6$$

$$A_{1i}(4,10) = A_{1i}(8,11) = \mathrm{e}_7,\ A_{1i}(5,10) = A_{1i}(9,11) = \mathrm{e}_8$$

in which:

$$e_5 = \frac{-L_m\, \omega_0\, i^+_{Mq} - L_{lr}\, \omega_0\, i^+_{rq}}{-L_{lr}},\ e_6 = \frac{L_m\, \omega_0\, i^+_{Md} + L_{lr}\, \omega_0\, i^+_{rd}}{-L_{lr}}$$

$$e_7 = \frac{L_m\, \omega_0\, i^-_{Mq} + L_{lr}\, \omega_0\, i^-_{rq}}{-L_{lr}},\ e_8 = \frac{-L_m\, \omega_0\, i^-_{Md} - L_{lr}\, \omega_0\, i^-_{rd}}{-L_{lr}}$$